TRANSPORT CHARACTERIZATION OF CERIUM DIOXIDE PRESSED POWDERS AT LOW TEMPERATURES

A Dissertation

by

TYLER DANIEL MORRISON

Submitted to the Graduate and Professional School of
Texas A&M University
in partial fulfillment of the requirements for the degree of

DOCTOR OF PHILOSOPHY

Chair of Committee,	Donald G. Naugle
Committee Members,	Igor Lyuksyutov
	Wenhao Wu
	Timothy Hughbanks
Head of Department,	Grigory Rogachev

December 2021

Major Subject: Physics

ABSTRACT

Reported is an experimental and computational investigation of the low temperature heat capacity, thermodynamic functions, and thermal conductivity of stoichiometric, polycrystalline CeO_2. The experimentally measured heat capacity at T<15K provides an important correction to the historically accepted experimental values, and the low temperature thermal conductivity serves as the most comprehensive data set at T<400K available. Below 10 K, the heat capacity is observed to obey the Debye T^3 law, with a Debye temperature of $\Theta_D = 455$ K. The entropy, enthalpy, and Gibbs free energy functions are obtained from the experimental heat capacity and compared with predictions from Hubbard-corrected density functional perturbation theory calculations done by colleagues. The thermal conductivity for stoichiometric CeO_2 is determined using the Maldanado continuous measurement technique, along with Laser Flash Analysis, and analyzed according to the Klemens-Callaway model. Further heat capacity measurements were done on nonstoichiometric $CeO_{2-\delta}$ samples in order to investigate signs of an anomalous heat capacity contribution in historical experimental values. The low temperature heat capacity data for nonstoichiometric samples showed a Schottky anomaly characteristic of Zeeman splitting in a paramagnetic salt. This Schottky contribution shows a magnetic dependence typical of Zeeman splitting of ground state energy levels. The nonstoichiometric heat capacity measurements were fitted with a multi-level Schottky funtion, and then the entropy was calculated. This entropy scales with the number of oxygen vacancies in the lattice. These measurements show signs of a more complex magnetic structure that has so far been unreported in the literature for this material.

DEDICATION

To my dear friend, Dr. Tristan S. Leggett (1983-2015)

Thank you for showing me the courage to keep going in the face of impossible odds.

ACKNOWLEDGMENTS

I would like to thank my advisor/committee chair, Dr. Naugle, and my committee members, Dr. Lyuksyutov, Dr. Wu, and Dr. Hughbanks, for their guidance and support throughout the course of this research.

This research wouldn't have been possible without tremendous support from my friend Dr. Elizabeth Wood. I also owe Dr. Daya Rathnayaka a great deal for his support and encouragement in the lab over many years.

I am indebted to Dr. Joseph Ross for many fruitful discussions on heat capacity and low temperature measurements.

Thanks to Dr. Sung Oh Woo for his friendship over the years. Finishing this document wouldn't have been possible without his encouragement and suggestions.

Raman measurements were thanks to use of tools in Dr. Sarbajit Banerjee's lab with guidance from Dr. Banerjee's students Nathan Fleer and Troy Alivio.

Texas A&M University wouldn't have been the same without my friends and colleagues, cheers.

Finally, thanks to my family for their encouragement and especially to my wife Maria for her patience and love during the most challenging parts of this endeavor.

CONTRIBUTORS AND FUNDING SOURCES

Contributors

This work was supported by a dissertation committee consisting of Professors Donald G. Naugle, Igor Lyuksyutov, and Wenhao Wu of the Department of Physics and Astronomy and Professor Timothy Hughbanks of the Department of Chemistry.

Samples were provided by Dr. Elizabeth Wood and Dr. Andrew T. Nelson of Los Alamos National Laboratory.

The DFPT data referenced in this work was provided by Dr. Phillippe F. Weck of Sandia National Laboratory and Dr. Eunja Kim of the University of Nevada, Las Vegas.

Work cited in this dissertation is done so with the permission of the authors, is included under the guidelines of fair use, or is in the public domain.

The student would like to thank S. Banerjee for use of the Raman Spectrometer; T.E.G. Alivio, and N.A. Fleer for their help performing Raman measurements; K.D.D. Rathnayaka for help with low-temperature measurements and useful discussions; and C.C. Hays, J.H. Ross, R.E. Allen, and T. Hughbanks for useful discussions. The student is further indebted to M. Khafizov for freely sharing the data referenced in this study.

All other work conducted for this dissertation was completed by the student independently.

Funding Sources

The sample preparation presented here was conducted at Los Alamos National Laboratory under the National Nuclear Security Administration contract DE-AC52-06NA25396. Sandia National Laboratories is a multi-mission laboratory managed and operated by National Technology and Engineering Solutions of Sandia, LLC., a wholly owned subsidiary of Honeywell International, Inc., for the U.S. Department of Energys National Nuclear Security Administration under contract DE-NA0003525. The views expressed in this work do not necessarily represent the views of the U.S. Department of Energy or the United States Government.

Low-temperature experimental work in this study was supported by The Robert A. Welch Foundation (A-0514), Houston, TX and TAMU-NSFC (Proj. 2014-30). Graduate study was supported with a Welch Predoctoral Fellowship during most of this work. Support was also obtained through a Charles F. Squire Graduate Fellow during part of this project.

NOMENCLATURE

DFPT	Density Functional Perturbation Theory
DFT	Density Functional Theory
DFT+U	Hubbard Corrected Density Functional Theory
DSC	Differential Scanning Calorimetry
GGA	Generalized Gradient Approximation
KCM	Klemens-Callaway Model
LDA	Local Density Approximation
LFA	Laser Flash Analysis
MTRM	Modulated Thermoreflectance Microscopy
EPR	Electron Paramagnetic Resonance
PBE	Perdew-Burke-Ernzerhof
PBEsol	Perdew-Burke-Ernzerhof revised for solids
PPMS	Physical Properties Measurement System
SOC	Spin-Orbit Coupling
CF	Crystal Field
P	Pressure
V	Volume
T	Temperature
R	Gas Constant
S	Entropy
U	Internal Energy
A	Helmholtz Function

H	Enthalpy
G	Gibb's Function
k_B	Boltzmann's Constant
N_A	Avogadro's Number
C_V	Specific Heat at Constant Volume
C_P	Specific Heat at Constant Pressure
E	Energy
h or $\hbar$	Planck's Constant or reduced Planck's Constant
v	Frequency
ω	Angular Frequency
Θ_E	Einstein Temperature
Θ_D	Debye Temperature
$g(\omega)$	Density of States

TABLE OF CONTENTS

Page

ABSTRACT ii

DEDICATION iii

ACKNOWLEDGMENTS iv

CONTRIBUTORS AND FUNDING SOURCES v

NOMENCLATURE vii

TABLE OF CONTENTS ix

LIST OF FIGURES xi

1. INTRODUCTION 1

2. THEORETICAL BACKGROUND 4

2.1 Some Preliminary Thermodynamics 4
2.2 Heat Capacity 6
2.2.1 The Law of Dulong and Petit 6
2.2.2 Einstein Model of the Lattice Heat Capacity 7
2.2.3 Debye Model of the Lattice Heat Capacity 9
2.2.4 The Diatomic Lattice 13
2.2.5 Heat Capacity of Conduction Electrons 14
2.2.6 Schottky Anomalies 16
2.3 Thermal Conductivity of Solids 18
2.4 The Klemens-Callaway Model 19

3. EXPERIMENTAL METHODS 21

3.1 The Quantum Design Physical Properties Measurement System 21
3.2 Heat Capacity 22
3.2.1 Simple Model 22
3.2.2 Two-tau Model™ 25
3.2.3 Dual-Slope Technique 30
3.2.4 Heat Capacity Hardware 32
3.2.4.1 Calorimetry Puck 32
3.2.4.2 Heat Capacity DSP Card 32
3.3 Thermal Conductivity 34

3.3.1 Steady-State Method 36
3.3.2 Pulse Power Method 38
3.3.3 Thermal Conductivity Hardware 41
3.3.3.1 Thermal Transport Puck 41
3.3.3.2 ACT Controller Card 43
3.4 Laser Flash Analysis 43

4. SAMPLE PREPARATION 46

4.1 Sample Fabrication 46
4.2 Heat Capacity Sample Preparation 47
4.3 Thermal Conductivity Sample Preparation 47

5. STOICHIOMETRIC CEO_2 RESULTS AND DISCUSSION 52

5.1 Raman Spectroscopy 52
5.2 Molar Heat Capacity 55
5.3 Thermodynamic Functions 59
5.4 Thermal Conductivity 60
5.4.1 Discussion on Phonon Scattering 66

6. NONSTOICHIOMETRIC $CEO_{2-\delta}$ RESULTS AND DISCUSSION 68

6.1 Oxygen Vacancies in Nonstoichiometric $CeO_{2-\delta}$ 68
6.2 Sample Reduction 70
6.3 Raman Spectroscopy of $CeO_{2-\delta}$ 70
6.4 Molar Heat Capacity of $CeO_{2-\delta}$ 72
6.5 Schottky Contribution to the Heat Capacity 79
6.6 Magnetic Function Fitting 86
6.7 Spin-Orbit Coupling 88
6.8 Entropy of $CeO_{2-\delta}$ 90

7. SUMMARY AND CONCLUSIONS 98

7.1 Conclusions 98
7.2 Further Study 99

REFERENCES 100

LIST OF FIGURES

FIGURE Page

3.1 Schematic of the experimental apparatus used to measure heat capacity in the PPMS. Adapted from Quantum Design user training material. 24

3.2 Circuit equivalent of the simple model for heat capacity. Adapted from Quantum Design user training material. 24

3.3 Idealized heat pulse and temperature response from a sample heat capacity measurement. 26

3.4 Schematic of the experimental apparatus used to measure heat capacity in the PPMS showing the two-tau model. Adapted from Quantum Design user training material. 27

3.5 Circuit equivalent of the two-tau model for heat capacity. Adapted from Quantum Design user training material. 28

3.6 Typical example of a heat pulse in the dual slope method. Data is from a sample measured in this study. Adapted from Quantum Design user training material. 31

3.7 Calorimeter Puck for the PPMS. Adapted from Quantum Design user training material. 33

3.8 Simple Steady State Heat Flow 37

3.9 Schematic of the experimental apparatus used to measure thermal conductivity in the PPMS. Adapted from Quantum Design user training material. 39

3.10 Circuit equivalent of the thermal transport. Adapted from Quantum Design user training material. 40

3.11 Heat pulse and temperature response at hot and cold thermometer shoes during thermal conductivity measurement. 42

3.12 Thermal Transport Option Puck. Adapted from Quantum Design user training material. 44

4.1 Thermal profile used to sinter CeO_2. 46

4.2 Micrograph of CeO_2 at $700\times$ magnification using a backscatter detector. Sample was cross-sectioned and thermally etched prior to imaging. 48

4.3 Microscope image of a typical CeO_2 sample after preparation with copper wire and high thermal conductivity epoxy. 50

4.4 Microscope image of a typical CeO_2 sample after mounting on the Quantum Design thermal transport option measurement puck. 51

5.1 Typical Raman Shift of CeO_2 Samples in this study. The vertical line at 465 cm^-1 represents the F_{2g} peak and is typical of high quality samples. 54

5.2 Measured standard-pressure isobaric molar heat capacity (C_P) of CeO_2 and DFPT/PBEsol calculated C_P and isochoric molar heat capacity (C_V). Calorimetric data from previous studies are also displayed: Westrum and Beale[1], Kuznetsov *et al.*[2], Krishnan and Nagarajan[3], Gallagher and Dworzak[4], Riess *et al.*[5], King and Christensen[6]. Inset shows experimental data as C/T vs. T^2 and a fit of the data to the low-temperature T^3 limit of the simple Debye model. 56

5.3 Calorimetric data and DFPT/PBEsol results for the entropy of CeO_2. Calorimetric data from Westrum and Beale[1] are also represented. 57

5.4 Experimental data and DFPT/PBEsol results for the enthalpy function of CeO_2. Calorimetric data from Westrum and Beale[1], King and Christensen[6], and Yashvili *et al.*[7] are also shown. 61

5.5 Experimental data and DFPT/PBEsol results for the Gibbs energy function of CeO_2. Calorimetric data from Westrum and Beale[1] are also displayed. 62

5.6 Experimental data and Klemens-Callaway fit for the Thermal Conductivity of CeO_2. LFA data from this study and MTRM data from Khafizov *et al.*[8] are also displayed. Error bars in this work are equal to or smaller than the symbol size, i.e. 5% for LFA measurements. 63

5.7 Variation of the effective Debye temperature Θ_D with T for stoichiometric CeO_2. .. 65

6.1 Crystal structure of stoichiometric CeO_2. Cerium atoms (yellow) are located at the corners and face centers of a cube, and Oxygen atoms (red) at the center of tetrahedral Cerium cages. Each Cerium atom is surrounded by eight nearest-neighbor Oxygen atoms. 69

6.2 Raman Shift of nonstoichiometric $CeO_{2-\delta}$ samples observed in this study compared with stoichiometric CeO_2 samples. Theoretical overtone peaks above the F_{2g} peak in the range 600-800 (cm^{-1}) are not observed for these samples, nor is a broadening of the F_{2g} peak. The Raman spectrums have been shifted vertically for clarity. 71

6.3 Total molar heat capacity of $CeO_{1.968}$ at 0-9 T (symbols). The number of plotted points has been reduced for clarity. The lattice heat capacity of stoichiometric CeO2 is plotted as a solid line. 74

6.4 Total molar heat capacity of $CeO_{1.975}$ at 0-9 T (symbols). The number of plotted points has been reduced for clarity. The lattice heat capacity of stoichiometric CeO2 is plotted as a solid line. 75

6.5 Total molar heat capacity of $CeO_{1.984}$ at 0-9 T (symbols). The number of plotted points has been reduced for clarity. The lattice heat capacity of stoichiometric CeO2 is plotted as a solid line. 76

6.6 Total molar heat capacity of $CeO_{1.993}$ at 0-9 T (symbols). The number of plotted points has been reduced for clarity. The lattice heat capacity of stoichiometric CeO2 is plotted as a solid line. 77

6.7 Total molar heat capacity of $CeO_{1.998}$ at 0-9 T (symbols). The number of plotted points has been reduced for clarity. The lattice heat capacity of stoichiometric CeO2 is plotted as a solid line. 78

6.8 Schottky contribution at 0-9 T (symbols) for the $CeO_{1.968}$ sample. The number of plotted points has been reduced for clarity. Also plotted is a multi-level Schottky fitting function that shows excellent agreement with the plotted data. 80

6.9 Schottky contribution at 0-9 T (symbols) for the $CeO_{1.975}$ sample. The number of plotted points has been reduced for clarity. Also plotted is a multi-level Schottky fitting function that shows excellent agreement with the plotted data. 81

6.10 Schottky contribution at 0-9 T (symbols) for the $CeO_{1.984}$ sample. The number of plotted points has been reduced for clarity. Also plotted is a multi-level Schottky fitting function that shows excellent agreement with the plotted data. 82

6.11 Schottky contribution at 0-9 T (symbols) for the $CeO_{1.993}$ sample. The number of plotted points has been reduced for clarity. Also plotted is a multi-level Schottky fitting function that shows excellent agreement with the plotted data. 83

6.12 Schottky contribution at 0-9 T (symbols) for the $CeO_{1.998}$ sample. The number of plotted points has been reduced for clarity. Also plotted is a multi-level Schottky fitting function that shows excellent agreement with the plotted data. 84

6.13 Internal magnetic field fitting parameter H_0 vs applied field H. 89

6.14 Schematic of the 4f electron energy levels, including spin-orbit coupling and crystal field splitting terms. Figure is not to scale. 91

6.15 Calculated entropy at 0-9 T for the $CeO_{1.968}$ sample. For clarity, experimental data has been left off and the horizontal axis has been plotted on a logarithmic scale. Also plotted is the entropy at the inflection point for the 0T curve. 93

6.16 Calculated entropy at 0-9 T for the $CeO_{1.975}$ sample. For clarity, experimental data has been left off and the horizontal axis has been plotted on a logarithmic scale. Also plotted is the entropy at the inflection point for the 0T curve. 94

6.17 Calculated entropy at 0-9 T for the $CeO_{1.984}$ sample. For clarity, experimental data has been left off and the horizontal axis has been plotted on a logarithmic scale. Also plotted is the entropy at the inflection point for the 0T curve. 95

6.18 Calculated entropy at 0-9 T for the $CeO_{1.993}$ sample. For clarity, experimental data has been left off and the horizontal axis has been plotted on a logarithmic scale. Also plotted is the entropy at the inflection point for the 0T curve. 96

6.19 Calculated entropy at 0-9 T for the $CeO_{1.998}$ sample. For clarity, experimental data has been left off and the horizontal axis has been plotted on a logarithmic scale. Also plotted is the entropy at the inflection point for the 0T curve. 97

1. INTRODUCTION[1]

Cerium dioxide (CeO_2) is used in a wide range of technological applications owing to its favorable redox properties, physicochemical stability, optical transparency, high dielectric constant and refractive index, and mixed electronic-ionic conduction properties. CeO_2 has attracted considerable attention recently as a catalyst due to its high oxygen mobility and storage capacity[10, 11]. CeO_2 is also suitable for epitaxial growth on Si [12], making it desirable for applications in microelectronics. CeO_2-based materials find applications as automotive and biomedical catalysts, [13, 14] gas sensors, [15] in high-temperature superconducting tapes, [16] hydrogen production and fuel cells, [17, 18, 19] and luminescence devices[20]. CeO_2 also serves as a surrogate for actinide dioxide nuclear fuels, such as UO_2 and PuO_2, and other f-electron oxide materials of interest in nuclear waste management[21, 22].

With the wide applicability of CeO_2 in modern technology, there is great interest and a wealth of information available for this material in the literature. Despite the vast amount of published data, limited thermal data exist in the low-temperature range below $\simeq 400$ K. As recently discussed in the review by Konings *et al.* [23], the most extensive set of low-temperature heat capacity data for CeO_2 was collected in 1961 by Westrum and Beale between 5 and 300 K by adiabatic calorimetry [1]. Heat-capacity measurements were also reported by Riess *et al.* [5] ($350 - 900$ K) using adiabatic scanning calorimetry, and by Gallagher and Dworzak [4] ($418 - 758$ K) and Krishnan and Nagarajan [3] ($280 - 820$ K) by differential scanning calorimetry (DSC). High-temperature enthalpy increment data were reported by Kuznetsov *et al.* [2] (in the range $608 - 1172$ K, although data down to 298 K were mentioned in other studies [3]), by King and Christensen [6] ($400 - 1800$ K), and by Yashvili *et al.* [7] ($391 - 1624$ K).

Furthermore, limited density functional theory (DFT) studies focused recently on the high-

[1]Part of this chapter is reprinted with permission from "A Comprehensive Assessment of the Low-Temperature Thermal Properties and Thermodynamic Functions of CeO_2" by T. D. Morrison, E. S. Wood, P. F. Weck, E. Kim, S. O. Woo, A. T. Nelson, and D. G.Naugle 2019. The Journal of Chemical Physics, vol. 151, p. 044202, Copyright 2019, The Journal of Chemical Physics and AIP Publishing.[9]

temperature thermodynamic properties of CeO_2 [24, 25, 26]. These computational investigations utilized Hubbard-corrected DFT (DFT+U) within either the local-density approximation (LDA+U) or the generalized-gradient approximation (GGA+U) to correctly describe strong on-site Coulomb repulsion between localized Ce $4f$ electrons. Both GGA+U studies by Gopal and van de Walle [24] and Niu *et al.* [26] utilized the standard parameterization of Perdew, Burke, and Ernzerhof [27] (PBE) to calculate the thermodynamic properties of CeO_2. However, a recent GGA+U study by Weck and Kim [28] demonstrated that the more recent Perdew, Burke, and Ernzerhof revised parameterization for solids [29] (PBEsol) describes experimental crystalline parameters and properties of CeO_2 and Ce_2O_3 with superior accuracy, compared to other standard GGA functionals such as PBE. Therefore, a reexamination of the thermodynamic properties of CeO_2 using DFT+U/PBEsol appears timely.

This joint experimental investigation of the thermodynamic properties of CeO_2 below $\simeq 400$ K is motivated by a need to extend the fundamental understanding of the lower temperature behavior of this versatile material and to present a comprehensive and accurate thermodynamic picture of this material in the lower temperature regime, as well as to provide a solid experimental test of recent first-principles calculations. The low temperature data presented here is essential for testing the modern computational techniques. DFT studies can be well fitted to the higher temperature regimes, but if they do not match the low temperature behavior the modeling is not a truly accurate picture of the material.

Specifically, the T ≤ 400 K heat capacity, thermodynamic functions, and thermal conductivity measurements of stoichiometric, polycrystalline, sintered CeO_2 monolithic samples is reported. The heat capacity is measured using adiabatic calorimetry employing a combination of relaxation and the dual slope techniques. The entropy, enthalpy function, and Gibbs free energy function are obtained from the experimental heat capacity data and compared with predictions from Hubbard-corrected density functional perturbation theory (DFPT) calculations using the PBEsol functional. The thermal conductivity is determined using the Maldanado continuous measurement technique, along with Laser Flash Analysis (LFA), and analyzed according to the Klemens-Callaway model.

The results reported in this study below $\simeq 400$ K provide accurate thermal data for CeO_2 in a temperature range of high relevance for technological applications.

2. THEORETICAL BACKGROUND

2.1 Some Preliminary Thermodynamics

It is natural to begin the theoretical discussion of this work with some simple thermodynamics. The material here will be clarified in the subsequent sections. Further, there are number of excellent works which are devoted to the principles of thermodynamics, but I feel it is important to briefly cover the fundamentals here.

Consider two blocks of a material. To make things more familiar, let's imagine them to be copper. If you were to bring one of the blocks into contact with a mercury thermometer, then after a certain length of time, the thermometer would equilibrate to a constant value. After removal of the first block, let the second block be brought into contact with the same thermometer. Suppose that there is then no change in the reading on the thermometer. We can then conclude that both blocks are in thermal equilibrium with the given thermometer. This idea can be stated more formally. If system A is in thermal equilibrium with system B, and system B is in thermal equilibrium with system C, then system A is in thermal equilibrium with system C. Thus the relationship of thermal equilibrium is transitive. Note that this fact is not derivable from other laws, and since it logically precedes the other thermodynamic laws it is often referred to as the zeroth law of thermodynamics. This law is then the basis of temperature measurement as numbers can be placed on the mercury thermometers allowing for quantitative evaluation. Comparing different thermometers as well as other measurement devices such as thermocouples or resistance thermometers remains an issue. This suggests the need for a standard scale. The current scale is the International Temperature Scale of 1990 or ITS-90. [30]

It is well known that if a quantity of heat dQ is added to a closed system, that heat will either increase the internal energy dU or contribute to the work done by the system dW. That is to say, conservation of energy must always hold. This relation is known as the first law of thermodynamics

and is formally stated

$$dQ = dU + dW. \tag{2.1}$$

Following the first law of thermodynamics, the traditional quantitative statement of the second law of thermodynamics is due to Clausius. [31] Assuming that the heat exchange is reversible the second law of thermodynamics allows for the calculation of entropy S in accordance with the relation

$$dQ = TdS. \tag{2.2}$$

Note that this equality does not hold for irreversible process. The second law is therefore a statement that the entropy must either remain constant or always increase in a closed system.

When calculating the work done by a system, the example of a compression of an ideal gas is very easy to imagine. In an ideal gas, the work done by the system must be an expansion (in volume) of the gas. This is because, in a closed system, the pressure P is the same in all directions. Then dW must be of the form

$$dW = PdV. \tag{2.3}$$

Combining equations 2.1, 2.2, and 2.3 one can see that the change in internal energy is then

$$dU = TdS - PdV. \tag{2.4}$$

Continuing with the example of an ideal gas, they obey what is arguably the most famous equation of state

$$PV = nRT \tag{2.5}$$

where P is the pressure, V the volume, n the number of moles, R is a constant, and T is the temperature. In general, the temperature, volume, and pressure are not independent and obey an equation of state of the form

$$f(P, V, T) = 0. \tag{2.6}$$

This means that only two of these quantities may be varied at the same time, and the other must be held constant.

There are other thermodynamic functions besides the internal energy that are often convenient to work with. These are the enthalpy H, the Helmholtz function A, and Gibb's function G whose differentials are given by

$$dH = d(U + PV) = TdS + VdP \tag{2.7}$$

$$dA = d(U - TS) = -SdT - PdV \tag{2.8}$$

$$dG = d(U - TS + PV) = -SdT + VdP. \tag{2.9}$$

The above relations are just a reformulation of expressing the internal energy under various conditions.

2.2 Heat Capacity

2.2.1 The Law of Dulong and Petit

We start with the application of equipartition of energy, which states that for each degree of freedom there is $\frac{1}{2}k_BT$ of energy. From just the translational degrees of freedom we get $\frac{3}{2}k_BT$ of energy per atom. Energy added to solids takes the form of atomic vibrations and that contributes three additional degrees of freedom and a total energy per atom of $3k_BT$. The specific heat at constant volume should be just the rate of change with temperature (temperature derivative) of that energy.

$$Energy\ (per\ mole) = 3N_Ak_BT \tag{2.10}$$

where k_B is Boltzmann's constant, T is the Temperature in Kelvin, and N_A is Avogadro's number. It follows that,

$$\begin{aligned} C_V &= \frac{\partial}{\partial T}\left(3N_Ak_BT\right) \\ &= 3N_Ak_B\ mole^{-1} \\ &= 24.94\ J\ mole^{-1}\ K^{-1}. \end{aligned} \tag{2.11}$$

This is known as the law of Dulong and Petit, after the scientists credited with its discovery. [32] This analysis holds for a large number of materials at room temperature. However, at low temperatures the specific heat falls off quite rapidly and approaches zero as the temperature approaches zero on the Kelvin scale.

2.2.2 Einstein Model of the Lattice Heat Capacity

Einstein is mainly remembered for his contributions of special and general relativity. One of the lesser known great contributions he gave to physics was to explain the deviation of specific heats at low temperatures from the law of Dulong and Petit. Dulong and Petit had assumed that Maxwell-Boltzmann statistics were valid at all temperatures and had used those statistics and the equipartition of energy to form their famous result. In the early 1900s, Einstein took a different approach. [33] Say there are N atoms in a lattice. He treated them as a set of $3N$ independent harmonic oscillators in one dimension, giving each an identical frequency ν. He then *quantized* the energy of the oscillators following the work of Planck 11 years earlier in 1900. According to Planck the energy E may only take on the values

$$E = nh\nu, \quad n = 0, 1, 2, ...$$

where n is a positive integer, ν is the frequency, and h is Planck's constant. Modern literature often quotes the above relation in a slightly modified manner,

$$E = n\left(\frac{h}{2\pi}\right)(2\pi\nu) = n\hbar\omega \tag{2.12}$$

where n is an integer, ω is the angular frequency, and $\hbar$ is the reduced Planck Constant, which has a value of $1.054\,571\,800 \times 10^{-34}\,\mathrm{J\,s^{-1}}$.

Classically, the average energy of a harmonic oscillator is just $\bar{E} = k_B T$. Clearly this isn't the case when using the discrete quantized values suggested by Planck. For this Einstein turned to the Boltzmann distribution law (also known as Gibb's distribution). According to this distribution

the ratio of populations in thermal equilibrium of two adjacent energy levels ($n' = n + 1$) is $e^{-(E_{n'}-E_n)/k_BT} = e^{-\hbar\omega/k_BT}$. The average energy is then

$$\begin{aligned}\bar{E} &= \frac{\sum_{n=0}^{\infty} n\hbar\omega e^{-n\hbar\omega/k_BT}}{\sum_{n=0}^{\infty} e^{-n\hbar\omega/k_BT}} \\ &= \frac{\hbar\omega\left(e^{-\hbar\omega/k_BT} + 2e^{-2\hbar\omega/k_BT} + \dots\right)}{(1 + e^{-\hbar\omega/k_BT} + e^{-2\hbar\omega/k_BT} + \dots)}\end{aligned}$$

where the denominator normalizes the distribution. Changing variables to $x = -\hbar\omega/k_BT$ and rearranging, we have

$$\begin{aligned}\bar{E} &= \hbar\omega\frac{d}{dx}log\left(1 + e^x + e^{2x} + \dots\right) \\ &= \hbar\omega\frac{d}{dx}log\frac{1}{1-e^x} = \frac{\hbar\omega}{e^{-x}-1}\end{aligned}$$

resulting in the final expression

$$\bar{E} = \frac{\hbar\omega}{e^{\hbar\omega/k_BT} - 1}. \tag{2.13}$$

At higher temperatures (where $k_BT >> \hbar\omega$) the denominator can be Taylor expanded as

$$e^{\hbar\omega/k_BT} - 1 = 1 + \left(\frac{\hbar\omega}{k_BT}\right) + \dots - 1 \cong \frac{\hbar\omega}{k_BT}$$

which reduces 2.13 to $\bar{E} = k_BT$. This is just the classical average energy k_B!! So at high temperatures the method of Einstein gives the classical result, but at low temperatures it adds new features. At low temperatures (where $k_BT << \hbar\omega$) the term $e^{\hbar\omega/k_BT} >> 1$ and dominates the expression. It is therefore reasonable to approximate the average energy at low temperatures by

$$\bar{E} \cong \hbar\omega e^{-\hbar\omega/k_BT}. \tag{2.14}$$

Therefore, as $T \rightarrow$zero, the heat capacity approaches zero as

$$C_V \cong Nk\left(\frac{\hbar\omega}{k_BT}\right)^2 e^{-\hbar\omega/k_BT}. \tag{2.15}$$

In the above expression, the exponential factor dominates over the T^{-2} term. The conclusion is that the heat capacity in the Einstein model varies as $e^{-\hbar\omega/k_BT}$ in this, the low-temperature limit. Sadly Einstein's model does not fit perfectly with experimental observations. The true low-temperature behavior of the lattice specific heat shows a T^3 dependence, not exponential as predicted in this model.

Despite the difference in the Einstein model from true behavior, the model gives a generally good description of the behavior of the heat capacity at low temperatures. The "goodness" of the description relies on the appropriate choice of adjustable parameters. A good fit is one that minimizes the difference between the model and experimental values. Being an extremely simple model, the adjustable parameter is just the oscillator frequency ω. However, results are often discussed in terms of a characteristic temperature Θ_E, known as the Einstein temperature, defined as

$$\hbar\omega = k_B\Theta_E. \tag{2.16}$$

The full expression for the heat capacity in terms of the Einstein temperature is given by

$$\begin{aligned} C = \frac{\partial U}{\partial T} = \frac{\partial\left(N\bar{E}\right)}{\partial T} &= Nk_B\left(\frac{\hbar\omega}{k_BT}\right)^2\frac{e^{\hbar\omega/k_BT}}{\left(e^{\hbar\omega/k_BT}-1\right)^2} \\ &= Nk_B\left(\frac{\Theta_E}{T}\right)^2\frac{e^{\Theta_E/T}}{\left(e^{\Theta_E/T}-1\right)^2} \end{aligned}. \tag{2.17}$$

2.2.3 Debye Model of the Lattice Heat Capacity

Einstein started with the assumption that all the harmonic oscillators were independent and shared a single characteristic frequency. While this was a major step forward in understanding the quantum nature of the heat capacity it doesn't give an accurate description of the low-temperature behavior. Einstein himself was aware of this fact. In real materials the theoretical ideal of independent harmonic motion of the atoms is clearly not going to be true. Since the low-temperature limit is described by the mathematical relation $k_BT << \hbar\omega$ it's easy to see that low frequency/long wavelength motions will dominate. This is often described as the high frequency modes being

"frozen out." Therefore it's unreasonable to assume that the motions of the lattice can be ascribed to a single characteristic frequency. These failures of the Einstein model were improved upon by the models of Debye and Born and von Kármán in 1912. [34, 35]

In deriving the Debye model it is usual to suppose that of the $3N$ normal modes of lattice vibration there are $g(\omega)d\omega$ modes in the range ω to $\omega + d\omega$. Summing over all the modes in a continuous fashion gives a total lattice energy of

$$U = \int \frac{\hbar\omega}{e^{\hbar\omega/k_B T} - 1} g(\omega) d\omega. \tag{2.18}$$

The problem of calculating the energy or subsequently any thermodynamic functions is reduced to calculating $g(\omega)$, known as the frequency spectrum or density of states.

During the time these theories were developed there were no computers and calculations were performed by hand. For real materials the calculations could be incredibly difficult, time consuming and tedious. Of course now, while still not trivial, these problems are performed using computational physics. Born and von Kármán's approach was the more complicated of the two, and so Debye's model, with it's incredible simplicity, became the go to method.

Debye's method relies on the fact stated above that as the temperature decreases the low frequency modes dominate. In solids the low frequency modes are the acoustic oscillations. Acoustic oscillations are of long wavelength and are much larger than the atomic dimensions of the crystal lattice. This allows the ideas of an elastic continuum to be used. Debye assumed a monatomic, homogeneous, and isotropic solid with the added condition that there are only $3N$ available modes. Once the $3N$ modes are filled the modes are then cut off. Alternatively this means that there is some maximum frequency allowable, known as the Debye frequency.

In order to solve this problem Debye assumed that solutions to the differential equations had a linear dispersion relation, i.e. that the frequency was linearly proportional to the wave number k. Assuming the proportionality constant is the velocity of sound in the crystal, c, we should have

$\omega = ck$ and $dk/d\omega = 1/c$, so that per unit volume

$$g(\omega) = \frac{3}{2\pi^2 c} k^2 = \frac{3}{2\pi^2 c^3} \omega^2. \tag{2.19}$$

This relation is based on the plane wave solution of the differential equation for an acoustic wave in a cube and can be easily derived, or found elsewhere.

In elastic solids, there are three possible types of waves. There can be a longitudinal wave of velocity c_L and two transverse shear waves both with velocity c_T. Modifying the frequency spectrum accordingly gives

$$g(\omega) = \frac{\omega^2}{2\pi^2} \left(\frac{1}{c_L^3} + \frac{2}{c_T^3} \right). \tag{2.20}$$

For simplicity the rest of the derivation uses 2.19, but can be derived using this relation with more effort.

The internal energy is then given by

$$U = \frac{3\hbar}{2\pi^2 c^3} \int_0^{\omega_D} \frac{\omega^3}{e^{\hbar\omega/k_B T} - 1} d\omega. \tag{2.21}$$

The condition for the cut off or Debye maximum frequency ω_D is that

$$\int_0^{\omega_D} g(\omega) d\omega = \frac{3}{2\pi^2 c^3} \int_0^{\omega_D} \omega^2 d\omega = 3N \tag{2.22}$$

which evaluated gives

$$\frac{\omega_D^3}{2\pi^2 c^3} = 3N \tag{2.23}$$

or finally

$$\omega_D = c \left(6\pi^2 N \right)^{1/3}. \tag{2.24}$$

Is this reasonable? Recall that the wavelength is given by $2\pi/k$. The wavenumber is usually

measured in cm^{-1} and estimating a number of modes as 10^{23} the minimum wavelength would be

$$\lambda \sim \frac{2\pi\ cm}{\left(6\pi^2\ 10^{23}\right)^{1/3}} \sim 3.5\,\text{Å}. \tag{2.25}$$

This value is on the order of atomic spacing, and is reasonable based on Debye's criteria for the wavelength.

As with the Einstein model, changing variables to $x = \hbar\omega/k_BT$ changes the internal energy to the form

$$U = 9Nk_BT\left(\frac{T}{\Theta_D}\right)^3 \int_0^{x_{max}} \frac{x^3}{e^x - 1}dx \tag{2.26}$$

where

$$x_{max} = \frac{\hbar\omega_D}{k_BT} \ = \left(\frac{\hbar c}{k_BT}\right)\left(6\pi^2 N\right)^{1/3} = \frac{\Theta_D}{T}, \tag{2.27}$$

gives the definition of the Debye characteristic temperature Θ_D. Performing the derivative to get the heat capacity we find

$$C_V = 9Nk_B\left(\frac{T}{\Theta_D}\right)^3 \int_0^{x_{max}} \frac{x^4 e^x}{\left(e^x - 1\right)^2}dx. \tag{2.28}$$

In the high temperature limit, $T >> \Theta_D$, x is small and so we can take the approximation $e^x \approx 1 + x$, then the internal energy becomes

$$\begin{aligned} U &= 9Nk_BT\left(\frac{T}{\Theta_D}\right)^3 \int_0^{x_{max}} x^2 dx \\ &= 9Nk_BT\left(\frac{T}{\Theta_D}\right)^3 \frac{1}{3}\left(\frac{\Theta_D}{T}\right)^3 \\ &= 3Nk_BT \end{aligned} \tag{2.29}$$

and the heat capacity becomes

$$C_V = \frac{\partial U}{\partial T} = 3Nk_B, \tag{2.30}$$

where we again obtain the law of Dulong and Petit.

In the low temperature limit, $T << \Theta_D$, x_{max} can be approximated as approaching infinity such that

$$\int_0^\infty \frac{x^3}{e^x - 1} dx = 6\zeta(4) = 6\sum_0^\infty \frac{1}{n^4} = \frac{\pi^4}{15} \tag{2.31}$$

where $\zeta(4)$ is the Riemann zeta function. Thus for $T << \Theta_D$,

$$U = \frac{3}{5}\pi^4 N k_B \left(\frac{T^4}{\Theta_D^3}\right) \tag{2.32}$$

giving the heat capacity as

$$C_V = \frac{\partial U}{\partial T} = \frac{12}{5}\pi^4 N k_B \left(\frac{T}{\Theta_D}\right)^3. \tag{2.33}$$

Here is where the Debye model shines, the heat capacity is correctly described as a T^3 law at low temperatures and is based on a single adjustable parameter, Θ_D.

Debye's model is extremely successful at fitting data for a wide variety of materials at low to moderate temperatures. However, it is not without some faults. The periodicity of the lattice causes the medium to be dispersive; i.e. the velocity of wave propagation is frequency dependent. In real materials this means that the Debye function doesn't fit the data perfectly without evaluating Θ_D at each temperature. In practice, as the temperature is lowered, the value of Θ_D begins to decrease around $\Theta_D/2$, has a minimum, and then rises to a constant value below $\Theta_D/50$. Therefore the Θ_D values calculated from the T^3 dependence are only truly valid below $\Theta_D/50$. The model of Born and von Kármán avoided these pitfalls, as Blackman later showed[36], but the simplicity of Debye's model won the day and continues to be the preferred method of analysis even today.

2.2.4 The Diatomic Lattice

Up until this point the lattice of atoms has been assumed to be monatomic. Most of the interesting materials under study today are made up of a handful of different atoms. The theory of lattice dynamics of these polyatomic materials are beyond the scope of this document and won't be covered here, but we can easily extend the discussion so far to a lattice of two different atoms.

Calculation of the exact solution to a diatomic lattice is more suited to a theoretical work and won't be done here. However, if the two atomic masses are very different, say $m >> M$ we can use an approximation. If $m >> M$ then the optical branch of modes won't vary too much and can be treated like it's nearly constant. The optical mode can then be approximated as a set of harmonic oscillators having a frequency

$$\omega_0 \cong \left[2\beta\left(\frac{1}{m}+\frac{1}{M}\right)\right]^{1/2} \cong [2\beta/M]^{1/2} \tag{2.34}$$

where β is a force constant relating the elastic stiffness to the lattice spacing. In this scheme we can then treat the optical modes using the Einstein model while using the Debye model for the acoustic modes. Modern analysis does exactly this, where the experimental heat capacity is fit to a combination of the Enstein and Debye models.

2.2.5 Heat Capacity of Conduction Electrons

So far the discussion presented here has only touched on the lattice vibrations, also known as phonons, contribution to the heat capacity. The materials in this study are non-conductive, and so one might imagine that we could skip talking about the electronic contributions. However, without developing the theory of free electrons in a metal, I will briefly discuss their contribution to the heat capacity so that we can convince ourselves later that there is no electronic contributions. For free electrons their dynamics are that of free classical particles. In this approximation, the electron 'gas' has 3 degrees of freedom and would make a contribution of $C_{(el)} = \frac{3}{2}Nk_B$ to the heat capacity. Here, N is the number of electrons per unit volume and not Avogadro's number. If $N = N_A$, then at high temperatures it would be reasonable to expect a total heat capacity (phonon and electron) of $\frac{9}{2}N_Ak_B$. In reality, the total heat capacity of almost all materials at high temperatures doesn't deviate from the law of Dulong and Petit. That is to say the total heat capacity is still just $3N_Ak_B$ and the electrons do not contribute to the total at high temperatures.

The underlying reason that the electrons do not contribute significantly to the heat capacity at high temperatures is ultimately a consequence of the Pauli exclusion principle. The argument for

the effect of the Pauli exclusion principle's effect on the contribution to the heat capacity will only be outlined here. The full derivation is rather involved and won't be presented, but can easily be found in the literature. The Pauli exclusion principle states that each electron can only occupy a single quantum state, and therefore unlike a classical gas cannot all have the same energy. The energy is quantized and each energy level can hold only a certain number of electrons, i.e. the ground state can hold a maximum of 2, the first excited state can hold a maximum of 12, etc. Depending on the number of electrons available some states will be filled and others will be empty. The level which divides the filled and vacant states is known as the Fermi level (after Enrico Fermi) at absolute zero or $E_F(0)$.

Upon heating from absolute zero, only a small portion of electrons gain an energy of $\sim k_B T$ as happens classically. Instead only the electrons already within an energy range on the order of $k_B T$ can be thermally excited. This fraction is on the order of T/T_F, where $T_F = E_F(0)/k_B$, and each gain an energy also on the order of $k_B T$. For N total electrons the thermal energy U is then of the order $NT/T_F \times k_B T = N k_B T^2/T_F$. The electronic heat capacity is then

$$C_V = \frac{\partial U}{\partial T} \approx \frac{N k_B}{T_F} T.$$

T_F is on the order of $5 \times 10^4\,\mathrm{K}$, and so even at room temperature the contribution to the total heat capacity is small. The full result for a free electron of mass m is

$$C_{V(el)} = \gamma T; \quad \gamma = \pi^2 N^{1/3} k_B m/(3\pi^2)^{2/3}\hbar^2. \tag{2.35}$$

At sufficiently low temperatures, usually below $4\,\mathrm{K}$, the electronic contribution becomes dominant over the phonon contribution. Recall the phonon contribution decreases as T^3 at low temperatures, where the electronic contribution is linear in T. Then the low temperature limit of the heat capacity is

$$C_V = \alpha T^3 + \gamma T \tag{2.36}$$

where α is a constant and is given in equation (2.33).

2.2.6 Schottky Anomalies

The simple models proposed by Einstein and Debye have been very successful at describing the physical behavior of the heat capacity. The fact that they are in use over 100 years later is a testament to that success. Yet there are other contributions to the heat capacity observed in experimental data that they don't predict. Many of these deviations from the expected theory were originally classified as "anomalous" as they deviated from the "normal" behavior expected. This description has remained even though many of the "anomalies" are now well understood and are expected normal behavior. It is best to remember that the theory presented here is only a simple model, and therefore only an approximation of true results.

As an example of these deviations, suppose there is a system in which the particles can exist in a group of m energy levels, separated from the ground state by energies $\varepsilon_1, \varepsilon_2, \ldots, \varepsilon_m$ and with degeneracies $g_1, g_2, \ldots, g_m$. The probability of a particle occupying the ith level is

$$\frac{g_i e^{-\varepsilon_i/k_B T}}{\sum\limits_n g_i e^{-\varepsilon_i/k_B T}}$$

in accordance with the Boltzmann distribution. The mean energy at temperature T for N independent particles is then

$$E = \frac{N \sum\limits_{i=0}^{m} \varepsilon_i g_i e^{\varepsilon_i/k_B T}}{\sum\limits_{i=0}^{m} g_i e^{\varepsilon_i/k_B T}} \tag{2.37}$$

The specific heat is then calculated in the usual fashion, by taking the derivative dE/dT. This general problem was solved by Schottky in 1922, [37] and so heat capacities of multilevel systems are referred to as Schottky anomalies in his honor. The full calculation for multiple levels is quite tedious, but a simple two-level system is easy to do. For the simple case of two levels equation (2.37) becomes

$$E = \frac{N \varepsilon_1 g_1 e^{\varepsilon_1/k_B T}}{g_0 + g_1 e^{\varepsilon_1/k_B T}}$$

and so the Schottky specific heat is then

$$\begin{aligned} C_{Sch} &= \frac{N\varepsilon_1^2}{k_B T^2}\frac{g_0}{g_1}\frac{e^{-\varepsilon_1/k_B T}}{[1+(g_0/g_1)e^{-\varepsilon_1/k_B T}]^2} \\ &= R\left(\frac{\delta}{T}\right)^2 \frac{g_0}{g_1}\frac{e^{-\varepsilon_1/k_B T}}{[1+(g_0/g_1)e^{-\varepsilon_1/k_B T}]^2} \end{aligned} \tag{2.38}$$

where $\delta = \varepsilon_1/k_B$ is the difference in energy between the two levels, measured in Kelvin. At $T \ll \delta$, the upper level will have a small population, where at $T \gg \delta$ both levels will be nearly equal in population. It is only at $T \approx \delta$ that there will be transitions from one level to another in any appreciable amount. This manifests as a large hump in the specific heat, which can be separated out from the lattice or electronic contributions. The quantitative form is such that

$$C_{Sch} = R\left(\frac{g_0}{g_1}\right)\left(\frac{\delta}{T}\right)^2 e^{-\delta/T} \qquad T \ll \delta \tag{2.39}$$

$$= R g_0 g_1 (g_0+g_1)^{-2}\left(\frac{\delta}{T}\right)^2 \qquad T \gg \delta \tag{2.40}$$

where it is easy to see that the Schottky heat capacity goes to zero at the extremes of either low or high temperature. C_{Sch} obtains a maximum value at an intermediate temperature T_m which obeys the relation

$$\left(\frac{g_0}{g_1}\right)e^{\delta/T_m} = \frac{(\delta/T_m)+2}{(\delta/T_m)-2} \tag{2.41}$$

where the maximum value is itself

$$C_{Sch}(T_m) = \frac{R}{4}\frac{T_m}{\delta}\left[\left(\frac{\delta}{T_m}\right)^2 - 4\right]. \tag{2.42}$$

Recall this is only for a two level system, and if there are more degenerate levels the full equations must be used. It is further possible to use these relations to determine δ and g_0/g_1 from experimentally observed values of the specific heat. However, it is difficult for most real materials due to many contributions to the specific heat. C_{Sch} cannot always be easily separated from the lattice, electronic, or other contributions.

2.3 Thermal Conductivity of Solids

Thermal Conductivity is a measure of how much heat can flow through a substance without appreciable displacement of its constituent particles. This transfer of heat through a material can occur regardless of the form of the material, whether its a solid, liquid, or gas. For solid materials, the heat transfer is most easily defined with a steady state of flow down a long rod where there is a temperature gradient along the rod. This set up follow's Fourier's heat equation,

$$\dot{Q} = \kappa \frac{A}{L} \Delta T, \tag{2.43}$$

where $\dot{Q}$ is a heat flux, ΔT is the change in temperature measured across length L, of cross-sectional area A, and κ is the thermal conductivity.

For most solids there are two main carriers available to transfer the heat. Free electrons are the primary heat carrier in metals, and for non-metals the heat is carried by lattice waves, better known as phonons. Phonons themselves are bosons (have integer spin), and obey Bose-Einstein statistics. The details and derivations are found in any text of statistical mechanics and won't be repeated here. The normal way to envisage the movement of phonons throughout a solid is the phonon gas model. The phonons themselves can be thought of as an ideal gas in an enclosed container where the phonons are the particles of the gas and the solid itself is the container. In this way the standard analysis of random processes can be applied so that the heat is carried by the phonons through a material as they experience frequent scattering and deflection.

As with a classical gas, we can assume a mean free path of the phonons given by $\ell = u\tau$ where ℓ is the average distance traveled between collisions, u is the average velocity of the phonon, and τ is the time between collisions. Assuming the material is the same in all directions, or isotropic, then $\ell^2 = \Delta x^2 + \Delta y^2 + \Delta z^2 = 3\Delta x^2$ where we can limit ourselves to one dimension Δx, as $\Delta x = \Delta y = \Delta z$.

With a little bit of non-rigourous and creative re-arranging we see that,

$$\frac{1}{\tau} = \frac{1}{3} u \frac{\ell}{\Delta x^2}, \tag{2.44}$$

and we can re-arrange 2.43 replacing L with Δx such that

$$\kappa = \frac{1}{\tau} \frac{Q}{\Delta T} \frac{\Delta x}{A} = \frac{1}{3} u \frac{\ell}{\Delta x^2} \frac{Q}{\Delta T} \frac{\Delta x}{A} \tag{2.45}$$

and using $\frac{Q}{V} = \frac{Q}{\Delta x A} = C_V \Delta T$, we finally arrive at the classical result that

$$\kappa = \frac{1}{3} C_V u \ell. \tag{2.46}$$

Note that this is making a large number of assumptions, particularly that the mean free path is on the order of the sample dimensions, and is not mathematically rigorous, but we can use this result as a sanity check to see if the phonon gas model is reasonable. Since we obtain the classical result for a gas, we conclude that this model is reasonable as long as the assumed conditions of the model hold. This isn't always the case, and to obtain the true relation between the thermal conductivity, κ, and the heat capacity, C_V, one must go through the full mathematical rigor. As this isn't truly practical for this experimental work, the full statistical derivation will be omitted and any reader is encouraged to explore the topic in the standard literature.

The important takeaway is that the thermal conductivity can be expected to vary proportionally to the heat capacity at low temperatures and should take a T^3 dependence as shown in equation 2.33 of the Debye heat capacity model.

2.4 The Klemens-Callaway Model

A simple model for thermal conductivity at low temperatures is the Klemens-Callaway model (KCM) [38]. The full model won't be covered here, but briefly introduced. To solve the Boltzmann transport equation, this model assumes a Debye phonon dispersion relation and utilizes a relaxation

time approximation. The thermal conductivity as a function of temperature T is then given by

$$\kappa = \kappa_1 + \kappa_2 \tag{2.47a}$$

$$\kappa_1 = \frac{k_B}{2\pi v}\left(\frac{k_B T}{\hbar}\right)^3 \int_0^{\Theta_D/T} \tau_c \frac{x^4 e^x}{\left(e^x - 1\right)^2} dx \tag{2.47b}$$

$$\kappa_2 = \frac{k_B}{2\pi v}\left(\frac{k_B T}{\hbar}\right)^3 \frac{\left(\beta \int_0^{\Theta_D/T} \frac{\tau_c}{\tau_U} \frac{x^4 e^x}{(e^x-1)^2} dx\right)^2}{\int_0^{\Theta_D/T} \frac{1}{\tau_U}\left(1 - \frac{\beta\tau_c}{\tau_U}\right) \frac{x^4 e^x}{(e^x-1)^2} dx} \tag{2.47c}$$

where β is the ratio of nomal to Umklapp processes, v is the mean velocity of sound in the solid, τ_c is the phonon relaxation time due to combined normal and Umklapp processes, τ_U is the phonon relaxation time due to Umklpapp processes, $x = \hbar\omega/k_B T$ is the reduced phonon frequency, ω, k_B, $\hbar$, and Θ_D are as defined previously.

The second Callway term k_2 is often neglected as it only becomes large enough to contribute to the overall thermal conductivity in very pure crystals. Most materials, and the materials studied in this work, have a large number of defects and so this term can safley be neglected such that $\kappa \approx \kappa_1$.

There are many nuances to these models and more advanced models have been developed, but as we'll see the experimental data in this work is well fitted to this simple model.

3. EXPERIMENTAL METHODS[1]

3.1 The Quantum Design Physical Properties Measurement System

All measurements in this study were made using a Quantum Design (QD) Physical Properties Measurement System (PPMS). The PPMS is a customizable automated cryostat system that can be operated from 1.8 to $400\,\mathrm{K}$. Quantum Design provides a number of different options depending on the needs of the user. Our PPMS is equipped with resistivity, torque magnetometry, a.c. transport, heat capacity, and thermal transport options. It is also equipped with an activated charcoal cryopump for the high vacuum required in the heat capacity and thermal transport options as well as a $9\,\mathrm{T}$ longitudinal magnet. Only those options with relevance to this work will be covered here.

The heat capacity option uses relaxation calorimetry to measure the heat capacity of samples. It is also capable of using a variation of relaxation calorimetry called the Dual-Slope technique which will be covered in section 3.2.3. Other methods of measuring heat capacity such as a.c. calorimetry and differential scanning calorimetry are beyond the scope of this work. Details of how the heat capacity option operates will be given in sections 3.2.1, 3.2.2, and 3.2.3. Equipment specific to this option will be covered in section 3.2.4. Methods of sample preparation for heat capacity measurements are discussed in chapter 4, section 4.2. The resolution of the system is $10\,\mathrm{nJ\,K^{-1}}$ at $2\,\mathrm{K}$. A detailed evaluation of the accuracy of using the PPMS for heat capacity measurements was published by Lashley *et al.* in 2003 [39]. Their results showed that the accuracy is $1\,\%$ above $10\,\mathrm{K}$, which decreases to about $5\,\%$ below $5\,\mathrm{K}$.

The thermal transport option (TTO) enables measurements of thermal properties, other than heat capacity, including thermal conductivity κ, and the thermopower (or Seebeck coeffecient) α, over the entire temperature and magnetic field range of the PPMS. This option can also measure electical resistivity ρ using the a.c. transport option hardware. Combining all of the above measurements the PPMS can assess the thermoelectric figure of merit, $ZT = \alpha^2 T/\kappa\rho$, which is the

[1]Part of this chapter includes text and images from Quantum Design user manuals. Text and images taken from Quantum Design user manuals are used with permission, © 2021 Quantum Design, Inc.

main quantity of interest in investigating thermoelectric materials. Normal operation of the TTO uses a pulse power method to measure the thermal conductivity; however, it can be set up using the traditional steady state technique. Operational details will be discussed in sections 3.3.1 and 3.3.2. The hardware required for this option will be presented in section 3.3.3. Sample preparation methods for the thermal conductivity measurements are given in chapter 4 section 4.3.

3.2 Heat Capacity

This section will give a brief background of relaxation calorimetry, introduce the theoretical models used by the PPMS in measuring heat capacity, cover the heat capacity option hardware, and describe methods of sample preparation for heat capacity measurements in the PPMS.

While the origin of modern calorimetry can be traced to the 18th century with the work of Black[40], followed subsequently by Lavoisier and Laplace[41], it wasn't until the twentieth century with the pioneering work of Eucken [42] and Nernst [43] that we see the adiabatic calorimetry we use today. The current standard is the thermal relaxation technique, which was developed by Bachmann *et al.* in 1972 [44]. This technique has proven to be immensely popular in condensed-matter research and has spawned a variety of calorimeters based on thermal relaxation [45, 46, 47, 48, 49]. Part of the popularity of this technique is that this adiabatic measurement approach relies directly on the classical definition of the heat capacity,

$$C_p = \lim_{dT \to 0} \left(\frac{dQ}{dT} \right)_p \tag{3.1}$$

where dQ is the heat input to the system and dT is the corresponding temperature rise in the measured sample.

3.2.1 Simple Model

The PPMS will first attempt to use a simple model to calculate the heat capacity during measurements. This model assumes that the sample is in good thermal contact with the platform, i.e. that both platform and sample are at the same temperature during measurement. It is also assumed that the temperature change is small.

In general, a relaxation calorimeter operating semi-adiabatically measures the total heat capacity (sample and addenda) by using a simple relation,

$$C_{total} = K \cdot \tau, \tag{3.2}$$

where K is the thermal conductance of the weak link between a sample platform and a thermal bath and τ is the constant of the temperature relaxation time between the platform and bath.

Since the PPMS uses this technique for heat capacity measurement we can describe the temperature T of the platform as a function of time t. This function obeys the equation,

$$C_{total}\frac{dT}{dt} = P(t) - K_w(T(t) - T_b), \tag{3.3}$$

where C_{total} is the total heat capacity of the sample and platform; K_w is the thermal conductance of the supporting wires; T_b is the temperature of the thermal bath (puck frame); and $P(t)$ is the power applied by the heater. Equation 3.3 is a simple heat balance equation where the rate of heating is expressed on the left hand side of the equation and is balanced by the heater power minus the heat loss through the wires on the right. A schematic of the experimental set up can be seen in figure 3.1 along with its corresponding equivalent electronic circuit in figure 3.2.

To measure the heat capacity, the PPMS applies a square heat pulse to the sample. After the heater power is turned off the sample temperature relaxes toward the temperature of the thermal bath. The software then uses a least-squares curve fitting technique where the measured response curve is compared to the solution of equation 3.3.

During the heating portion of the measurement, the heater power $P(t)$ is equal to a constant P_0, where during the cooling portion it is zero. This condition can be mathematically stated as

$$P(t) = \begin{cases} P_0 & (0 \leq t \leq t_0) \\ 0 & (t > t_0) \end{cases}. \tag{3.4}$$

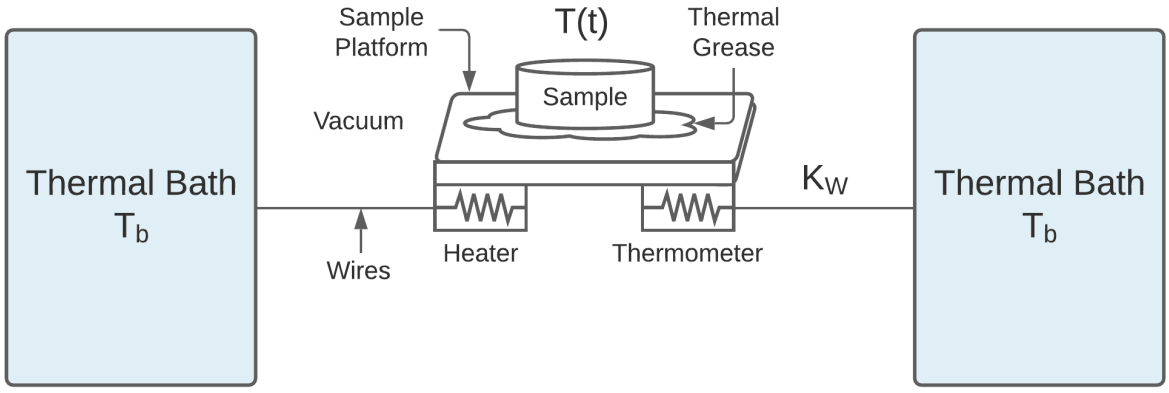

Figure 3.1: Schematic of the experimental apparatus used to measure heat capacity in the PPMS. Adapted from Quantum Design user training material.

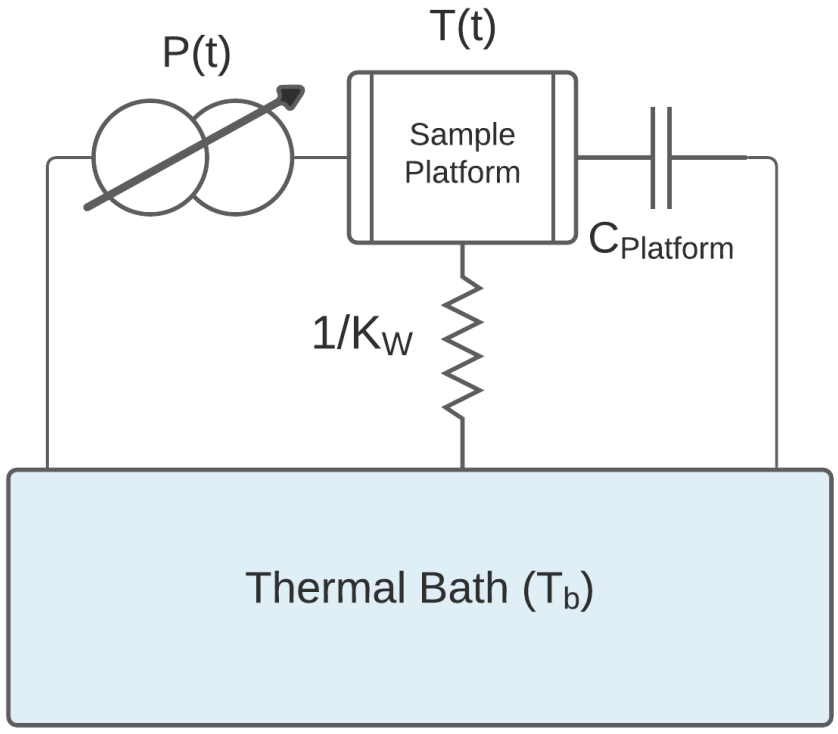

Figure 3.2: Circuit equivalent of the simple model for heat capacity. Adapted from Quantum Design user training material.

When the power is switched off at time t_0 the solution to equation 3.3 is subjected to Dirichlet boundary conditions such that $T_{on}(t_0) = T_{off}(t_0)$. Since the power given in equation 3.4 is piecewise constant, the solution to the differential equation 3.3 takes on a closed-form expression,

$$T(t) = \begin{cases} P_0\tau(1 - e^{-t/\tau})/C_{total} + T_b & (0 \leq t \leq t_0) \\ P_0\tau(1 - e^{-t_0/\tau})e^{-(t-t_0)/\tau}/C_{total} + T_b & (t > t_0) \end{cases}, \tag{3.5}$$

where $\tau = C_{total}/K_w$. P_0 and t_0 are known values controlled by the software. This is illustrated in figure 3.3.

The software can then adjust the parameters C_{total}, K_w, and T_b to optimize the curve fit. The least-squares method finds its optimum when the sum, S_{LS}, of squared residuals is a minimum. For this application the sum is given by,

$$S_{LS}(C_{total}, K_w, T_b) = \sum_i (T(t_i) - T_i)^2, \tag{3.6}$$

where the t_i are the measured times and T_i the corresponding measured temperatures. The PPMS applies this simple model to measure addenda and in general for most samples.

At very low temperatures, and with certain samples, the thermal resistance between the sample and the platform can no longer be neglected. This introduces another degree of freedom to the model which can be included by adding a second time constant.

3.2.2 Two-tau Model™

For many cases, good results are obtained using the simple model discussed above. The two-tau model[2] is a more complicated fitting model used when thermal coupling between the sample to be measured and platform is poor. Poor coupling can occur when the thermal conductance of the sample or the grease used to bond the sample to the platform is small relative to that of the heat leak through the connecting wires or if the heat capacity of the wires is significant. Samples with

[2]Two-tau model™ is a trademark of Quantum Design. Text and images taken from Quantum Design user manuals are used with permission, © 2021 Quantum Design, Inc.

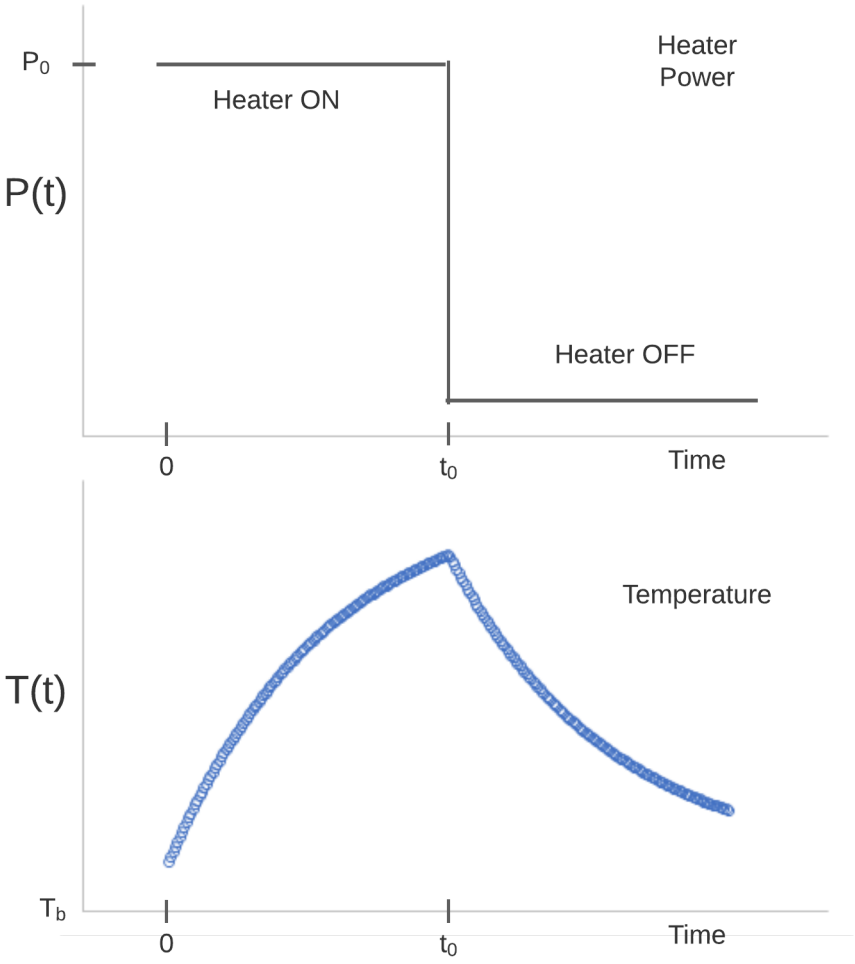

Figure 3.3: Idealized heat pulse and temperature response from a sample studied in this work during heat capacity measurement. A square-pulse of height P_0 is applied (upper diagram), resulting in a temperature change of the sample and platform (lower diagram). The temperature curve is raw data of a typical response from those studied in this work. Adapted from Quantum Design user training material.

a thermal conductance comparable to the connecting wires will have regions of the sample with different temperatures. $T(t)$ must then be represented by a sum of exponentials with different time constants [44]. Alternatively, an impedance mismatch between the sample, grease, and platform would also require a sum of exponentials. Poor coupling is usually characterized by cooling curves with an abnormally high initial slope compared to the rest of the decay [50].

The two-tau model uses a modified technique initially developed by Hwang *et al.* [51]. They examine the scenario of an impedance mismatch. The poor thermal coupling is treated as two heat flows, one between the sample and platform, then one between the platform and thermal bath as seen in figure 3.4.

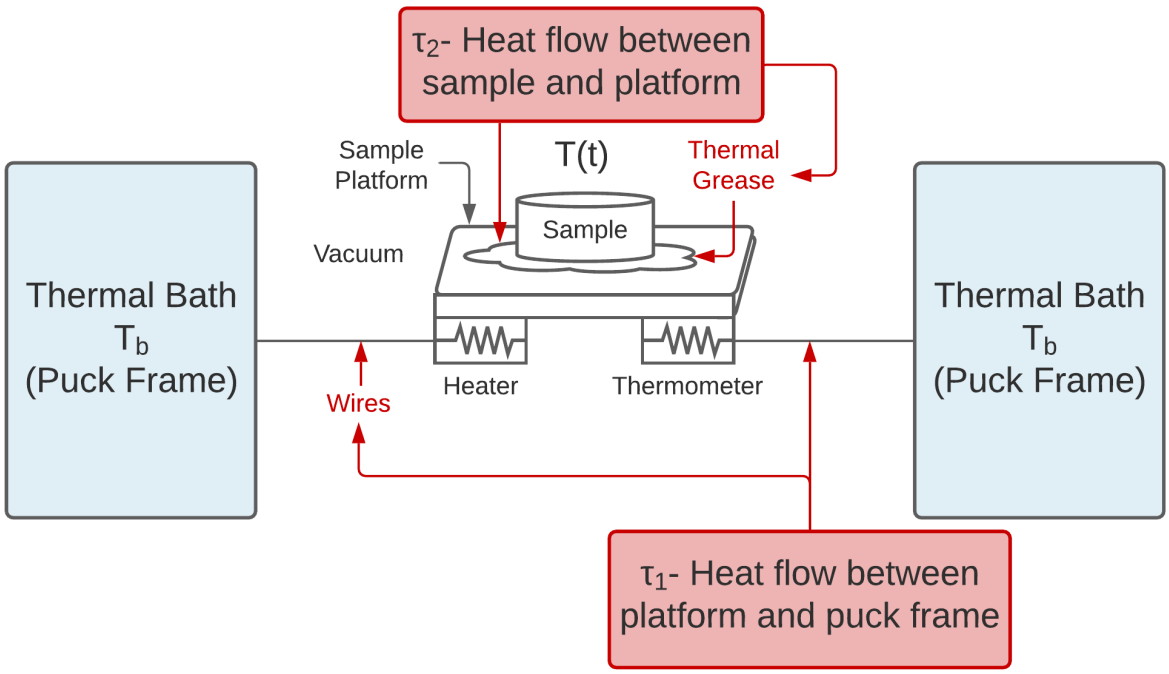

Figure 3.4: Schematic of the experimental apparatus used to measure heat capacity in the PPMS showing the two-tau model. Adapted from Quantum Design user training material.

Since the heat flow is split into two separate terms, we must also split the heat capacity into separate terms where $C_{total} = C_{platform} + C_{sample}$. An equivalent circuit diagram is given in figure

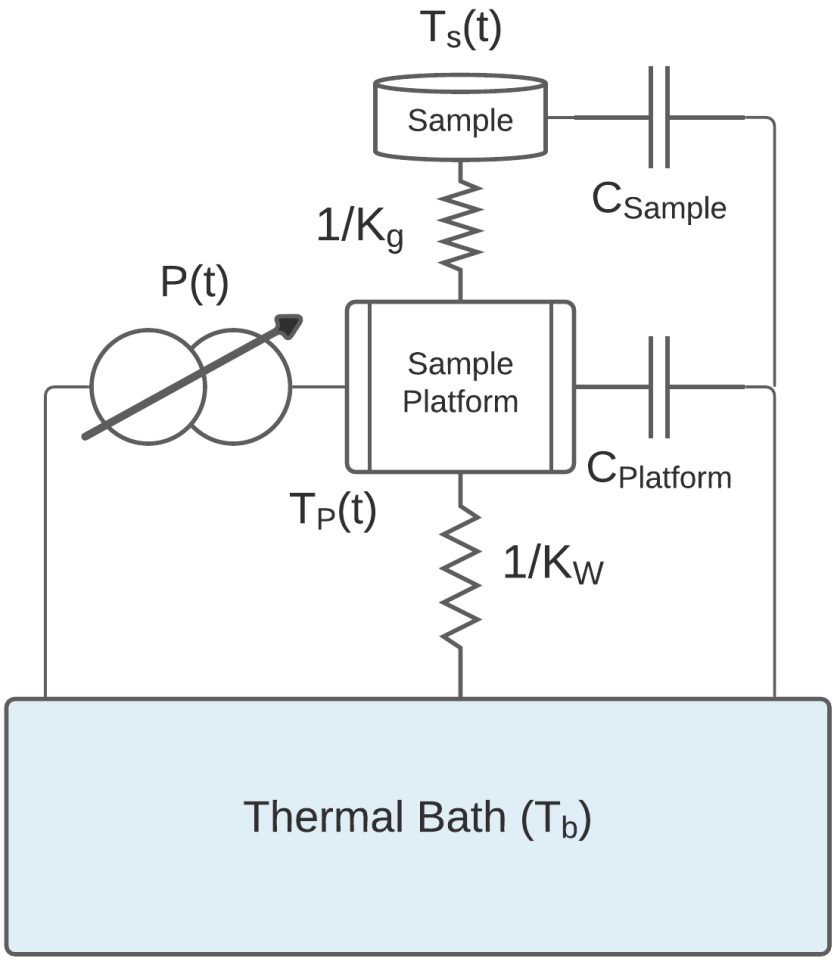

Figure 3.5: Circuit equivalent of the two-tau model for heat capacity. Adapted from Quantum Design user training material.

3.5. Equation 3.3 is then modified to give the following two equations,

$$C_{platform}\frac{dT_p}{dt} = P(t) - K_w(T_p(t) - T_b) + K_g(T_s(t) - T_p(t)) \tag{3.7a}$$

$$C_{sample}\frac{dT_s}{dt} = -K_g(T_s(t) - T_p(t)), \tag{3.7b}$$

where $C_{platform}$ is the heat capacity of the sample platform, C_{sample} is the heat capacity of the sample, and K_g is the thermal conductance between the two due to the grease. The respective temperatures of the platform and sample are given by $T_p(t)$ and $T_s(t)$.

Using the same power given in equation 3.4, the solution for the cooling curve ($t > t_0$) is represented by the expression,

$$T_p(t) - T_b = \left(\frac{P_0}{K_w}\right)\left[\left(\frac{\tau - \tau_2}{\tau_1 - \tau_2}\right)e^{-t/\tau_1} + \left(\frac{\tau_1 - \tau}{\tau_1 - \tau_2}\right)e^{-t/\tau_2}\right], \tag{3.8}$$

where the functional forms of τ_1, and τ_2 are given in equations 3.9a and 3.9b.[50]

$$\tau_1 = \left(\frac{\tau + \tau_s}{2}\right)\left(1 + \sqrt{1 - \frac{4\tau_s\tau_p}{(\tau + \tau_s)^2}}\right) \tag{3.9a}$$

$$\tau_2 = \left(\frac{\tau + \tau_s}{2}\right)\left(1 - \sqrt{1 - \frac{4\tau_s\tau_p}{(\tau + \tau_s)^2}}\right) \tag{3.9b}$$

where

$$\tau \equiv \frac{C_{sample} + C_{platform}}{K_w} \tag{3.10a}$$

$$\tau_s \equiv C_{sample}/K_g \tag{3.10b}$$

$$\tau_p \equiv C_{platform}/K_w. \tag{3.10c}$$

Note that $\tau_s\tau_p = \tau_1\tau_2$ and $\tau + \tau_s = \tau_1 + \tau_2$.

In this case, there are now 5 unknowns (instead of 3) that the computer needs to fit to the model, namely C_{sample}, $C_{platform}$, K_g, K_w, and finally T_b. However, if the heat capacity of the

platform $C_{platform}$ was measured by creating an addenda then there are only 4 unknowns. The PPMS software automatically applies the two-tau model if sample coupling, defined as $100\,\% \cdot (K_g/(K_g + K_w))$, falls below $100\,\%$.

There are certain cases where both the simple model and the two-tau model give erroneous results, specifically when C_{sample} is not constant during the measurement. For these cases, we must turn to slope analysis techniques.

3.2.3 Dual-Slope Technique

The thermal models and the data-fitting algorithm described in sections 3.2.1 and 3.2.2 assume that the heat capacity is approximately constant over the range of temperatures covered by a single measurement cycle. This assumption is not always true: for example, when materials being studied undergo first order phase transitions. In such transitions, the heating and cooling curves during relaxation must be treated separately. These cases are beyond the scope of this document, and interested readers are referred to the literature for more information.

Analyzing the heating and cooling relaxation curves individually can be useful for all samples. In this method, C_{total} is evaluated by directly comparing the heating and cooling rates of the sample temperature without need of measuring the thermal conductance between sample and bath. To use this technique, the heat capacity is measured continuously through a large temperature range. The slope of $T(t)$ is then calculated, making use of both the heating and the cooling curves. This eliminates the need to know the thermal conductance of the weak link. This so called Dual Slope (DS) method was proposed by Riegel and Weber [52].

More formally this is shown by,

$$C_{total}(T) = \frac{P(T) - K_w(T - T_b)}{S(T)}, \tag{3.11}$$

where $S(T) = dT/dt$ is the slope of the relaxation curve expressed as a function of temperature and $P(T)$ is the heater power as a function of temperature. Note that this expression is for analyzing the heating and cooling curves separately, which is important for samples undergoing first order

transitions. For samples that don't exhibit these features, we can combine the heating and cooling curves into the simple expression,

$$C_{total}(T) = \frac{P_h(T)}{S_h(T) - S_c(T)}. \tag{3.12}$$

The "h" and "c" subscripts in this equation refer to the heating and cooling curves, respectively. $P_c(T) = 0$ as in equation 3.4. Nowhere in this formula is the K_w term used, as it has been eliminated during the simultaneous equation solving. Figure 3.6 shows measurements made during a typical heating and cooling cycle.

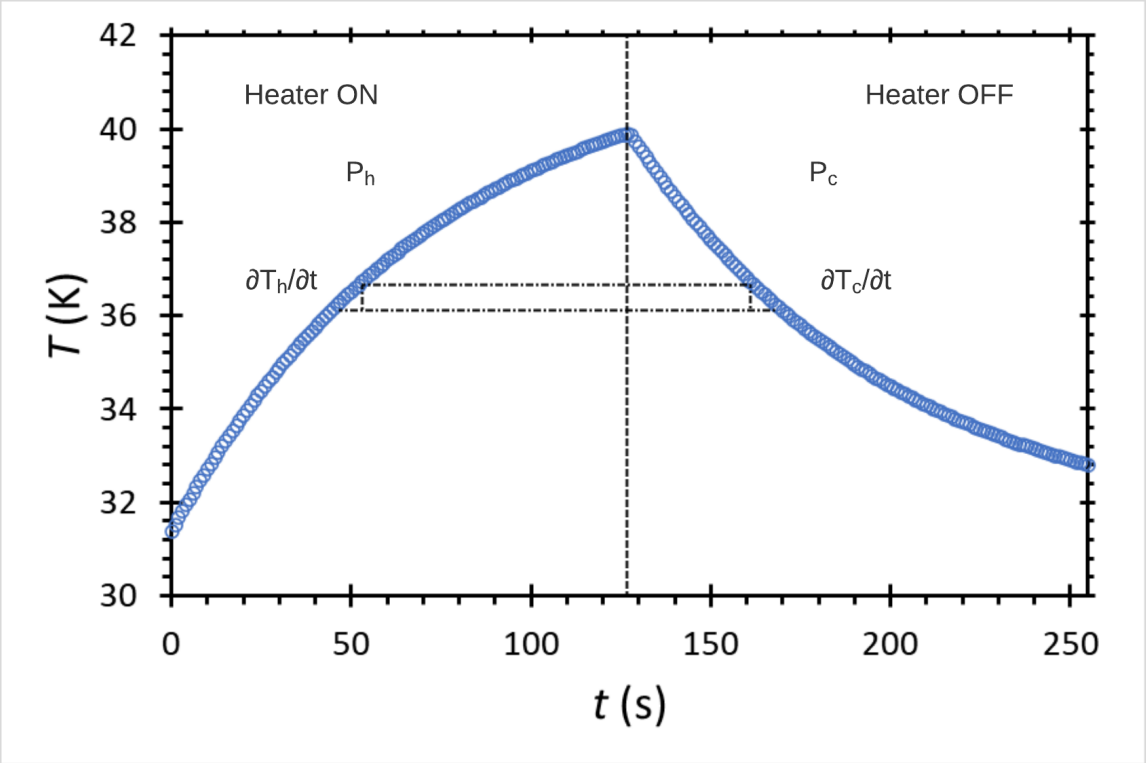

Figure 3.6: Typical example of a heat pulse in the dual slope method. Data is from a sample measured in this study. Adapted from Quantum Design user training material.

This has the benefit of removing uncertainties introduced by relatively poor knowledge of the bath temperature and the wire conductance. This technique does not explicitly depend on the heat loss through the wires; therefore, it is possible to obtain accurate heat capacity values from relaxation curves that span $30\,\%$ or more in temperature instead of the more typical 1–$2\,\%$. This allows much wider temperature spacing without compromising temperature coverage, leading to a reduction in total measurement time.

3.2.4 Heat Capacity Hardware

The PPMS heat capacity hardware consists of a calorimetry puck, digital signal processing (DSP) card, a sample mounting station, and high vacuum hardware. This section will cover the basic design of the calorimetry puck and DSP card. Quantum Design provides various options, particularly for use in ^{3}He systems as well as a vertical puck for highly magnetic samples, which are not covered here.

3.2.4.1 Calorimetry Puck

The PPMS calorimetry puck can be seen in figure 3.7. The puck itself is composed of the sample platform and accompanying chuck. The sample platform is a thin $3\,\mathrm{mm} \times 3\,\mathrm{mm}$ alumina square. On the platform is a thin-film heater and a bare Cernox™ [3] thermometer. Calibration of the Cernox thermometer is based on the ITS-90 temperature scale. The chuck, puck frame, and thermal radiation shield are assumed to be gold plated oxygen-free high conductivity (OFHC) copper. The "H grease" used for thermal connection between the chuck and the sample platform is a hydrocarbon based grease called Apiezon H and is currently made by M&I Materials Limited.

3.2.4.2 Heat Capacity DSP Card

The heat capacity DSP card extends the base functionality of the PPMS motherboard to allow heat capacity measurements. This card includes all the electronics needed to control the heaters and thermometers simultaneously. Along with the puck hardware covered above, the DSP card is

[3] Cryogenic thermometer made by sputtering a zirconium oxynitride thin film. Trademarked and commercially available from Lake Shore Cryotronics, Inc.

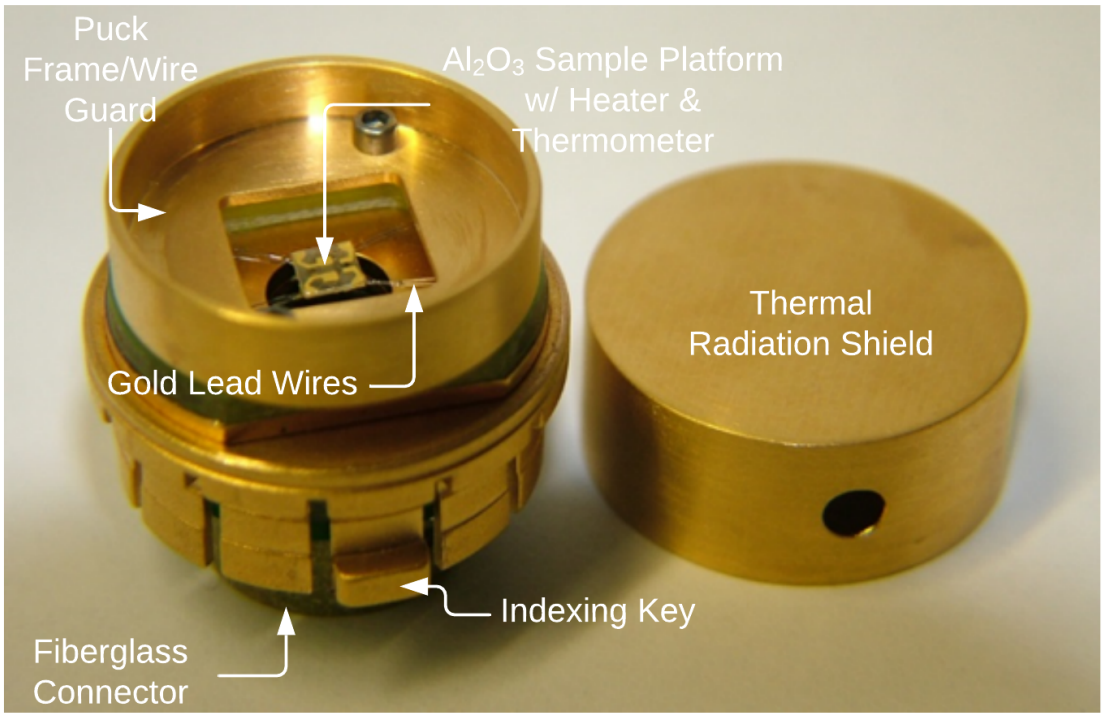

Figure 3.7: Calorimeter Puck for the PPMS. Adapted from Quantum Design user training material.

the heart of the heat capacity option. The card contains a digital signal processor used to control a number of converters and gain amplifiers. Precise digital signal processing is required for measuring the heater power and sample temperature versus time. To accomplish this, the DSP card supplies heater power through a precision current source and a digital-to-analog converter (DAC). The heater power used is then monitored by a separate analog-to-digital converter (ADC) and a programmable gain stage. Another precision current source provides AC current for reading the platform thermometer along with another ADC which measures the voltage across the thermometer. The resistance of the thermometer is measured by driving a constant square-wave alternating current at $244\,\mathrm{Hz}$ in the thermometer. Resistance is then calculated on the card in approximately $4\,\mathrm{ms}$ intervals by finding the difference between the positive and negative parts of the $244\,\mathrm{Hz}$ cycle as a current reversal technique. The DSP card also includes on-board resistors with minimal temperature sensitivity for calibration. All of this is done in order to reduce error in the thermometer measurement. The four-wire technique is used to reduce any contributions from the lead wires. The square-wave alternating current is used to cancel any thermoelectric electromotive forces (EMFs) by current reversal. Here the measurement voltage V_M is given by a combination of measurements with positive and negative polarity currents.

$$V_{M+} = V_{EMF} + I_S R_{Therm} \tag{3.13a}$$

$$V_{M-} = V_{EMF} - I_S R_{Therm} \tag{3.13b}$$

$$V_M = \frac{V_{M+} - V_{M-}}{2} = |I_S| R_{Therm}, \tag{3.13c}$$

where I_S is the current source and R_{Therm} is the thermometer resistance. Quantum Design also utilizes twisted wire pairs in order to reduce errors induced by magnetic fields.

3.3 Thermal Conductivity

This section will give a brief background of thermal conductivity measurements, introduce the theoretical models used in measuring thermal conductivity, cover the thermal transport option

hardware, and describe methods of sample preparation for thermal conductivity measurements in the PPMS.

The concept of heat flow can be argued to extend back to when man first discovered fire. As such, the history of thermal conductivity is too immense to be covered in full here. Those interested in the subject are encouraged to read the works of Burr [53], and Narasimhan [54, 55]. This short history is a much-condensed version of the full history covered in those works.

Heat and heat flow have been known since before written documentation existed. Many great scientists have contributed to the topic, and it cannot be fully explored in this work. However, in terms of measurements and their techniques, it is convenient to start with the invention of the mercury thermometer by Fahrenheit in the early 1700s. This is the accepted time period for repeatable thermometry measurements, and the adoption of a standard temperature scale.

As briefly discussed in section 3.2, the work of Black, Lavoisier, and Laplace on latent and specific heat in the middle 18th century paved the way for other quantitative thermodynamic measurements. Lambert made a large contribution posthumously in 1779 with publication of work introducing heat conservation, showing that the temperature profile of a heated object dropped off logarithmically instead of linearly, and proving the importance of geometry in heat flow. Around the same time, Benjamin Franklin conceived heat flow experiments that he prepared and gave to Ingen-Houz, who showed that the rate of heat conduction differed depending on the material. Comparable to the work of Lavoisier and Laplace with the invention of a calorimeter, Count Rumford (born Benjamin Thompson) is credited for inventing a heat flow measurement apparatus as well as performing a number of measurements. The above mentioned works were all groundbreaking, and helped to uncover some of the mystery of heat, which later allowed for more precise definitions of heat in the 19th century as well as lay the groundwork for measurement techniques we use today.

Our basis of understanding today came from the work of Fourier in the 19th century. Fourier's mathematical analysis is still the basis of steady state heat flow methods we use today. While others before him had uncovered parts of the picture, Fourier was unique in that he understood the connection to specific heat. Fourier was also revolutionary in breaking away from accepted

scientific thought at the time. Fourier is well-known for his theoretical physics contributions, but in the time of formulation some of his ideas were so revolutionary that he required experimental proof. Fourier then devised experimental techniques and carried out the first measurements of thermal conductivity as we now know it.

Many other great physicists contributed to thermodynamics, such as Joule, Boltzmann, etc. Further developments in thermal sciences are covered better elsewhere. Numerous measurement devices have been developed, many in the 1950s and 1960s. Readers are encouraged to delve into the papers and books of that time period, including authors such as G. White, R. Berman, G. Slack, as well as many others.

3.3.1 Steady-State Method

Only the absolute axial steady-state method will be covered here. Other steady-state techniques, such as the comparative or radial methods, were not used in this work, and can readily be found in the literature.

The simplest experimental arrangement is that shown in figure 3.8. This is known as the longitudinal, or axial, heat-flow method. A known heat flux $\dot{Q}$ is supplied by a heater to a sample of uniform cross-sectional area A and length L. Ideally the same heat is removed at the other end. We then have Fourier's heat equation,

$$\dot{Q} = \kappa \frac{A}{L} \Delta T, \tag{3.14}$$

where ΔT is the change in temperature measured across length L, and κ is the thermal conductivity. The ratio A/L is often absorbed into one of the other factors or expressed as a constant called the geometrical form factor.

The heat flux $\dot{Q}$ is supplied by a small heater which in modern equipment usually consists of a resistive circuit element. Since $\dot{Q}$ has the same units as electronic power $P = IV$, the heat input can be measured by monitoring the current and voltage drop across this resistive element. Temperature is then measured at two points along the sample at a fixed distance. The PPMS uses

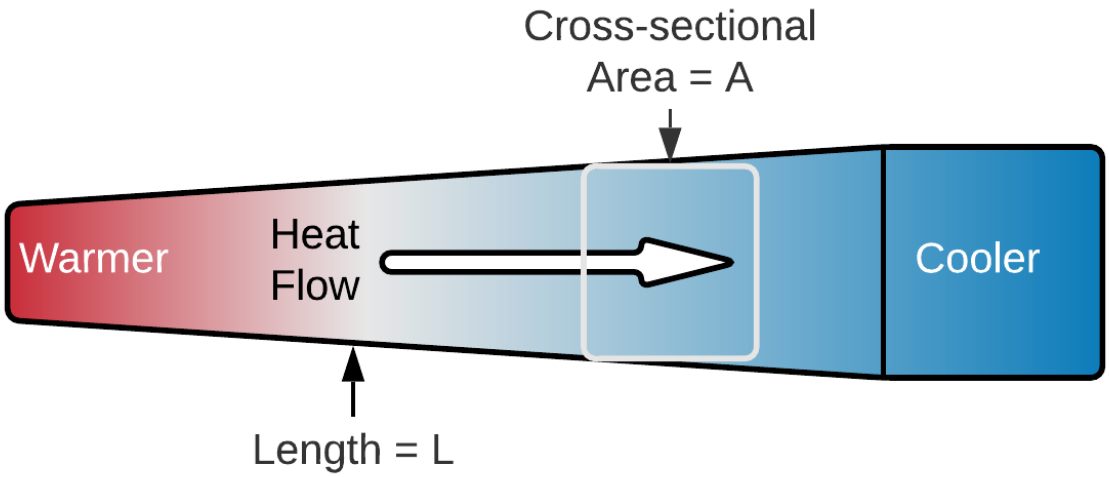

Figure 3.8: Simple Steady State Heat Flow

two Cernox temperature sensors. Knowing the sample geometry one can then solve directly for the thermal conduction,

$$\kappa = \frac{L}{A}\frac{\dot{Q}}{\Delta T}. \tag{3.15}$$

Thus, in this arrangement, all quantities are directly measured.

This technique assumes that the sample is isotropic, homogenous, and that heat losses due to radiation, heat conduction through gas or the connection leads, and convection currents are small. With real samples, the assumptions of isotropy and homogeneity are suspect. However, with proper care the heat losses can be controlled and minimized. The main disadvantage of this technique is that achieving steady-state conditions can take enormous amounts of time. Thus, while the PPMS can operate using this simple method, QD has employed the Pulse Power Method, also known as the Maldonado technique, for normal operation. This method is discussed in the next section.

3.3.2 Pulse Power Method

Steady-state methods are simple, yet powerful, and as with any experimental method, suffer from drawbacks. The main drawback of steady-state techniques is the long measurement time required for steady-state conditions to be realized. The Pulse Power Method is an alternate technique that allows for shorter measurement periods and is the default operation mode in the QD PPMS.

This method is attributed to Maldonado, who used it to measure both thermal conductivity and thermoelectric power in 1992 [56]. The experimental setup is similar to that of the steady-state measurement. The difference is that the bath temperature is slowly drifted and the heater current is pulsed with a square wave. See figure 3.9. No steady-state conditions are ever established or measured, allowing for measurement time to be substantially reduced.

As with heat capacity measurements, the thermal conductivity can be expressed in terms of an equivalent circuit as in figure 3.10. The PPMS uses a slightly different model than the original Maldonado technique. Mathematically, the model is given by the following equations,

$$C_{heater}\frac{dT_{heater}(t)}{dt} = P(t) - K_{leads}(T_{heater}(t) - T_{hot}(t)) \tag{3.16a}$$

$$C_{sample}\frac{dT_{hot}(t)}{dt} = K_{leads}(T_{heater}(t) - T_{hot}(t)) - K_{sample}(T_{hot}(t) - T_{cold}(t)) \tag{3.16b}$$

$$K_{sample}(T_{hot}(t) - T_{cold}(t)) = K_{leads}(T_{cold}(t) - T_b), \tag{3.16c}$$

where C represents the heat capacity, T is the time dependent temperature, P is the power input to the heater, and K is the thermal conductivity. Subscripts denote the heater, sample, leads, and hot and cold thermometers.

As with the heat capacity, QD uses a two-tau model for solving these differential equations. The solution can be derived by a Laplace transform of these differential equations and is rather involved, and will not be covered here. The change in temperature of the sample while heating is

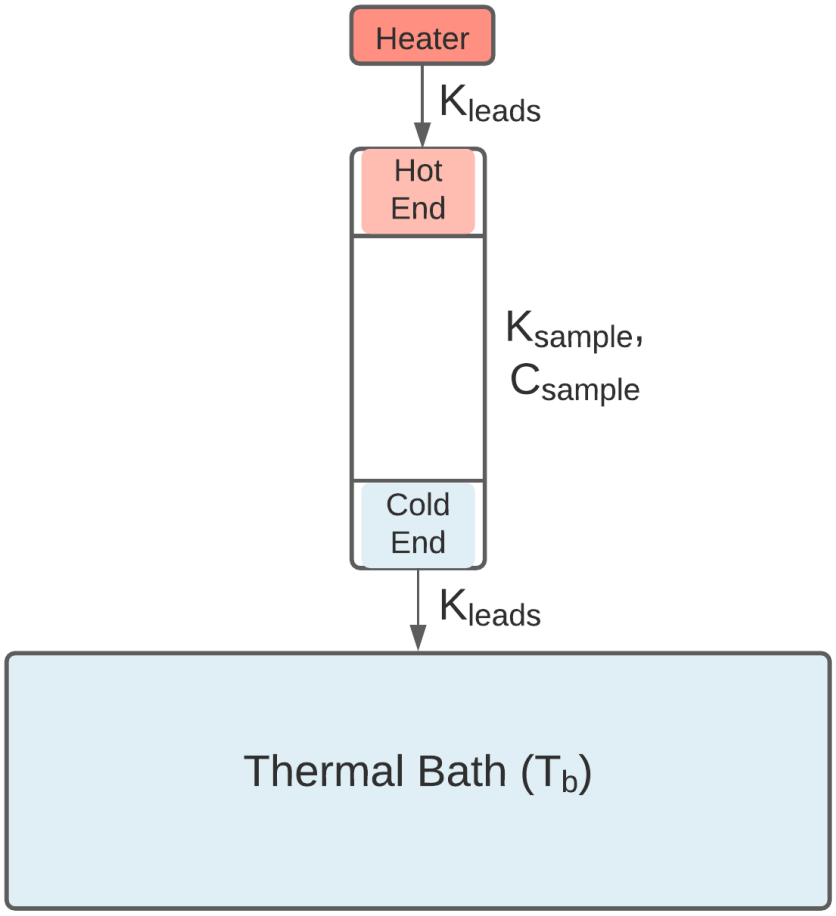

Figure 3.9: Schematic of the experimental apparatus used to measure thermal conductivity in the PPMS. Adapted from Quantum Design user training material.

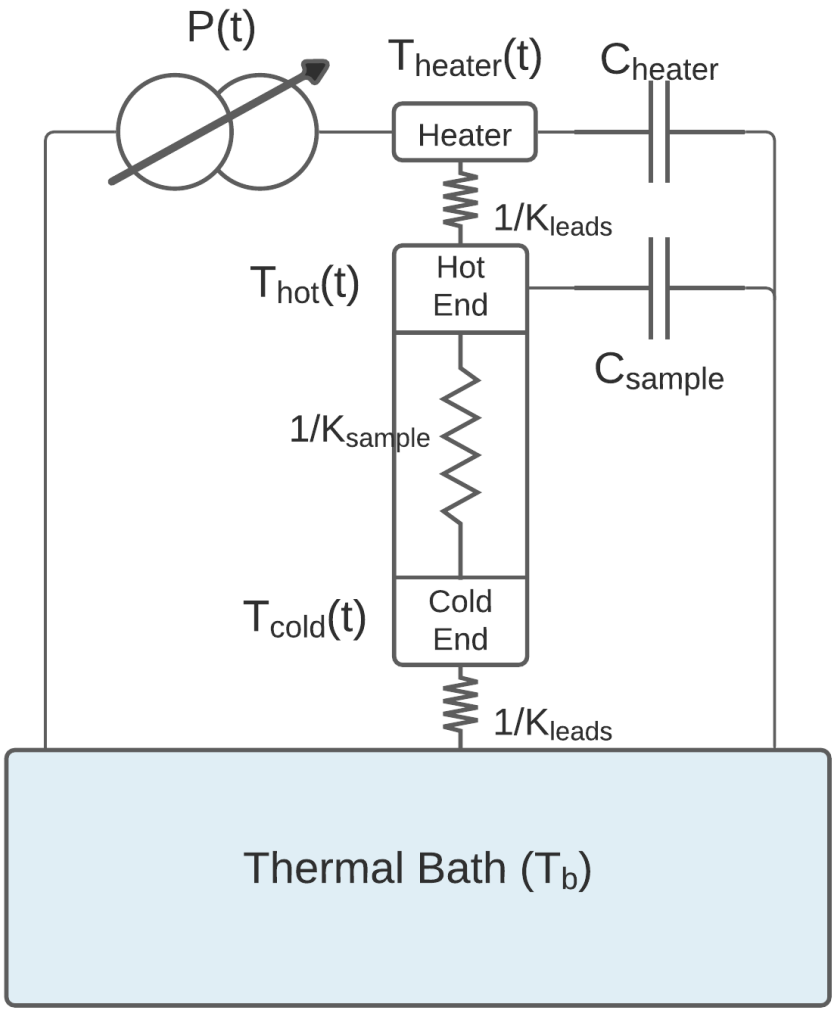

Figure 3.10: Circuit equivalent of the thermal transport. Adapted from Quantum Design user training material.

then given by,

$$\Delta T(\Delta T_\infty, \tau_1, \tau_2; t) = \Delta T_\infty \times [M(t - t_0) + P_{-1}M(t - t_{-1}) + P_{-2}M(t - t_{-2})] \tag{3.17a}$$

$$M(\tau_1, \tau_2; t) = 1 - \frac{\tau_1 e^{-t/\tau_1} - \tau_2 e^{-t/\tau_2}}{\tau_1 - \tau_2} \qquad (Heating) \tag{3.17b}$$

where ΔT_∞ represents the asymptotic temperature drop across the sample if the heater is left on indefinitely, τ_1 and τ_2 are the long and short empirical time constants, respectively, of the sample and P_n are the ratios of previous heater powers on previous pulses to the current pulse. See figure 3.11 for an example of a heat pulse along with the temperature response at the hot and cold thermometers in an idealized sample.

The cooling curve is modeled by changing the sign of the model equation, $\Delta T_{cooling} = A - \Delta T_{heating}$, where A is a constant. The PPMS uses a non-linear least-squares fitting to fit the data taken to these mathematical models and then reports the calculated thermal conductivity.

3.3.3 Thermal Conductivity Hardware

The PPMS Thermal Conductivity Option (TTO) hardware consists of a TTO puck (and its subcomponents/accessories), the AC Transport (ACT) Option hardware (including digital signal processing), a sample mounting station, and high vacuum hardware. This section will cover the basic design of the TTO puck and brielfy discuss the ACT hardware. For more detail see the Quantum Design hardware manuals [57, 58, 59, 60].

3.3.3.1 Thermal Transport Puck

The TTO sample puck can be seen in figure 3.12. The puck consists of a 12 pin plastic socket interface, key indexed chuck, base, printed circuit board (PCB), thermometer/heater shoe assemblies, and isothermal radiation shield. There are three shoe assemblies, two temperature/voltage shoes and one heater/current shoe. Each gold-plated copper "shoe" has a hole in which the appropriate sample lead is inserted and held in the shoe by a small stainless steel metric M1 screw. The temperature/voltage shoe assemblies contain a Cernox 1050 thermometer as well as a voltage

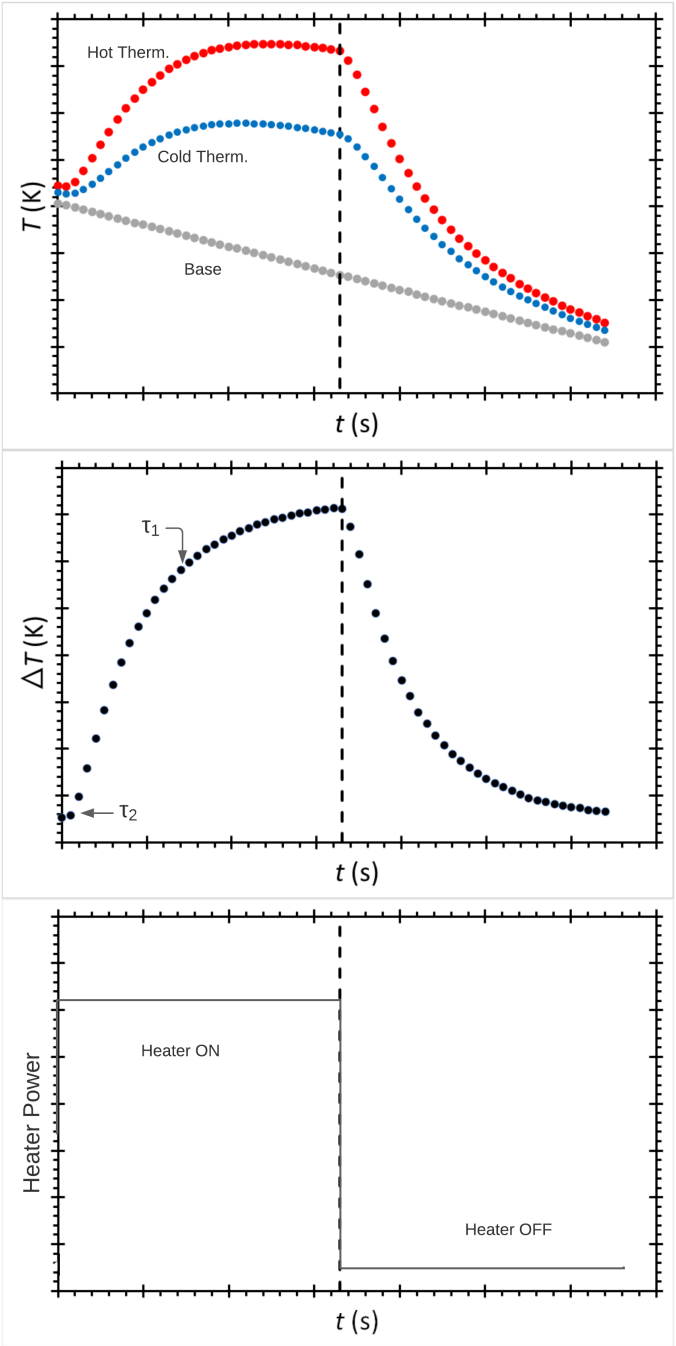

Figure 3.11: Heat pulse and temperature response at hot and cold thermometer shoes during thermal conductivity measurement.
Top Panel: Time trace of hot and cold thermometers during a heat pulse in this study; note that the PPMS base temperature is slewing. This data taken while cooling.
Middle Panel: Corresponding temperature ΔT differentials across the sample, indicating thermal time constants τ_1 and τ_2.
Bottom Panel: Heater power during square-wave heat pulse.
Adapted from Quantum Design user training material.

lead that is soldered to the shoe itself. The heater/current shoe assembly contains a resistive heater chip as well as an electrical current source lead (I+) that is soldered to the shoe. At the other end of each shoe assembly is a five-pin electrical plug on which the serial number is written. These plug into the PCB connected to the base. Each shoe type, heater or thermometer, is individually serialized. In order to minimize thermal conduction away from the sample, QD uses $2\,\mathrm{in}$ long, $3\,\mathrm{mil}$ diameter manganin wires for all connections except the (I+) current lead, which is made of PD-135 low-resistance copper alloy. The sample is connected to the puck at the coldfoot, which contains a Phillips screw and a stainless steel clamp on the bottom that clamps onto the sample lead. A copper isothermal radiation shield screws into the base of the puck in order to minimize radiation between the sample and the environment. A copper shield plate is also placed between the sample stage and the PCB sockets to minimize radiation effects.

3.3.3.2 ACT Controller Card

The TTO system uses hardware for the ACT option in order to generate the heat pulse and read back the sample thermal voltages in the thermal measurements, and to make the four-probe resistivity measurement on the sample. The driver board in the ACT Controller excites the sample by receiving and amplifying the signal from the AC boards digital signal processor. The sample signal is detected by a preamplification board, which sends the signal to the ACT DSP for processing. The ACT option provides as much as $200\,\mathrm{mA}$ of current when being controlled by the TTO system. More details are available in the Quantum Design hardware manuals [57, 58, 59, 60].

3.4 Laser Flash Analysis

Laser Flash Analysis results were performed by the Nelson group at Los Alamos National Laboratory. These results are compared with the measurements done on the Quantum Design system in the Naugle laboratory at Texas A&M University. An LFA 427 made by Netzch-Gmbh (Germany) was used for the measurement. This instrument uses a pulsed laser to irradiate the bottom of a pellet sample mounted in a carrier system and inside a furnace. The furnace is heated to a desired temperature before measurement. A thermocouple measures the sample temperature

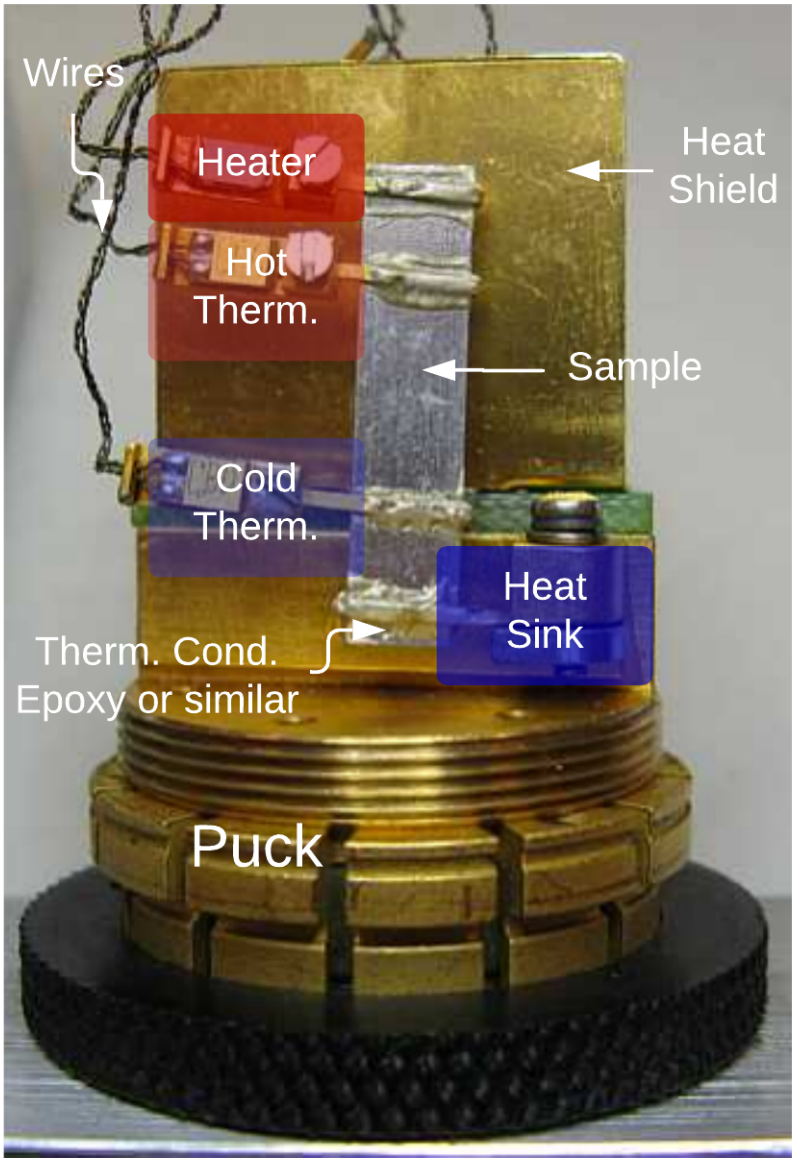

Figure 3.12: Thermal Transport Option Puck. Adapted from Quantum Design user training material.

and an infrared (IR) detector are used to simultaneously determine the heat capacity and thermal diffusivity. The method used is based upon the original work by Parker et al.[61].

4. SAMPLE PREPARATION[1]

4.1 Sample Fabrication

The experimental investigations in this study were performed on rod-like cylinders prepared via conventional powder metallurgical methods. These samples were prepared by the Nelson group at Los Alamos National Laborities. CeO_2 monoliths were prepared using a modified procedure to that reported by Nelson *et al.* [21]. CeO_2 powder (Alfa Aesar 99.99% purity rare-earth oxide (REO) basis, Lot C09Y013) was mixed with a binding agent, 0.45% ethylene bis(stearamide) (Sigma Aldrich Lot 1204CD). The binder and powder were homogenized using a high energy ball mill for 30 minutes in a zirconia jar and with zirconia ball. The resulting powder was sieved through a -200 mesh sieve to produce a fine power for pressing. The powder was pressed into cylindrical geometries (pellets) with a 4.17 mm diameter and approximately 6.5 mm tall. The pellets were sintered on a bed of CeO_2 powder at 1873 K for 4 hours in an Al_2O_3 crucible. A 1473 K isothermal soak, following the sintering step, was employed to set the $CeO_{2.0}$ stoichiometry.

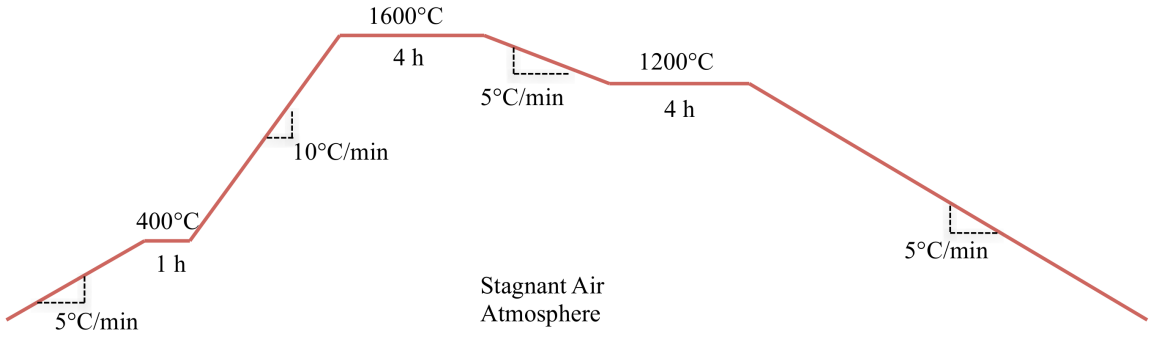

Figure 4.1: Thermal profile used to sinter CeO_2.

[1]Part of this chapter is reprinted with permission from "A Comprehensive Assessment of the Low-Temperature Thermal Properties and Thermodynamic Functions of CeO_2" by T. D. Morrison, E. S. Wood, P. F. Weck, E. Kim, S. O. Woo, A. T. Nelson, and D. G.Naugle 2019. The Journal of Chemical Physics, vol. 151, p. 044202, Copyright 2019, The Journal of Chemical Physics and AIP Publishing.[9]

Following the sintering profile, each pellet was weighed on a balance calibrated to 1 mg. The height and diameter were measured using calipers. These measurements were used to calculate a geometric density (7.21 g/cm^3) [62] and percent theoretical density, which was determined to be 97% $\pm$ 1%. Average grain size was measured to be 20.5 μm with a 1.9 μm standard deviation using the ASTM standard E112-12 Circular Intercept Procedure. A characteristic micrograph of this microstructure is displayed in Figure 4.2.

The stoichiometry of the CeO_2 is assumed to be minimally reduced (i.e. $CeO_{1.995}$). See Nelson *et al.* [21] for more details on the achievable stoichiometries of CeO_2 via powder metallurgical methods.

4.2 Heat Capacity Sample Preparation

Prior to heat capacity measurements a small flat disk of approximately $1\,\mathrm{mm}$ height was cut from the pellets using a wire diamond saw. Samples were weighed to within $0.1\,\mathrm{mg}$ with an analytical balance. Measurements were performed in a Quantum Design Physical Properties Measurement System (PPMS) from 2 to $400\,\mathrm{K}$. In all measurements, Apiezon N grease was placed on the sample platform to facilitate thermal conduction between the sample and platform. C_a, the combined addenda heat capacity of the platform, temperature sensor, heater, and including the contribution of the grease, was measured over the desired temperature range before the sample was loaded onto the platform. Addenda measurements were performed before each run. C_a was then subtracted from the total measured heat capacity to obtain the heat capacity of the sample. The standard relaxation technique was adopted for the entire temperature range. For finer spaced data the dual-slope method[52] was employed from 2 to $40\,\mathrm{K}$.

4.3 Thermal Conductivity Sample Preparation

For thermal conductivity measurements samples were prepared by first cutting the sample into a small brick of approximately $7\,\mathrm{mm} \times 1\,\mathrm{mm} \times 1\,\mathrm{mm}$ using a wire diamond saw. Samples were covered with Kapton tape exposing only the ends and small sections where the leads were to be attached. $50\,\mathrm{nm}$ of gold-palladium was then sputter coated onto the surface with an Anatech

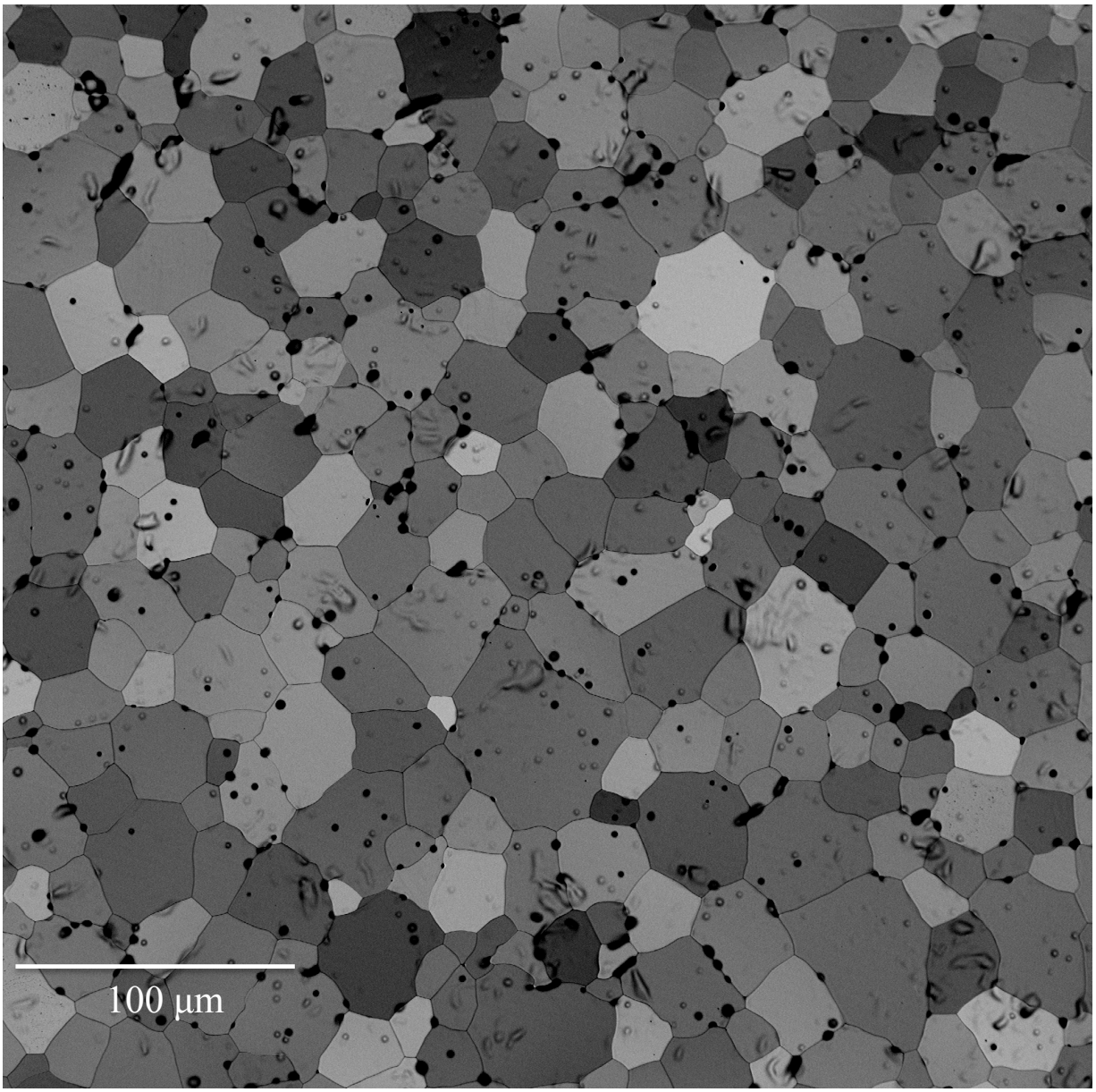

Figure 4.2: Micrograph of CeO_2 at $700\times$ magnification using a backscatter detector. Sample was cross-sectioned and thermally etched prior to imaging.

Hummer Sputtering System. Leads to the sample were made using high thermal conductivity epoxy (Epotek EK2000) and 5 mil ($0.127\,\mathrm{mm}$) diameter bare copper wire. The bare copper wire was wrapped around the sample on the sputtered gold-palladium surface to provide temperature measurement leads and twisted together to make a snug fit against the sample. The epoxy was then used to cement the copper wire leads to the sample. Finally the Kapton tape was removed and the epoxy cured. We used the cure schedule recommended by the manufacturer to attain the highest thermal conductivity. This cure schedule consisted of an initial cure at $125\,^{\circ}\mathrm{C}$ for $2\,\mathrm{h}$ followed by two step thermal post-cure of $150\,^{\circ}\mathrm{C}$ for $36\,\mathrm{min}$ and $200\,^{\circ}\mathrm{C}$ for $15\,\mathrm{min}$. The cure schedule was performed in a laboratory furnace using an argon atmosphere and according to the manufacturer, would result in a thermal conductivity of approximately $35.5\,\mathrm{W\,m^{-1}\,K^{-1}}$. The finished samples are represented by a typical example in Figure 4.3.

All samples were prepared in a 4 probe configuration to reduce contact resistance. Samples were measured multiple times by calipers to get an average of the cross sectional area and length between the two thermometer contacts. Since CeO_2 is an electrical insulator the 4 probe configuration is only reducing the thermal resistance and would normally be measured in a 2 probe configuration, however the high conductance of CeO_2 results in the sample thermal resistance and contact thermal resistance being of similar magnitude and as such, extreme care was taken to eliminate any effects of contact resistance. Thermal conductivity measurements were performed using the thermal transport option (TTO) of the Quantum Design PPMS. The TTO used a $2\,\mathrm{k\Omega}$ metal film resistor as a heat source and 2 Cernox® resistance thermometers made by Lake Shore Cryotronics. These thermometers offer excellent measurement stability over the entire available temperature range of the PPMS. [63] The samples were mounted by first attaching one of the outer copper wire leads to the cold foot heat sink of the TTO puck. The heater and both the "hot" and "cold" thermometers are attached to gold plated oxygen free high conductivity copper mounts. The other 3 copper wires of the 4 probe configuration were mounted to the thermometers and heaters by means of a screw. Thermal losses between the copper wire and the platforms is assumed to be negligible. Great care was taken to not have any physical contact between the thermometers and

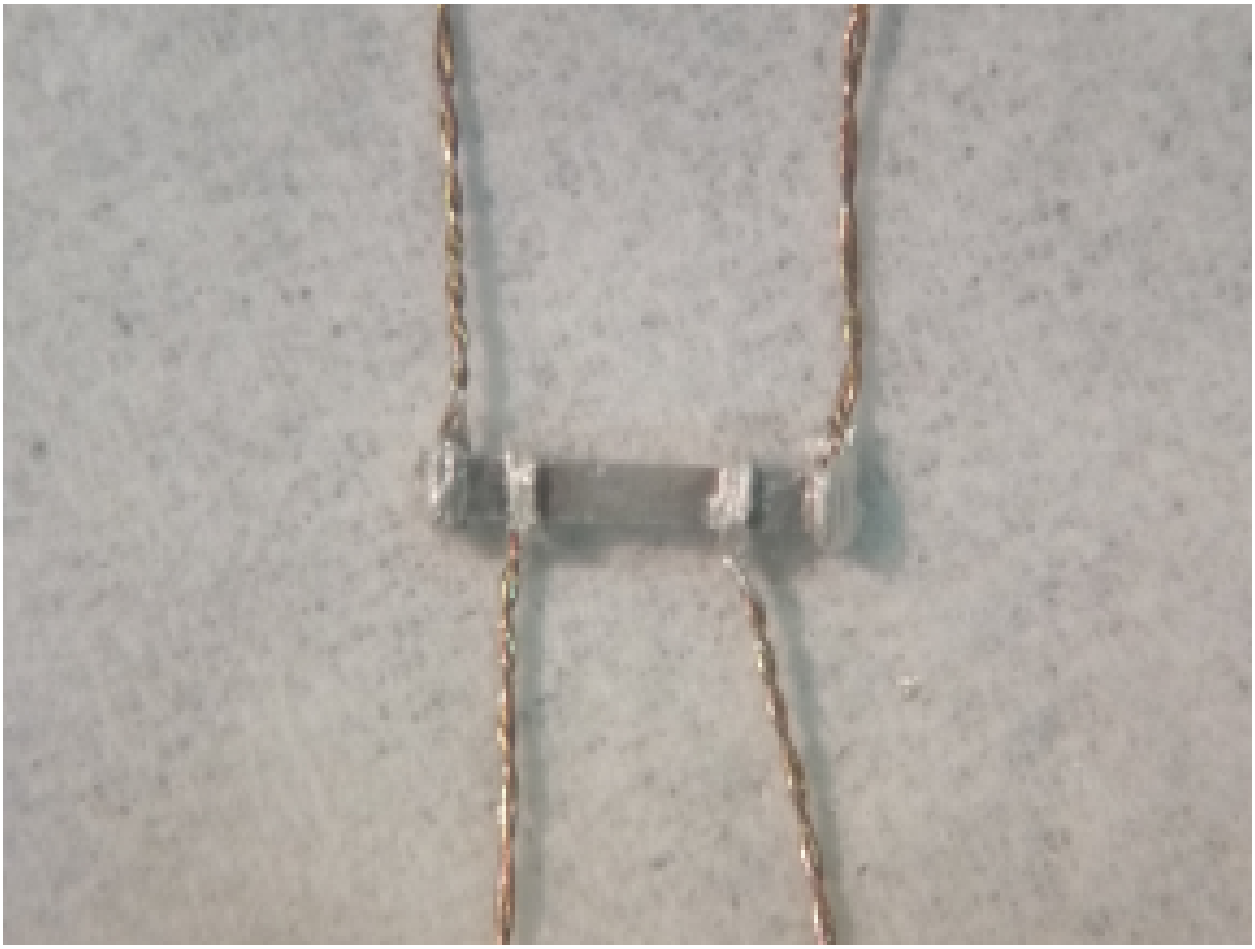

Figure 4.3: Microscope image of a typical CeO_2 sample after preparation with copper wire and high thermal conductivity epoxy.

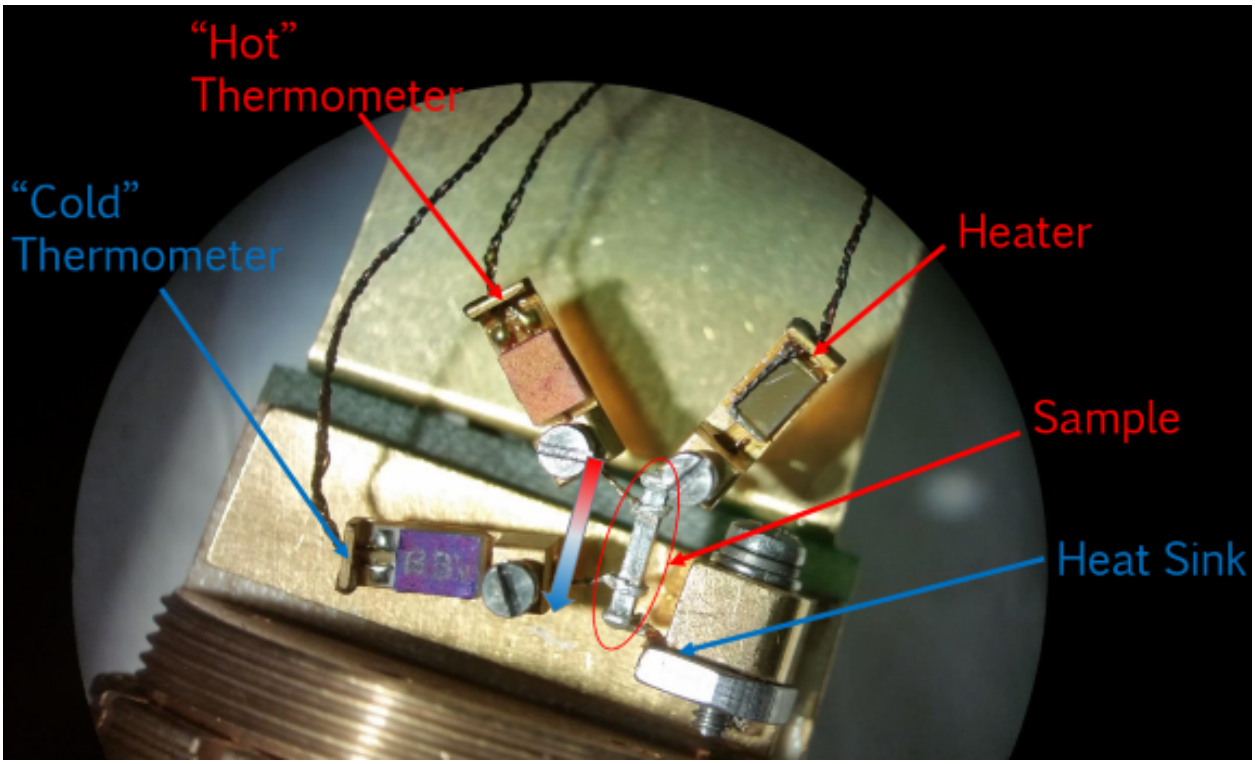

Figure 4.4: Microscope image of a typical CeO_2 sample after mounting on the Quantum Design thermal transport option measurement puck.

the TTO puck itself. An example image of one of the fully mounted CeO_2 samples is presented in Figure 4.4. As previously discussed in section 3.3.2 the PPMS was operated in continuous measurement mode, which utilizes the Maldanado[56] technique. Curves were taken from 2 to $400\,\mathrm{K}$ while both cooling and heating at a rate of $0.5\,\mathrm{K/\,min}$.

5. STOICHIOMETRIC CEO_2 RESULTS AND DISCUSSION[1]

In this chapter I will present the detailed experimental results of our stoichiometric, polycrystalline, sintered CeO_2 monolithic samples. This data will then be compared with other experimental literature, laser flash analysis experiments done at Los Alamos National Laboratory as well as density functional perturbation theory (DFPT) calculations performed by colleagues at Sandia National Laboratory/University of Nevada Las Vegas. By collecting high quality thermodynamic experimental data in the T ≤ 400 K range we are able to provide a unique look at how well modern computational calculations match with fundamental thermodynamic experiments. Although this range has been experimentally measured before, it will be shown that these results define a new standard for low temperature measurements of this material. With the exception of the Laser Flash Analysis measurements, all experimental work was performed by me at Texas A&M. The work presented in this chapter has been published by Morrison *et al.* "A Comprehensive Assessment of the Low-Temperature Thermal Properties and Thermodynamic Functions of CeO_2," The Journal of Chemical Physics (2019) [9]. Much of the same material will be presented here, with in depth expansion of the discussion where appropriate. Considerable work was done in doing numerical integration of the heat capacity data to extract the thermodynamic functions of this material. A more thorough discussion of this aspect, as well as the Klemens-Callaway model fitting will be included. Results of non-stoichiometric ceria will be reviewed in chapter 6.

5.1 Raman Spectroscopy

In order to verify that the samples studied were of high quality and also attempt to characterize the oxygen vacancies present, a series of Raman spectroscopy measurements were performed. Raman measurements were performed at room temperature using a Jobin Yvon Horiba LabRAM HR (Villeneuve d'Ascq, France) instrument coupled to an Olympus BX41 microscope with a 50Œ

[1]Part of this chapter is reprinted with permission from "A Comprehensive Assessment of the Low-Temperature Thermal Properties and Thermodynamic Functions of CeO_2" by T. D. Morrison, E. S. Wood, P. F. Weck, E. Kim, S. O. Woo, A. T. Nelson, and D. G.Naugle 2019. The Journal of Chemical Physics, vol. 151, p. 044202, Copyright 2019, The Journal of Chemical Physics and AIP Publishing.[9]

objective using a $514.5\,\mathrm{nm}$ laser excitation from an Ar-ion laser. An $1800\,\mathrm{lines/mm}$ grating spectrometer equipped with a Peltier-cooled charge-coupled device (CCD) detector (Andor) was used to acquire spectra yielding a spectral resolution better than $2\,\mathrm{cm}^{-1}$ and spatial resolution of about $1\,\mu\mathrm{m}$. The experimentally determined Raman spectrum of a typical CeO_2 sample in this study (see Figure 5.1) shows the distinct F_{2g} band at 465 cm^{-1}. Extraction of the Raman peak was carried out via custom code written in the python programming language and utilizing the python built in module Lmfit along with a combination of other python packages for data analysis including Pandas. To properly model the Raman peak I chose to use a custom model that is a combination of the LorenztianModel class and LinearModel class. The linear part of the model was to take out the background measurement, while the Lorenztian model was the actual peak fitting shape. The Lorenztian model is based on the Cauchy-Lorentz distribution function. This model has three Parameters: amplitude, center, and sigma. In addition, parameters for the full width at half maximum and maximum peak height are included as constraints.

$$f(x; A, \mu, \sigma) = \frac{A}{\pi}\left[\frac{\sigma}{(x-\mu)^2 + \sigma^2}\right] \tag{5.1}$$

where the parameter amplitude corresponds to A, center to μ, and sigma to σ. The full width at half maximum is then given by 2σ.

Results of this modeling gave a peak of 464.8 cm^{-1} agreeing completely (and within the estimated spectral resolution of 2 cm^{-1}) with "eye-ball" graphing results of a peak at 465 cm^{-1} . The full width at half maximum is measured to be 7 cm^{-1} using this Lorentzian fit. This band is consistent with single crystal CeO_2 at 465 cm^{-1} [64, 65, 66]. As detailed in previous polycrystalline sample measurements [67, 68] large grain size samples show a Raman spectra consistent with single crystal samples. DFPT calculations performed by Sandia/UNLV as part of the published study predict a value of 458 cm^{-1}. This is in good agreement with the experimentally obtained value. The lack of any other peaks in the 400-600 cm^{-1} range indicate that the samples are highly stoichiometric with no detectable oxygen vacancies. See Schilling *et al.* [68] for a thorough discussion of the effect of oxygen vacancies on the F_{2g} band. Further Raman measurements of

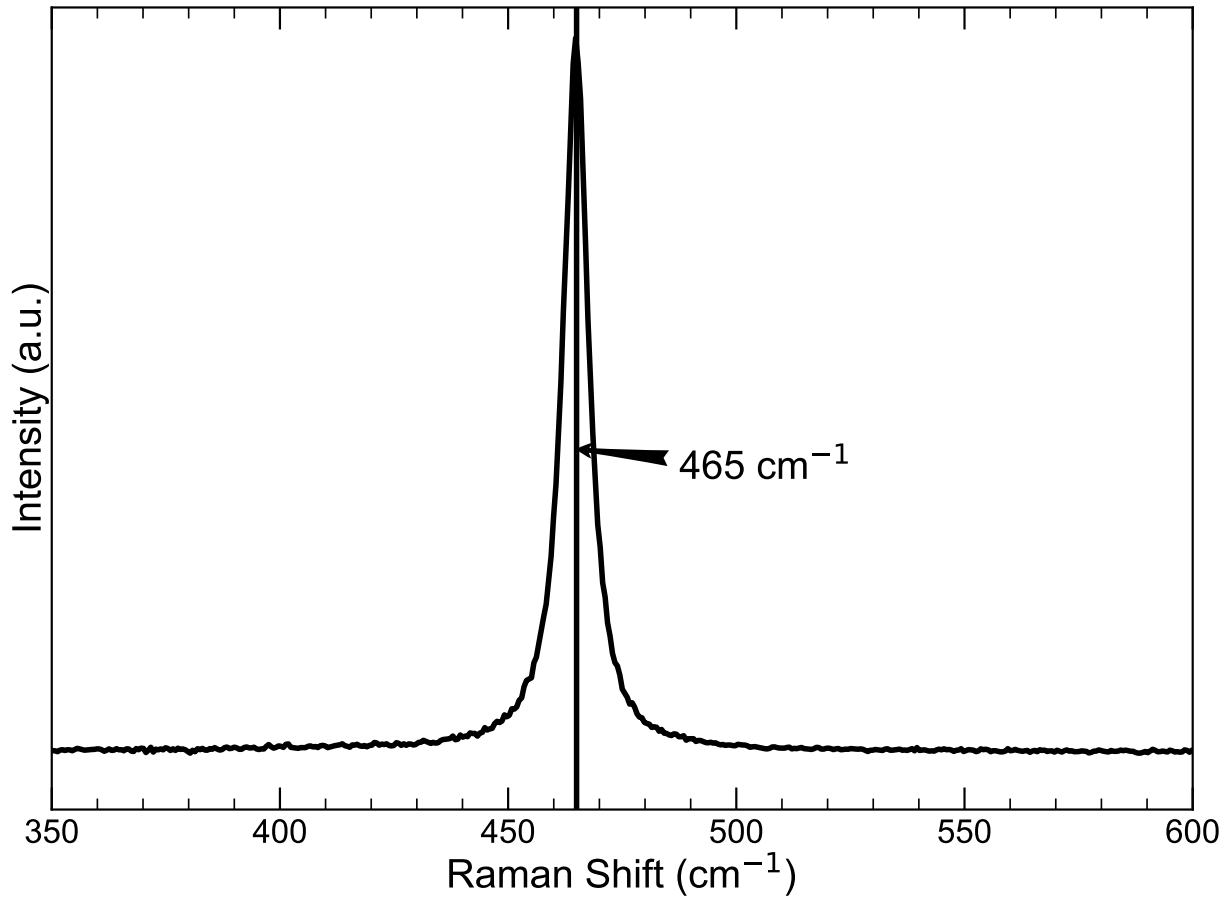

Figure 5.1: Typical Raman Shift of CeO_2 Samples in this study. The vertical line at 465 cm$^{-}1$ represents the F_{2g} peak and is typical of high quality samples.

nonstoichiometric $CeO_2 - \delta$ samples will be presented with their heat capacity data in chapter 6.

5.2 Molar Heat Capacity

Figure 5.2 displays the isobaric molar heat capacity at standard pressure ($P = 1$ bar) determined by my experiments at Texas A&M. Figure 5.3 depicts the calculated entropy from the low-temperature calorimetric measurements of the present study and those of Westrum and Beale [1], along with DFPT calculated values for bulk CeO_2. Figure 5.2 also shows calorimetric data from Kuznetsov *et al.*[2], Krishnan and Nagarajan[3], Gallagher and Dworzak[4], Riess *et al.*[5], and King and Christensen[6].

Measured results are in excellent agreement with those of Westrum and Beale throughout most of the temperature range, with an important correction at T<15K. Estimated error bars are $\pm 5\%$ or smaller as detailed in Lashley *et al.* [39]. Data presented here is an average of 3 different samples. Each data point was also taken 3 times for each sample and averaged together (2 times for dual slope data).

As shown on the inset C/T vs T^2 plot in Figure 5.2, below 15 K (where $T^2 < 200$) there is a significant deviation in the data from the previously published values. The deviation in the current and previously reported data can, in part, be due to improvement in measurement techniques over the last 60 years. Modern instruments such as the PPMS feature high volume automatic data collection and analysis, as well as real time slope fitting and precise temperature control. Westrum and Beale had two operators of their cryostat system and took their data by hand while simultaneously compensating temperature drifts. Their work is extremely impressive and should remain a recognized gold standard. However, the difference is hypothesized here to be due to impurities in Westrum and Beale's original samples. This argument is supported by the excellent work of Gruber *et al.* [69] concerning impurities in Ce_2O_3 samples measured by Westrum and Beale. The deviation of Westrum and Beale's CeO_2 data from that reported here at low temperatures shows characteristics similar to that of a Schottky anomaly, which could be due to sample impurities. This is supported by measurement of C_p in nonstoichiometric samples ($CeO_{2-\delta},\ \delta = 0 - 0.032$) that will be presented in the chapter 6.

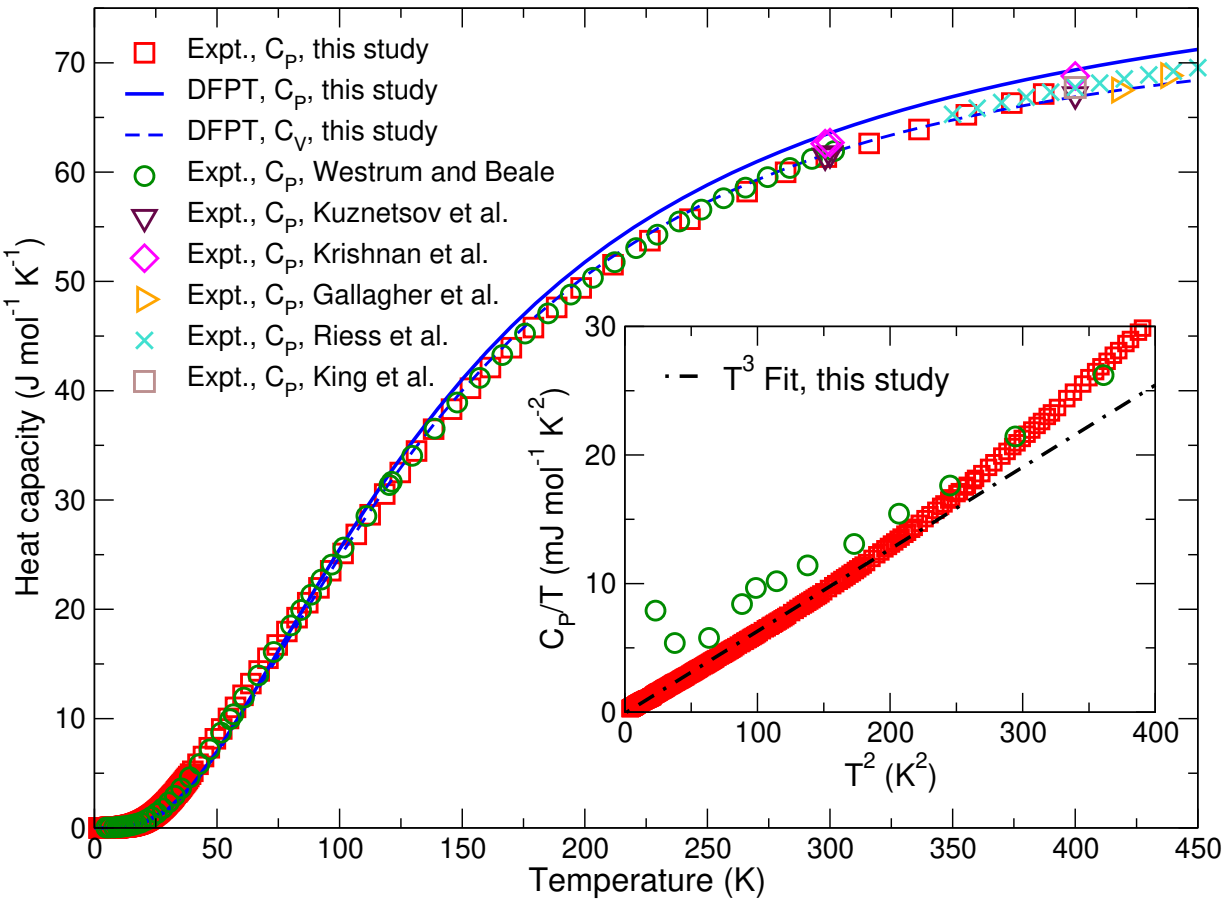

Figure 5.2: Measured standard-pressure isobaric molar heat capacity (C_{P}) of CeO_2 and DFPT/PBEsol calculated C_{P} and isochoric molar heat capacity (C_{V}). Calorimetric data from previous studies are also displayed: Westrum and Beale[1], Kuznetsov *et al.*[2], Krishnan and Nagarajan[3], Gallagher and Dworzak[4], Riess *et al.*[5], King and Christensen[6]. Inset shows experimental data as C/T vs. T^2 and a fit of the data to the low-temperature T^3 limit of the simple Debye model.

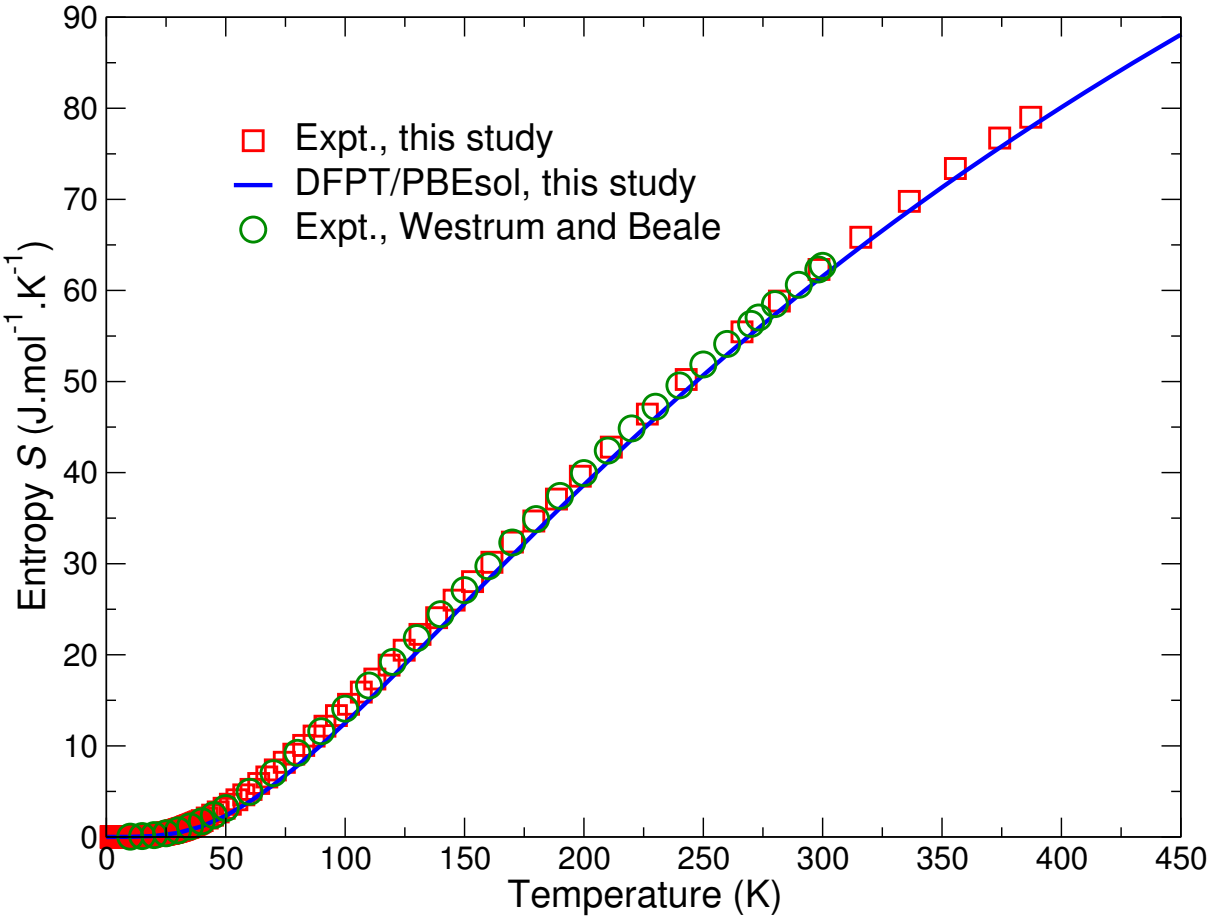

Figure 5.3: Calorimetric data and DFPT/PBEsol results for the entropy of CeO_2. Calorimetric data from Westrum and Beale[1] are also represented.

All measurements showed the expected sigmoid behavior typical of crystalline salts. At low temperatures the well known Debye model provides a simple yet successful one parameter model to describe the heat capacity [34]. For the phonon contribution, the low temperature limit of the heat capacity reduces to

$$C = \frac{12}{5}\pi^4 N_A k_B (\frac{T}{\Theta_D})^3 \tag{5.2}$$

where N_A is Avogadro's number, Θ_D is the Debye temperature, k_B and T are the same as defined above, and $C = C_v \approx C_p$. Thus, at sufficiently low T, C varies vary as T^3 and a plot of C/T against T^2 will be a straight line. It must be stressed that equation (5.2) is valid only for temperatures of the order of $T < \Theta_D/50$.

As can be seen in the inset of Figure 5.2 there is no indication of magnetic or electronic contributions to the heat capacity of stoichiometric CeO_2. To extract Θ_D a linear least squares regression was performed on C/T vs. T^2 data. Since CeO_2 is not a monatomic solid, equation (5.2) must be multiplied by the number of atoms per molecule to properly fit the data. Using the simple Debye model Θ_D was calculated to be 455 K. This value lies in between previously reported data: Θ_D = 409 K[8], 480 K[70], and also within the range of recent theoretical calculations Θ_D= 481 K[28] and Θ_D= 414.5-582.9 K[25] depending on calculated parameters.

This experimental work was motivated in part to provide a unique test to the modern computational calculations available. Most of the interest in CeO_2 lies in the high temperature regime, where CeO_2 is used as a non-nuclear surrogate for UO_2 and PuO_2. Total-energy calculations were conducted using spin-polarized density functional theory (DFT), as implemented in the Vienna *Ab initio* Simulation Package (VASP) [71, 72]. The parameterization of Perdew, Burke, and Ernzerhof revised for solids [29] (PBEsol) was utilized, since it accurately reproduces the measured crystal parameters and properties of CeO_2 [73, 28]. Information about this is included here for context, but the work was not done by me and so will not receive attention in this thesis. For more information please refer to the published paper [9].

To compare to the experimental work, the isobaric molar heat capacity, C_{P}, was computed as the second derivative of the Gibbs free energy with respect to the temperature by colleagues at

Sandia/UNLV:

$$C_{\mathrm{P}}(T,P) = -T\frac{\partial^2 G(T,P)}{\partial T^2} = T\frac{\partial V(T,P)}{\partial T}\frac{\partial S(T,V)}{\partial V}\Big|_{V=V(T,P)} + C_{\mathrm{V}}[T, V(T,P)] \tag{5.3}$$

where $V(T,P)$ corresponds to the equilibrium volume at T and P. In Eq. (5.3), the isochoric molar heat capacity C_{V} is defined as,

$$C_{\mathrm{V}} = k_{\mathrm{B}} \sum (\beta\hbar\omega)^2 \frac{e^{\beta\hbar\omega}}{[e^{\beta\hbar\omega}-1]^2}, \tag{5.4}$$

and the entropy is computed using the expression:

$$S = -k_{\mathrm{B}} \sum \ln\left[1 - e^{-\beta\hbar\omega}\right] - \frac{1}{T}\sum \frac{\hbar\omega}{e^{\beta\hbar\omega}-1}. \tag{5.5}$$

The standard values calculated from DFPT at $T = 298.15$ K by the Sandia/UNLV group and published in [9] are $C_{\mathrm{P}}^0 = 63.4$ J mol^{-1} K^{-1} and $S_{\mathrm{P}}^0 = 61.1$ J mol^{-1} K^{-1}, and are in good agreement with calorimetric data. They show less than 2% deviation from the experimental values.

5.3 Thermodynamic Functions

In order to derive the enthalpy and entropy functions, the thermal evolution of the isobaric heat capacity calculated from DFPT/PBEsol for bulk CeO_2 was fitted using a nonlinear least-squares regression to a Haas-Fisher-type polynomial [74],

$$C_{\mathrm{P}} = a + bT + cT^{-2} + dT^{-0.5} + eT^2, \tag{5.6}$$

with the resulting optimized coefficients in the temperature range 100-450 K: $a = 2.04096 \cdot 10^2$, $b = -1.370 \cdot 10^{-1}$, $c = 2.44059095 \cdot 10^5$, $d = -1.901314 \cdot 10^3$, and $e = 8.5 \cdot 10^{-5}$. The sum of squared differences between calculated and fitted C_{P} data was $7 \cdot 10^{-3}$.

The enthalpy function, $(H_T - H_{298.15}) \cdot T^{-1}$, was calculated by analytical integration of the fit to the isobaric heat capacity using the formula:

$$(H_T - H_{298.15}) \cdot T^{-1} = \int_{298.15}^{T} C_{\mathrm{P}}(T)\mathrm{d}T, \tag{5.7}$$

The Gibbs energy function, $(G_T - H_{298.15}) \cdot T^{-1}$, was computed using the expression:

$$(G_T - H_{298.15}) \cdot T^{-1} = (H_T - H_{298.15}) \cdot T^{-1} - S, \tag{5.8}$$

where S is the entropy calculated from Eq. (5.5). Results for the experimental and computed enthalpy function and Gibbs energy function for bulk CeO_2 are shown in Figures 5.4 and 5.5, along with previous experimental data from Westrum and Beale [1], King and Christensen [6], and Yashvili *et al.* [7]

5.4 Thermal Conductivity

In Figure 5.6 presents the thermal conductivity of bulk CeO_2 pellets from 2-400 K using the Maldonado[56] technique. Also presented are the results of LFA (this work), along with previously published data by Khafizov *et al.* [8]. Low-temperature thermal conductivity data and LFA data in this study are in excellent agreement. Further, measured values are in good agreement with previously published data. The only low-temperature thermal conductivity data of bulk polycrystalline CeO_2 pellets in the literature to date was performed by Khafizov *et al.* [8]. However, the focus of that study was mainly thin films of CeO_2, not the bulk properties and used modulated thermoreflectance microscopy (MTRM) from 77-1000 K. The room temperature value of the thermal conductivity was found to be 16.7 W m^{-1} K^{-1}, also in good agreement with that determined for CeO_2 of similar purity. [75]

In order to determine the thermal conductivity using LFA, the thermal diffusivity was measured on three samples. All three samples provided data in good agreement across the temperature range investigated. The thermal diffusivity is observed to monotonically decrease with temperature, as

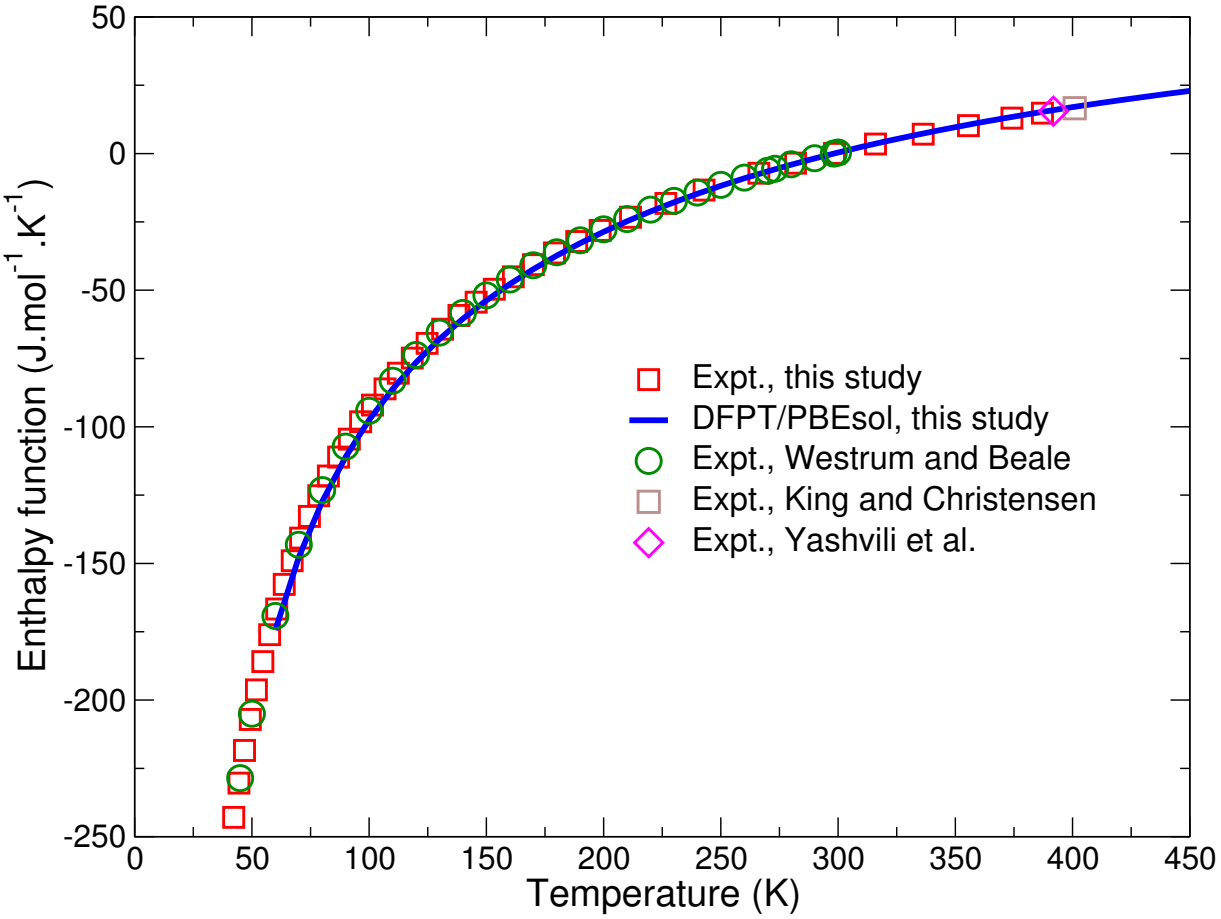

Figure 5.4: Experimental data and DFPT/PBEsol results for the enthalpy function of CeO_2. Calorimetric data from Westrum and Beale[1], King and Christensen[6], and Yashvili *et al.*[7] are also shown.

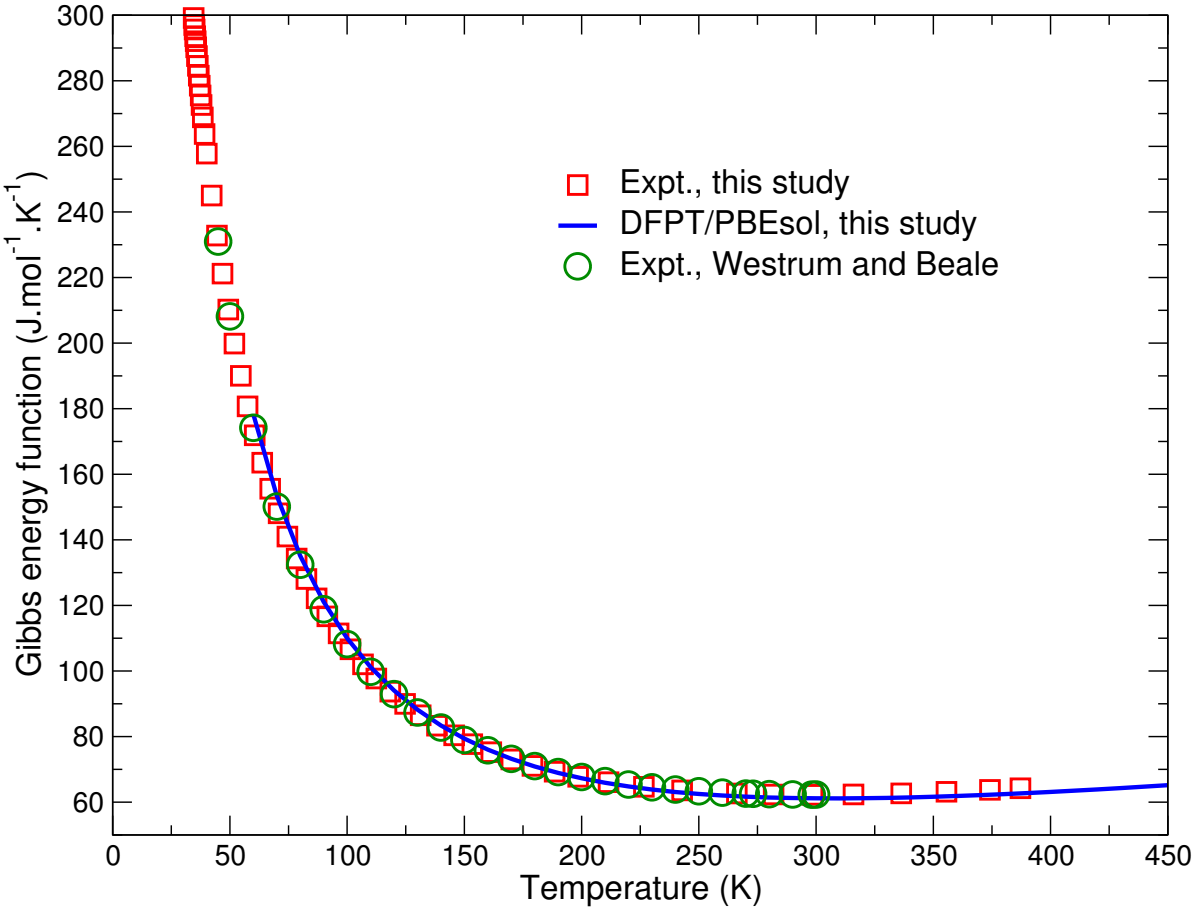

Figure 5.5: Experimental data and DFPT/PBEsol results for the Gibbs energy function of CeO_2. Calorimetric data from Westrum and Beale[1] are also displayed.

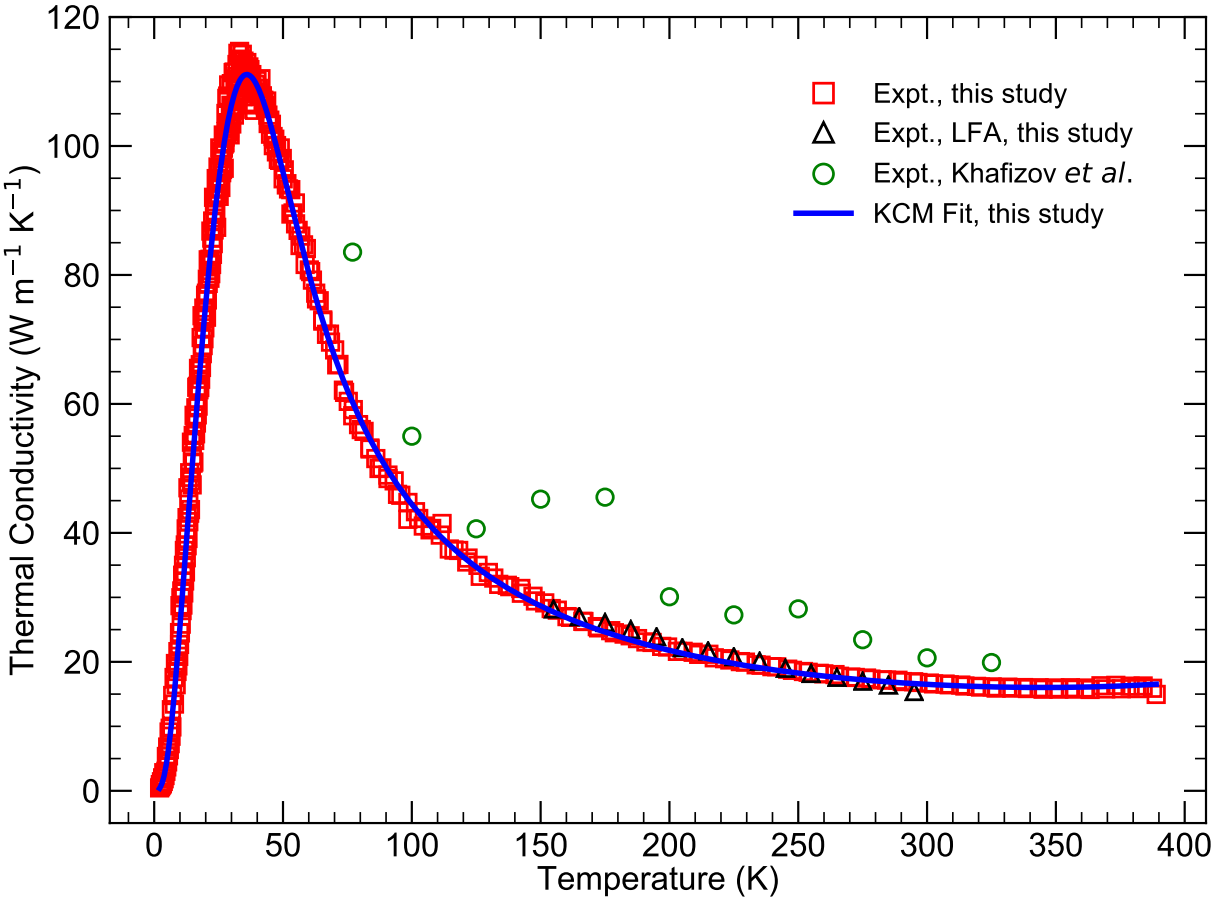

Figure 5.6: Experimental data and Klemens-Callaway fit for the Thermal Conductivity of CeO_2. LFA data from this study and MTRM data from Khafizov *et al.*[8] are also displayed. Error bars in this work are equal to or smaller than the symbol size, i.e. 5% for LFA measurements.

typical of an oxide ceramic in this temperature range. Thermal conductivity can then be calculated using the product of the thermal diffusivity, specific heat capacity, and density. The heat capacity of CeO_2 measured as described earlier in this work provides this data as a function of temperature over the temperature range where LFA was used to collect thermal diffusivity data. This data is converted from a molar heat capacity to a specific heat capacity by assuming a molar mass of CeO_2 as 172.12 g/mol. Density is assumed constant as 6.85 g/cm^3. This value corresponds to 95% theoretical density, within 1% of the value measured for all samples measured.

A simple model for thermal conductivity at low temperatures is the Klemens-Callaway model (KCM) [38]. To solve the Boltzmann transport equation, this model assumes a Debye phonon dispersion relation and utilizes a relaxation time approximation. The thermal conductivity as a function of temperature T is then given by

$$\kappa = \frac{k_B}{2\pi v}\left(\frac{k_B T}{\hbar}\right)^3 \int_0^{\Theta_D/T} \tau(x,T)\frac{x^4 e^x}{\left(e^x-1\right)^2}dx \tag{5.9}$$

where v is the mean velocity of sound in the solid, $\tau(x,T)$ is the phonon relaxation time, $x = \hbar\omega/k_B T$ is the reduced phonon frequency, and ω, k_B, $\hbar$, and Θ_D are as defined above. Higher order correction terms are neglected for simplicity. The Debye temperature was taken from the above experimental heat capacity measurements to be $\Theta_D = 455$ K. Then the mean velocity of sound is calculated to be 3610 m/s using the relation $v = k_B\Theta_D/\hbar\sqrt[3]{6\pi^2 N/V_0}$, where N is the number of atoms per unit cell, and $V_0 = a^3/4$ is the volume per unit cell, with a being the lattice constant of 5.411 Å. In general, the Debye temperature is not constant and at higher temperatures anharmonic, and other effects must be considered.[76, 77] A plot displaying the temperature dependence of Θ_D is pictured in Figure 5.7.

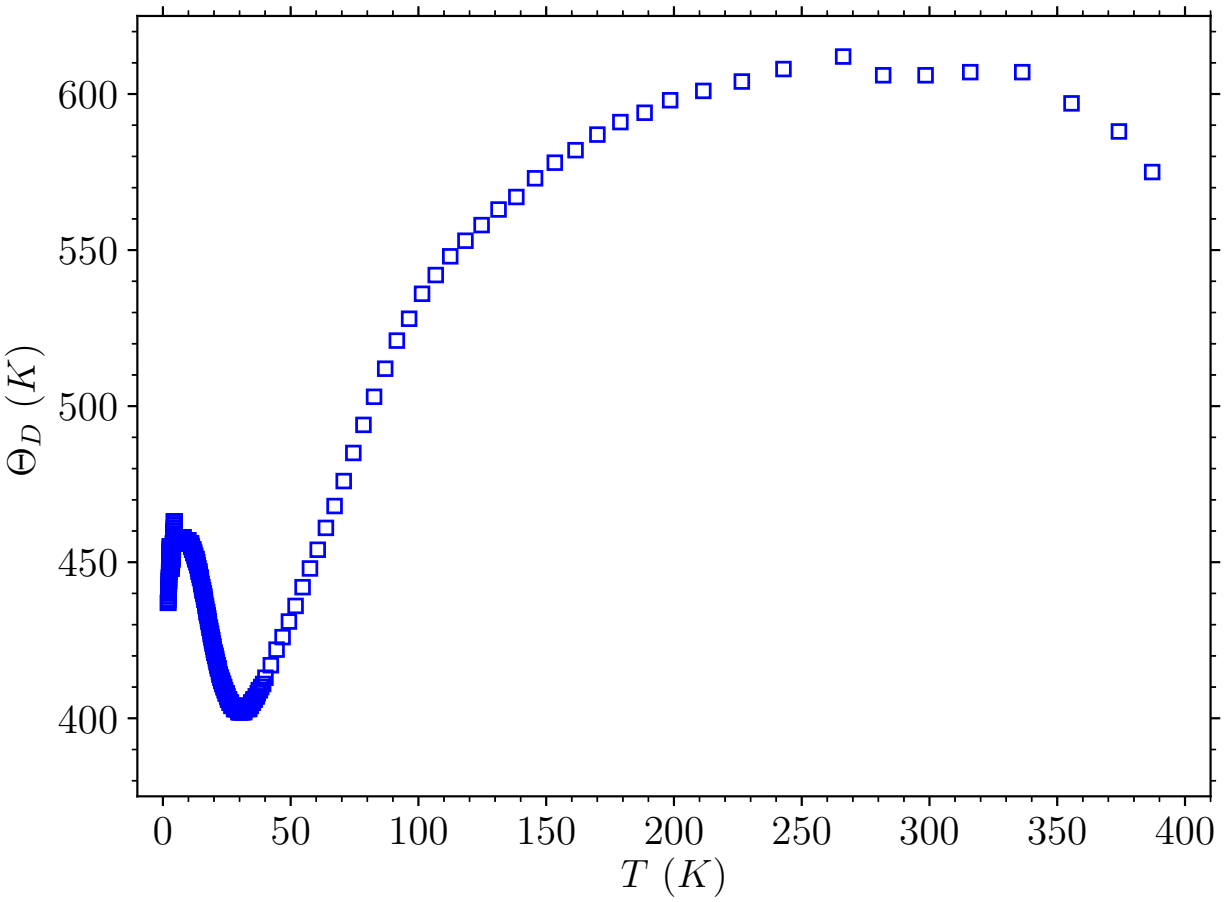

Figure 5.7: Variation of the effective Debye temperature Θ_D with T for stoichiometric CeO_2.

5.4.1 Discussion on Phonon Scattering

The scattering rate $\tau^{-1}(x,T)$ is a combination of the different scattering mechanisms that follow the Matthiessen rule and is given by the following equation:[16]

$$\tau^{-1}(x,T) = v/L + \alpha x^4 T^4 + \beta_U x^2 T^3 e^{-\Theta_D/bT} + \beta_N x^2 T^5. \tag{5.10}$$

Here, included (in order) are the boundary scattering, point defect (Rayleigh) scattering, 3-phonon Umklapp and Normal phonon-phonon interactions through the adjustable parameters L, α, β_U, and β_N respectively. To obtain a best fit to the data, b in the Umklapp expression is left as a further adjustable parameter, though decent fits are obtained by leaving it as a constant, *i.e.* $b = 3$.

For the boundary scattering term the parameter L represents the Casimir length [78], an effective phonon mean free path. For single crystal materials this is given by sample geometry. However, in the context of a polycrystalline aggregate such as this, it can be thought of as the grain size. This analysis gives a best fit when $L = 15.4$ μm which is in general agreement with the measured averaged grain size of 20.5 μm.

Point defect scattering gives a Rayleigh like term of $\omega^4 \propto x^4 T^4$. Klemens [79] then gives the relaxation time in terms of mass defect or isotope scattering. The fitting parameter α is then given by

$$\alpha = \left(\frac{k_B}{\hbar}\right)^4 \frac{V_0}{4\pi v^3}\Gamma \tag{5.11}$$

where Γ is the scattering parameter due to mass fluctuations and is given by $\Gamma = \Sigma_i f_i \left(\frac{\Delta M_i}{M}\right)^2$. Here f_i is the atomic fraction of the ith isotope whose mass is M_i. M is the average atomic mass and $\Delta M_i = |M - M_i|$. This expression must further be modified to include multiple atoms and can also be shown to include effects of strain field scattering [80, 81]. It is difficult to extract physical insights from this term as the matter is further complicated by the easy reduction of CeO_2 into off stoichiometric phases. Also, as discussed below, analysis shows a nearly complete domination of the scattering by 3-phonon Umklapp processes. This analysis gives an $\alpha = 40.6$ s^{-1} K^{-4}. This value is similar to the fitting parameter given by Khafizov [8] as well as parameters used in

analysis of high purity UO_2 and ThO_2 single crystals [82] indicating the samples are of reasonably high quality.

Results indicate that the 3-phonon Umklapp process was the dominating factor with a value of $\beta_U = 7.31 \cdot 10^4$ s^{-1} K^{-3}. In order to obtain the best fit b was allowed to vary with the best fit giving $b = 3.2$. Assuming the relation

$$\beta_U = \left(\frac{k_b}{\hbar}\right)^2 \frac{\hbar\gamma^2}{Mv^2\Theta_D} \tag{5.12}$$

where γ is the Grüneisen parameter and a value of the average atomic mass $M = \rho V_0/N = 9.53 \cdot 10^{-23}$ g. These values suggest a Grüneisen parameter of 4.78 which is well beyond the 2.5 obtained by Khafizov *et al.* and the value of 1.24 for optical phonons. As the system temperature approaches the Debye temperature the Normal process becomes important. In order to bring the fitted function in line with the experimental data, an unphysical value of -0.184 s^{-1} K^{-5} is obtained for β_N. The results for β_U and β_N clearly show the failure of this simple model in explaining the experimental data. Analyses using more complex models, while motivated by this work, are beyond its scope.

6. NONSTOICHIOMETRIC $CEO_{2-\delta}$ RESULTS AND DISCUSSION

As was shown in the previous chapter, stoichiometric CeO_2 behaves in perfect accordance with the theory of heat capacity and thermal conductivity for insulators. However, the high quality data previously obtained by Westrum and Beale [1] showed a distinct additional heat capacity at temperatures $T < 15$ K. I hypothesized that this additional heat capacity was due to impurity of Westrum and Beale's samples based upon the excellent analysis of Gruber *et al.* [69] The additional heat capacity appeared in the form of a Schottky anomaly, which is a result of Zeeman energy level splitting. The most likely impurity of Westrum and Beale's samples was an oxygen deficiency in the lattice. This is due to the ability of CeO_2 to easily give up oxygen in a redox reaction. Although only briefly touched upon in this work, one of the large uses for CeO_2 is as a catalyst in oxidation reactions. Of bigger interest in this study is that this behavior also allows experimentation on a non-radioactive material that can be compared with radioactive $PuO_{2-\delta}$ with the assumption that oxygen vacancies will result in similar behavior in the two materials. In order to definitively and quantitatively study whether oxygen deficiencies were the source of the additional heat capacity, reduced oxide ceria samples were obtained from the Los Alamos group. This chapter will present the experimental data of these nonstoichiometric reduced oxides (of the form $CeO_{2-\delta}$) and briefly touch upon the supporting theory.

6.1 Oxygen Vacancies in Nonstoichiometric $CeO_{2-\delta}$

Pure, stoichiometric ceria is an insulating pale-yellow oxide with the cubic fluorite lattice structure and has a space group of $Fm\bar{3}m$,[12] as seen in Figure 6.1. The lattice parameter is $a_0 = 5.411$ Å. Cerium atoms are located at the corners and face centers of a cube, and Oxygen atoms at the center of tetrahedral Cerium cages. Each Cerium atom is surrounded by eight nearest-neighbor Oxygen atoms. Cerium is stable in both Ce^{3+} and Ce^{4+} oxidation states, leading to stable oxide compounds of Cerium (III) Oxide and Cerium (IV) Oxide, the sesquioxide Ce_2O_3 and dioxide CeO_2 respectively. Further compounds of cerium and oxygen of the fluorite-type lattice such as

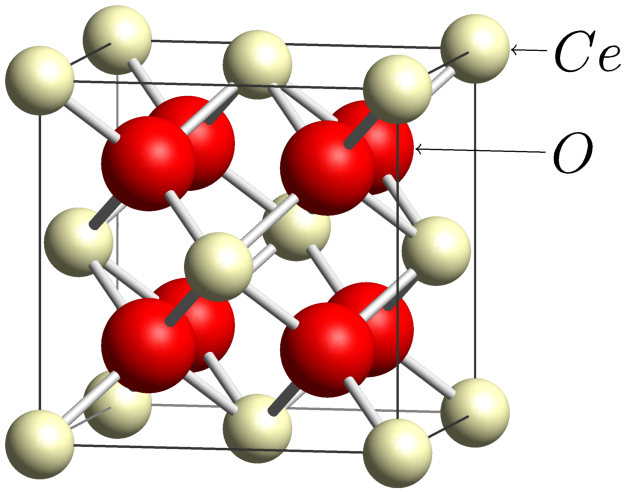

Figure 6.1: Crystal structure of stoichiometric CeO_2. Cerium atoms (yellow) are located at the corners and face centers of a cube, and Oxygen atoms (red) at the center of tetrahedral Cerium cages. Each Cerium atom is surrounded by eight nearest-neighbor Oxygen atoms.

found in CeO_2 and their compositions can be described with the relation Ce_nO_{2n-2m}, where n and m are integers with $(n > m)$.[83] Reduction of Ce(IV) to Ce(III) by oxygen release resulting in oxygen vacancies in the crystal structure allows for formation of nonstiochiometric $CeO_{2-\delta}$.[84] The cubic flourite structure can tolerate a wide range of oxygen deficiency with $0 < \delta < 0.28$. For larger values of δ, a series of ordered oxygen vacancy superstructures is found, ending with Ce_2O_3, equivalent to a value of $\delta = 0.5$, which crystallizes in the related hexagonal bixbyite structure. [85]

For the experimental data presented here we cannot determine the precise location of oxygen vacancies, only note that for every missing Oxygen anion there must exist two Cerium (III) cations

to maintain charge neutrality. Computational studies have shown that it is more energetically favorable for vacancies to form on surface locations and preferentially on certain crystal axis.[86] Since all of the samples studied here are polycrystalline pellets, that implies any oxygen vacancies would preferentially form on grain boundaries of the samples and would result in highly stoichiometric and nonstoichiometric localized regions. The polycrystallinity of the samples therefore result in a highly disordered system, which is difficult to analyze but can provide a rich playground for studying interesting physics.

6.2 Sample Reduction

Sample reductions were carried out by the Los Alamos group in a thermogravimetric analyzer (TGA). Prior to reduction the sintered CeO_2 was weighed on a benchtop balance calibrated to 0.01 mg. The samples were placed on an $Al_2 2O_3$ platform in a commercial simultaneous thermal analyzer (STA 449 F3, Netzsch Instruments, Selb, Germany) to measure the mass loss during both ramp and isothermal reductions. The samples were then reduction heat treated in the TGA. For each sample the final stoichiometry was calculated by accounting for the initial mass of the CeO_2 sample and the mass following reduction as measured on the bench-top balance, which is a common technique used to discern O/M following reduction. [87, 88, 89] The stoichiometries listed here are the expected stoichiometry at time of measurement. $CeO_{2-\delta}$ stoichiometry is not necessarily stable at low temperatures and may have drifted in the time between thermogravimetric analysis and heat capacity measurements.

6.3 Raman Spectroscopy of $CeO_{2-\delta}$

Oxygen vacancies in the $CeO_{2-\delta}$ lattice should theoretically lead to additional Raman peaks in the 600-800 (cm^{-1}) range. According to Weber *et al.* [65], these are due to the longitudinal optical modes. With the lattice strain caused by the vacancies, peak broadening should occur on the main F_{2g} peak, accompanied by a slight leftward shift of the peak position. [65, 90] As mentioned in Chapter 5 Section 5.1 the $CeO_{2-\delta}$ samples were also measured via the same Raman spectroscopy experiment in an effort to verify the oxygen deficiency. As can be seen in Figure 6.2, neither a

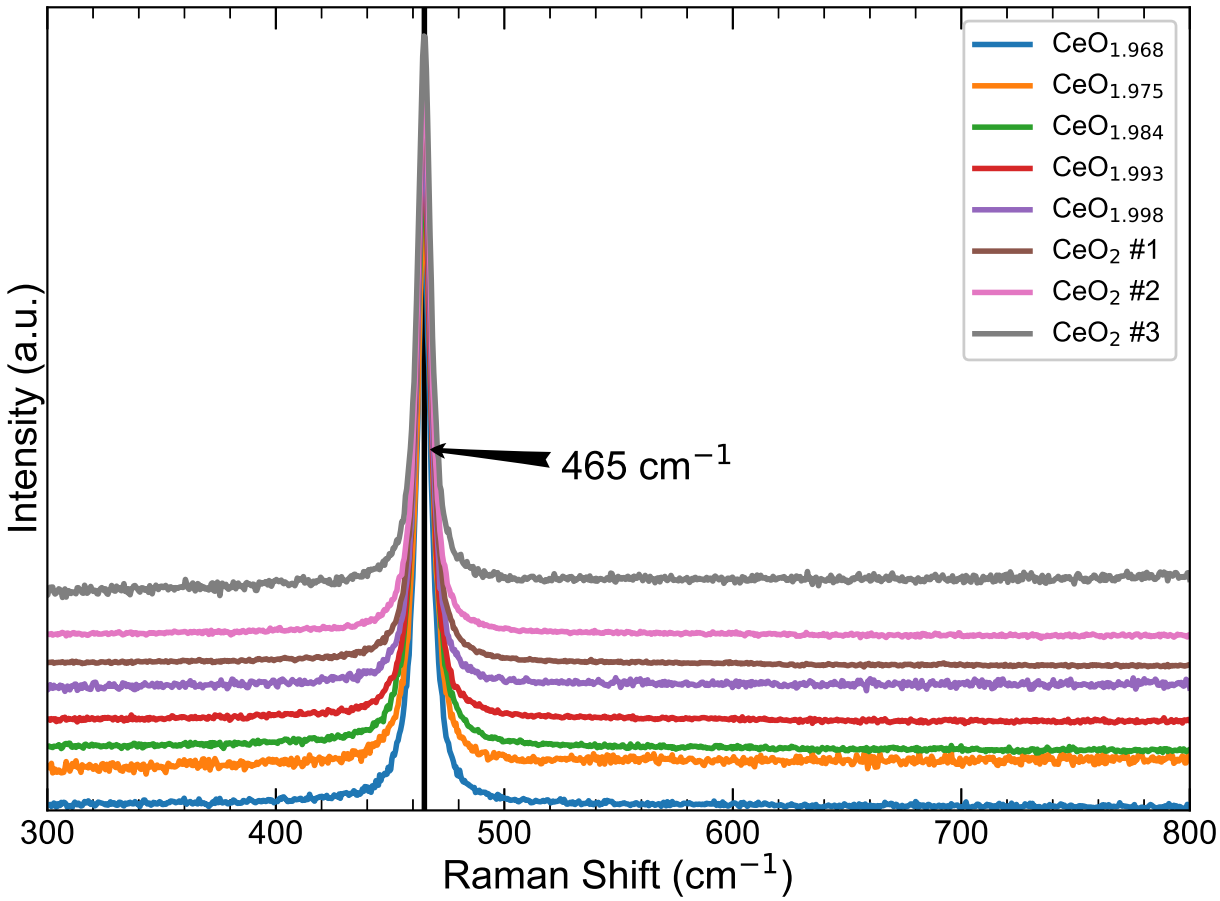

Figure 6.2: Raman Shift of nonstoichiometric $CeO_{2-\delta}$ samples observed in this study compared with stoichiometric CeO_2 samples. Theoretical overtone peaks above the F_{2g} peak in the range 600-800 (cm^{-1}) are not observed for these samples, nor is a broadening of the F_{2g} peak. The Raman spectrums have been shifted vertically for clarity.

broadening of the F_{2g} peak, leftward shift, nor any overtone peaks in the 600-800 (cm^{-1}) range were observed.

These results are not particularly surprising, as the highest amount of Oxygen reduction studied in these samples was $\delta = 0.032$. The overtones should also be more absorbent to UV light wavelengths, meaning the $514.5\,\mathrm{nm}$ Ar-ion excitation laser was not the most suitable choice to bring out the overtone peaks. Unfortunately re-measurement with a UV laser was not possible, nor was confirmation by X-ray Diffraction, Neutron scattering or other techniques. Further Raman effect studies must therefore be relegated to suggested future work. Based upon the Raman results there

was no difference between the reduced samples and stoichiometric CeO_2. It may be said of all the samples that they were of ultra high purity, and as the reader will see below that heat capacity gives a very sensitive probe of the Oxygen vacancies, with the drawback that a low temperature cryostat with high magnetic field is not available in all labs, and a unique contribution by this work.

6.4 Molar Heat Capacity of $CeO_{2-\delta}$

As was demonstrated in Chapter 5, stoichiometric CeO_2 displays textbook theoretical behavior of an insulating solid for all thermodynamic functions. Our measurements set a new standard for low temperature reference data, providing an important correction to T< 15 K measurements originally obtained by Westrum and Beale.[1] Later experiments by Justice and Westrum [91], as well as the analysis by Gruber *et al.* [69] of Ce_2O_3 samples, clearly show a distinct Schottky anomaly in the T< 15 K range. As discussed in Section 6.1 above, as we reduce the stoichiometric CeO_2 by introducing oxygen vacancies in the lattice we will eventually end up with the compound of Ce_2O_3. Therefore it is natural to conclude that the extra heat capacity contribution observed between our CeO_2 data versus Westrum and Beale's is a result of oxygen vacancies and a Schottky contribution. This naturally led to a further line of inquiry: How does the Schottky contribution scale with increasing reduction? In order to answer this question we set out to measure the reduced oxide samples mentioned above.

The LANL group supplied a range of reduced oxide samples for measurement and five different reduction were chosen on the basis that they featured a unique enough δ to show a distinct difference. These were $CeO_{1.968}$, $CeO_{1.975}$, $CeO_{1.984}$, $CeO_{1.993}$, and $CeO_{1.998}$ whose heat capacity is represented in Figures 6.3,6.4,6.5,6.6, and 6.7 respectively. As previously noted, the actual stoichiometry at the time of the heat capacity measurement may have changed from that of the thermogravimetric measurement. All samples were measured in the entire temperature range of 2-400 K at 0 T, and confirmed the presence of an extra heat capacity term, assumed to be a Schottky contribution. In order to further investigate the assumed Schottky contribution, additional measurements were taken from 2-40 K at integer magnetic fields from 0-9 T. The results presented in Figures 6.3-6.7 are all plotted from $0 < T < 15$ K in order to highlight the observed extra contri-

bution to the heat capacity in the low temperature regime. For all the crystals, as the temperature is lowered, the low-temperature anomaly upturn appears to develop starting at approximately 4-5 K when there is 0 T applied field. This effect can most easily be seen in Figure 6.4. With increasing applied field the upturn shifts to higher temperatures and it becomes clear that there is a peak resulting in a downturn of the heat capacity as the temperature is lowered toward 0 K. With zero applied field the peak of the anomaly is below our capability of measurement and should appear near 1 K. To measure the full anomaly the measurement will need to be repeated in a cryostat with a dilution refrigerator.

As an aid to quick comparison, all the figures are presented on the same scale of 0 to $150\,\mathrm{mJ\,mol^{-1}\,K^{-1}}$. Helium liquid shows a heat capacity peak in this temperature regime, so extra caution was taken to measure accurate sample puck heat capacity before measurement. Measurements in this region showed approximately $\pm 8\%$ error or less when comparing multiple runs. This value is slightly worse than the expected measurement error ($< \pm 5\%$) for this temperature region on the PPMS system [39] and we attribute this variation due to absorbed Helium on the sample puck. Final measurements presented here were taken with extra caution to remove any helium in gas in the sample space and are taken as the ideal values.

The stoichiometric data of Chapter 5 is also plotted as a solid line. There can be no electronic contribution to the heat capacity, as even with the creation of lattice vacancies the number of those vacancies and the polycrystalline nature of the samples should not lead to electronic conduction. We must therefore conclude that there is no electronic contribution, only a lattice and an anomalous contribution. While the anomalous contribution is magnetically dependent on the applied field, its magnitude does not show a distinctive sharp peak that would be characteristic of an onset of magnetic ordering, nor would we expect any long range ordering due to the low number of oxygen vacancies. Subsequent investigation was carried out by subtracting off the phonon contribution to the heat capacity $C_{Lattice}$ from the total to view only the anomalous portion. The next section will make it clear that this anomalous heat capacity is indeed a Schottky term and can be fit by assuming a set of split energy levels.

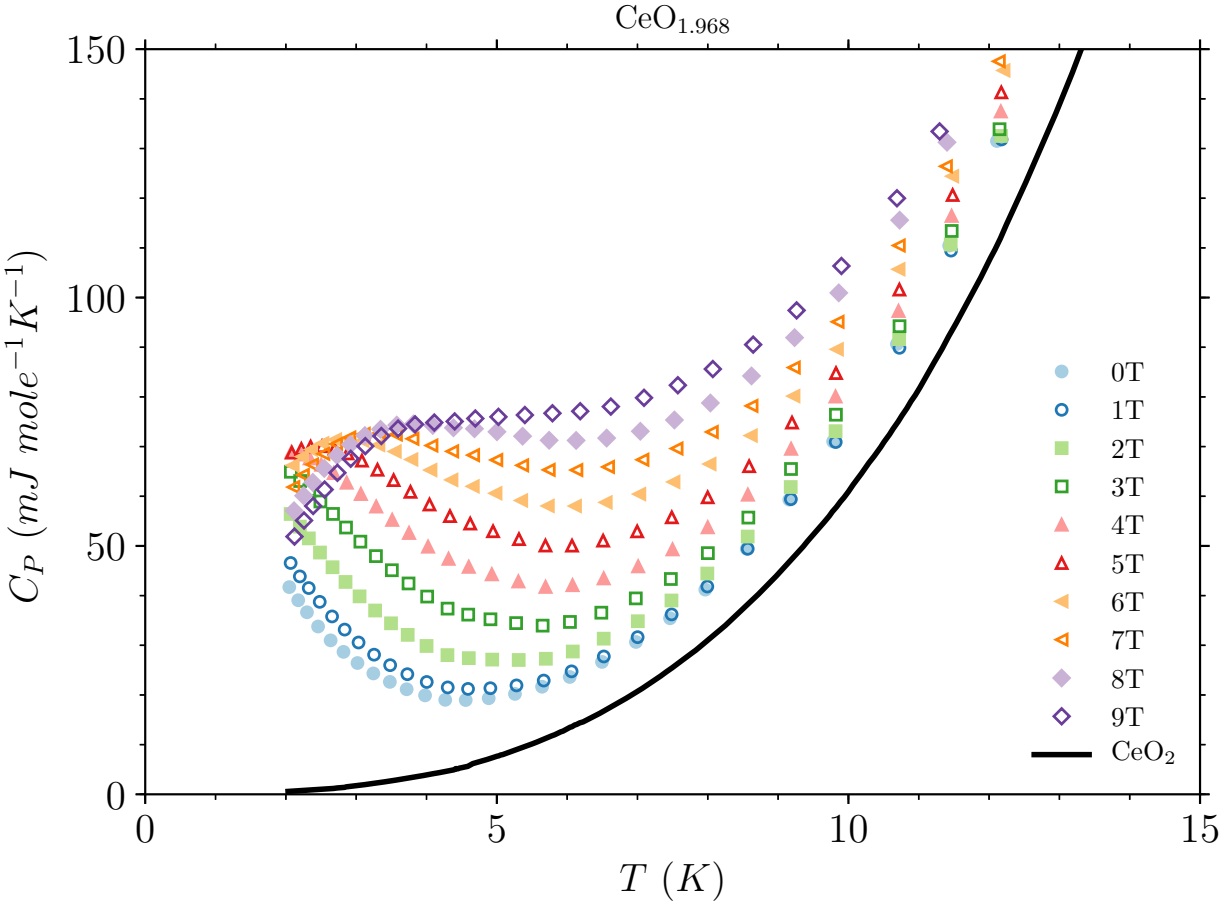

Figure 6.3: Total molar heat capacity of $CeO_{1.968}$ at 0-9 T (symbols). The number of plotted points has been reduced for clarity. The lattice heat capacity of stoichiometric CeO2 is plotted as a solid line.

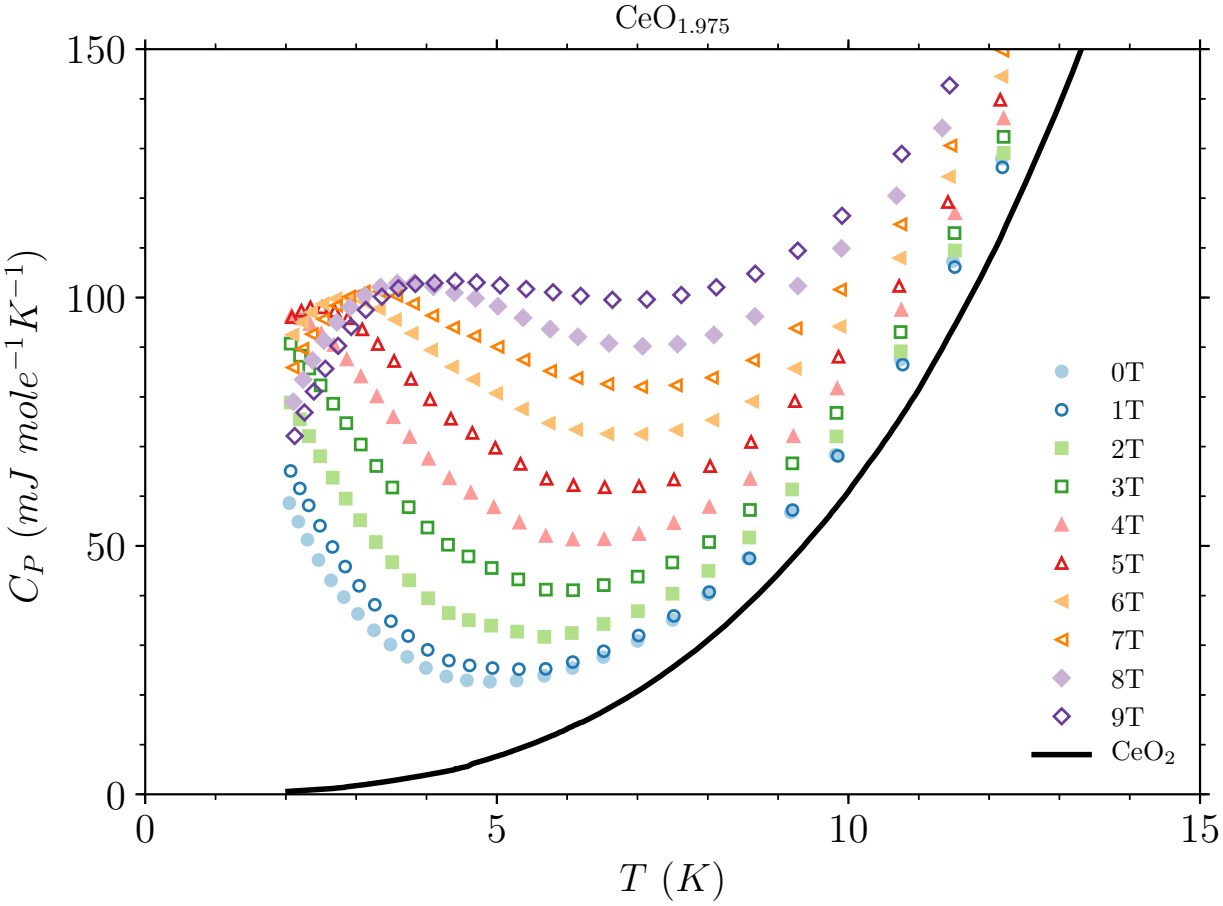

Figure 6.4: Total molar heat capacity of $CeO_{1.975}$ at 0-9 T (symbols). The number of plotted points has been reduced for clarity. The lattice heat capacity of stoichiometric CeO2 is plotted as a solid line.

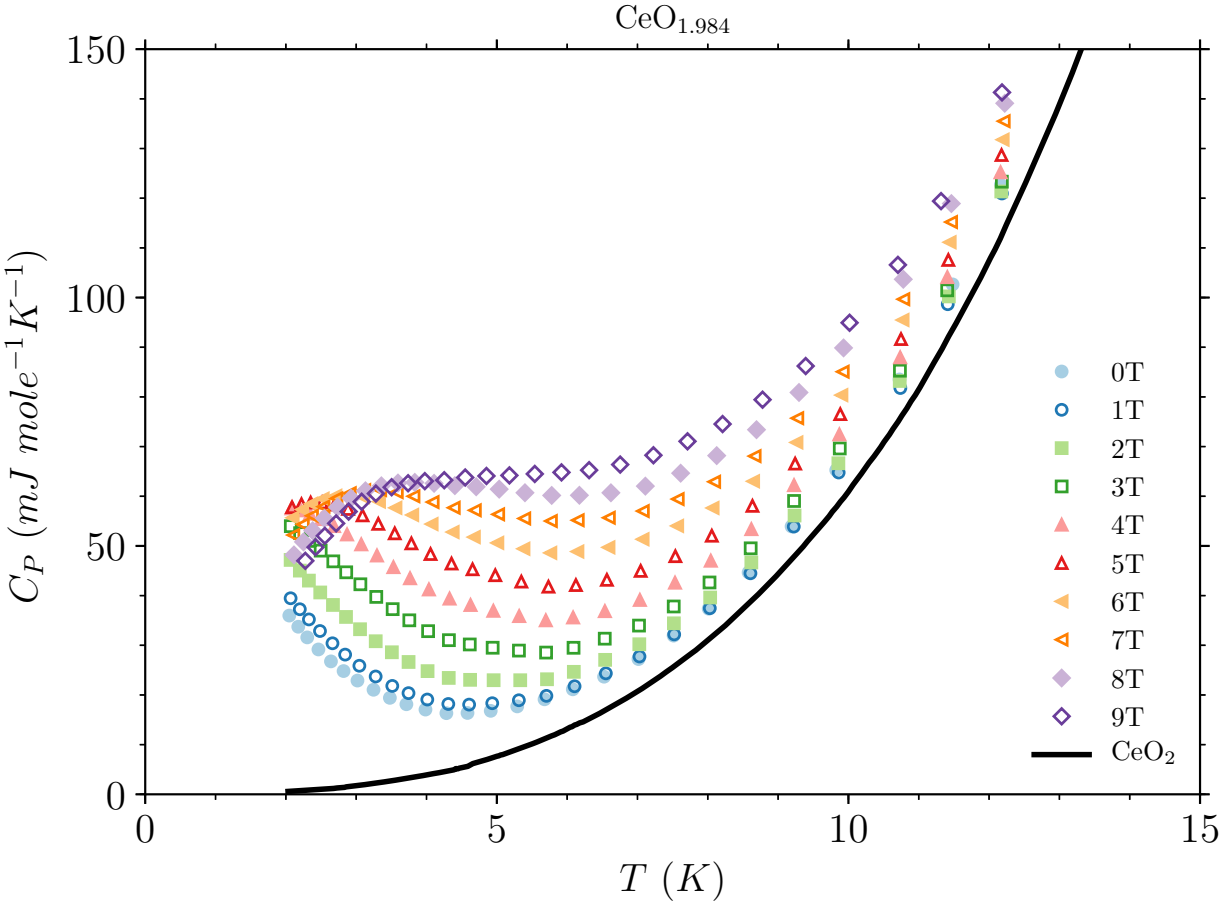

Figure 6.5: Total molar heat capacity of $CeO_{1.984}$ at 0-9 T (symbols). The number of plotted points has been reduced for clarity. The lattice heat capacity of stoichiometric CeO2 is plotted as a solid line.

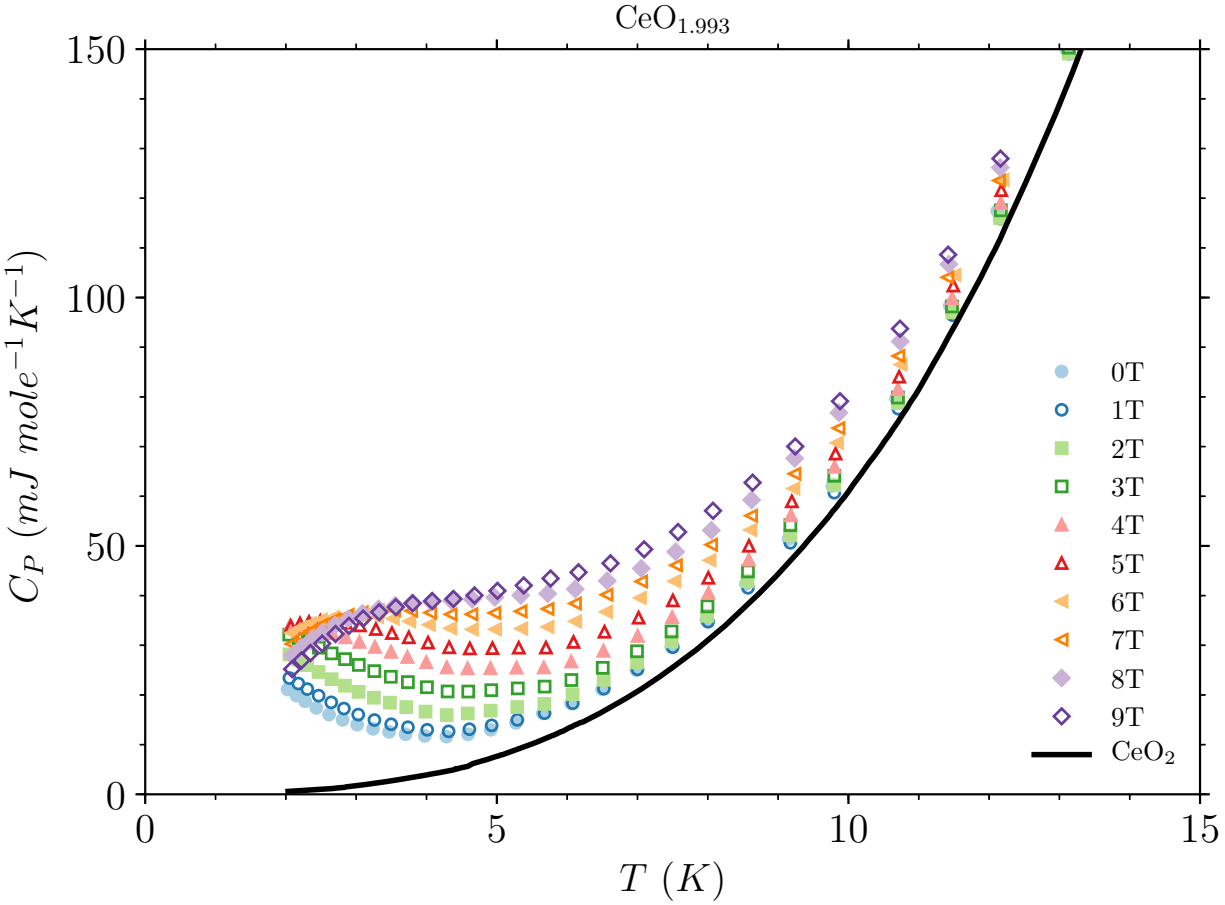

Figure 6.6: Total molar heat capacity of $CeO_{1.993}$ at 0-9 T (symbols). The number of plotted points has been reduced for clarity. The lattice heat capacity of stoichiometric CeO2 is plotted as a solid line.

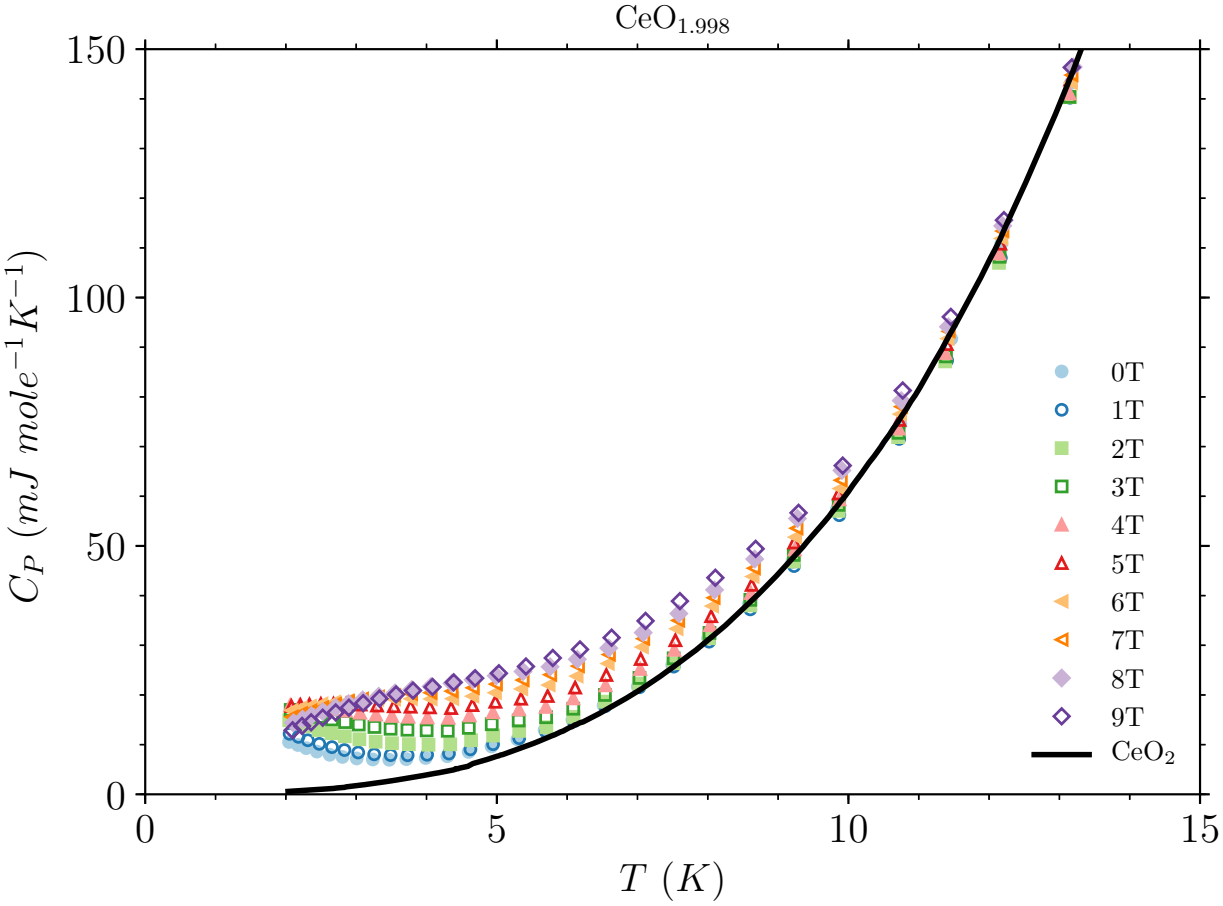

Figure 6.7: Total molar heat capacity of $CeO_{1.998}$ at 0-9 T (symbols). The number of plotted points has been reduced for clarity. The lattice heat capacity of stoichiometric CeO2 is plotted as a solid line.

6.5 Schottky Contribution to the Heat Capacity

As discussed in length above, measurements of stoichiometric CeO_2 clearly showed only a lattice phonon contribution. This is serendipitous for the calculation of the Schottky term, as the lattice value can be directly subtracted from the total heat capacity to obtain the Schottky term. Explicitly this is expressed as

$$C_{Sch}(T, H) = C(T, H) - C_{Lattice} \tag{6.1}$$

where $C_{Sch}(T, H)$ represents the anomalous term, $C(T, H)$ is the total heat capacity, both as a function of temperature T and applied magnetic field H, and $C_{Lattice}$ is the heat capacity of the stoichiometric samples. If the raw experimental data weren't available, $C_{Lattice}$ would need to be calculated from the Einstein or Debye models of the heat capacity. In order to correct for slight temperature differences between runs and to make a perfect subtraction the lattice heat capacity curve and anomalous curves first needed to be interpolated from discrete data into a function. The SciPy interpolation packaged was used for this along with the 1-D interpolation function. Experimental Data was interpolated using the cubic spline option, which will fit a number of low order polynomials to the data instead of a single high order polynomial. The interpolated data could then be directly subtracted. The temperature measurement points of the total heat capacity term were used, while the lattice subtracted term was adjusted to match. For example, if the total heat capacity $C(T, H)$ was measured at $T = 2.15$ K and the $C_{Lattice}$ term was measured at $T = 2.16$ K, then $C_{Lattice}$ interpolated at $T = 2.15$ K and then directly subtracted to yield $C_{Sch}(T, H)$ at $T = 2.15$ K.

Calculating the anomalous term in this manner for all samples, temperatures and applied magnetic fields, it is clear to see that the shape gives that of a Schottky anomaly with the distinct feature that the Schottky term falls off quickly at temperatures below the maximum value and slowly above this value. Figures 6.8-6.12 plot the results of this calculation and demonstrate Schottky anomaly behavior clearly. The number of plotted points has been reduced for clarity, and each plot has a

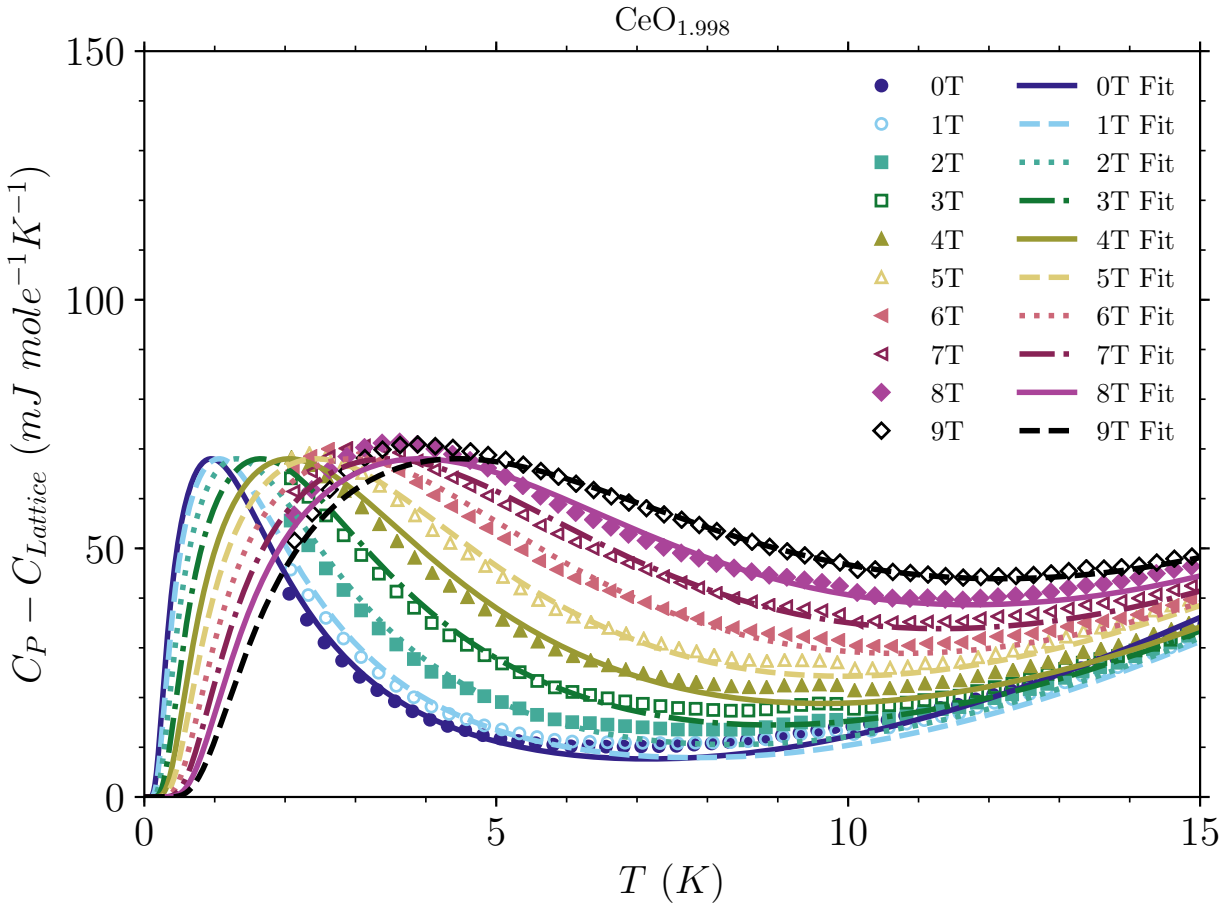

Figure 6.8: Schottky contribution at 0-9 T (symbols) for the $CeO_{1.968}$ sample. The number of plotted points has been reduced for clarity. Also plotted is a multi-level Schottky fitting function that shows excellent agreement with the plotted data.

Schottky fitting function plotted for each applied field. Details of the fitted function will be discussed below. Of particular note is that even with zero applied field, there is a clear Schottky peak. Also observed is a substantial broadening of the peak with higher applied magnetic fields.

The data is obviously of the Schottky form discussed in Chapter 2 Equation 2.37, but the energy between the $^2F_{5/2}$ ground state of any Ce^{3+} free electron and the next $^2F_{7/2}$ excited state is too large at $\approx$ 273 meV[92] to adequately explain the peak. With the peak at zero applied field occurring below 5 K the energy should be approximately the same order of magnitude and would be expected to be $\approx 0.1 - 1.0$ meV. The natural examples of energy gaps at this magnitude are found in paramagnetic salts, which have energy level spacings of approximately 1 to 10 K.

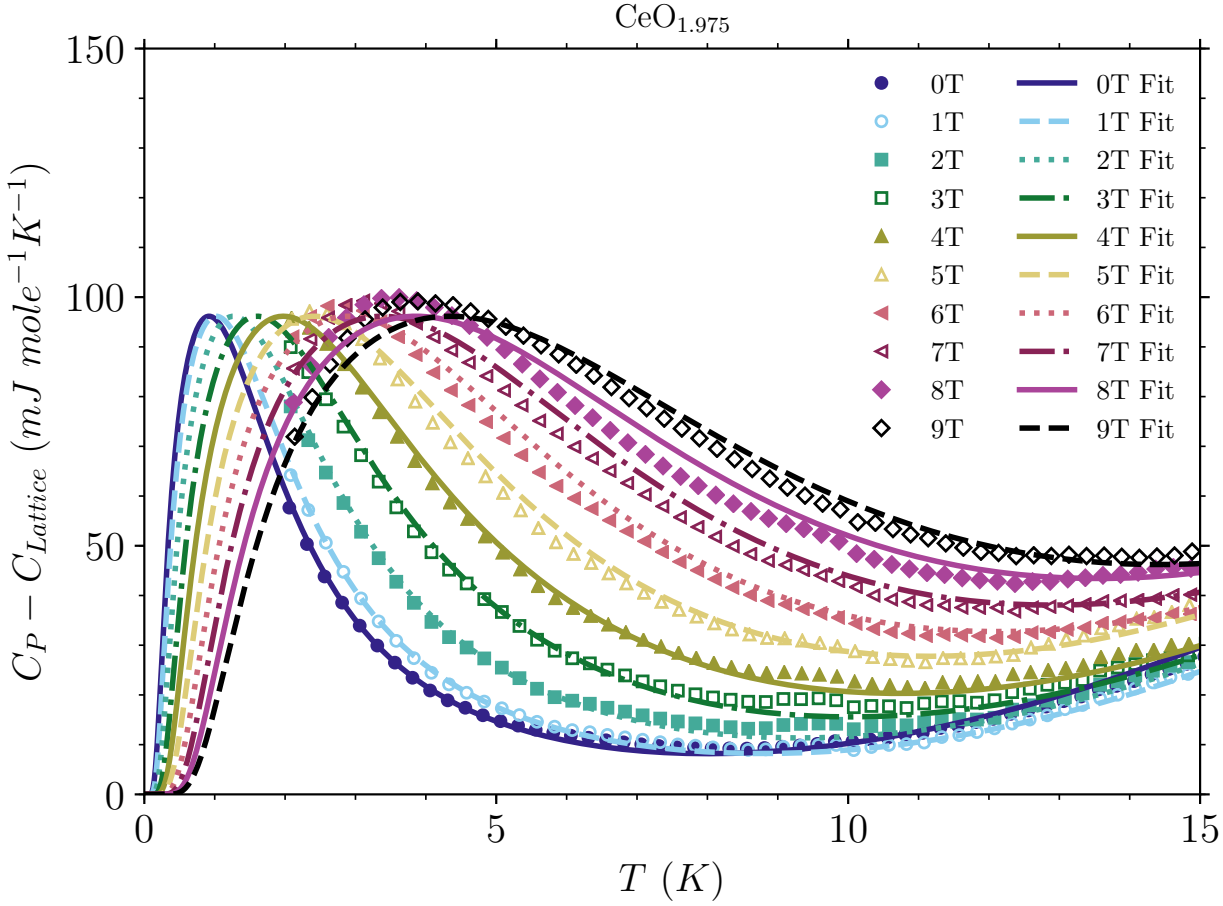

Figure 6.9: Schottky contribution at 0-9 T (symbols) for the $CeO_{1.975}$ sample. The number of plotted points has been reduced for clarity. Also plotted is a multi-level Schottky fitting function that shows excellent agreement with the plotted data.

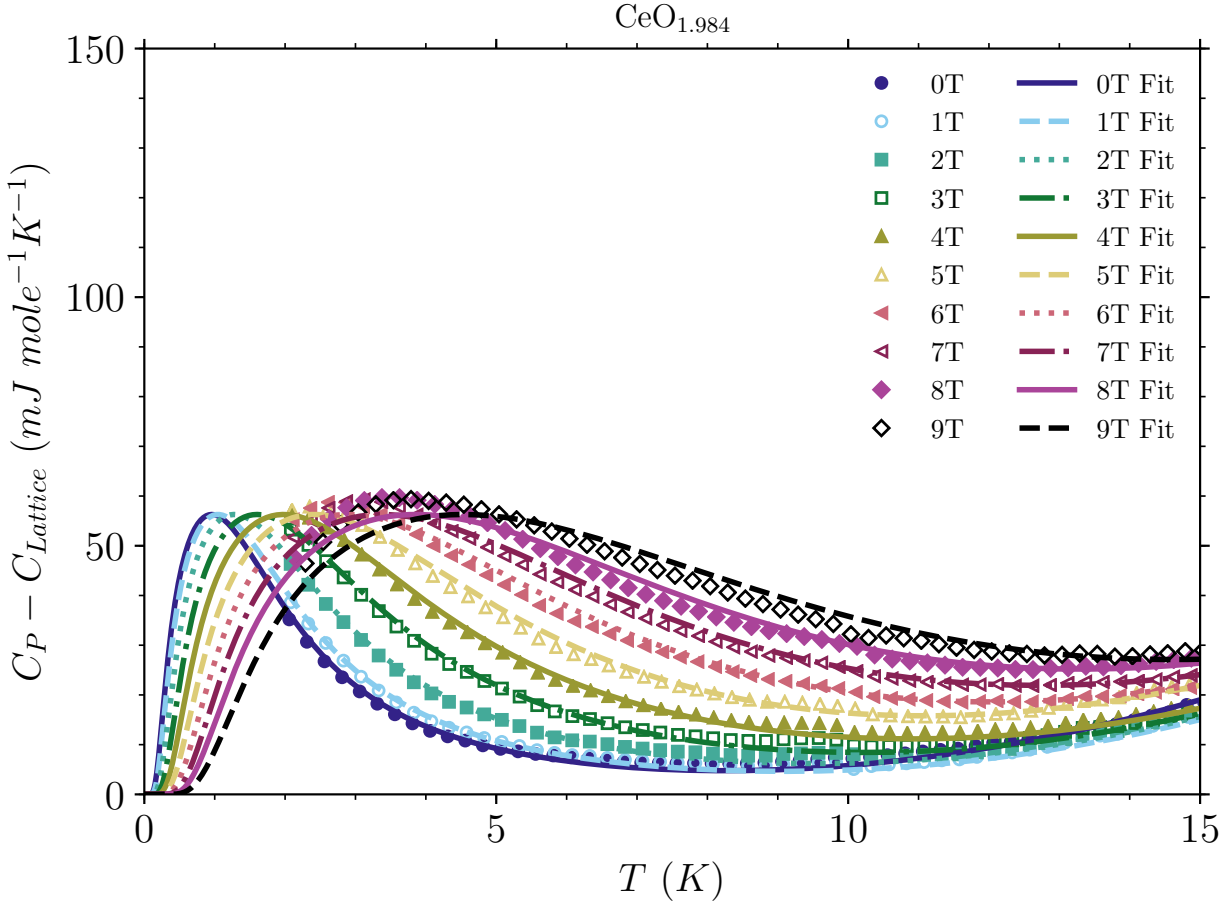

Figure 6.10: Schottky contribution at 0-9 T (symbols) for the $CeO_{1.984}$ sample. The number of plotted points has been reduced for clarity. Also plotted is a multi-level Schottky fitting function that shows excellent agreement with the plotted data.

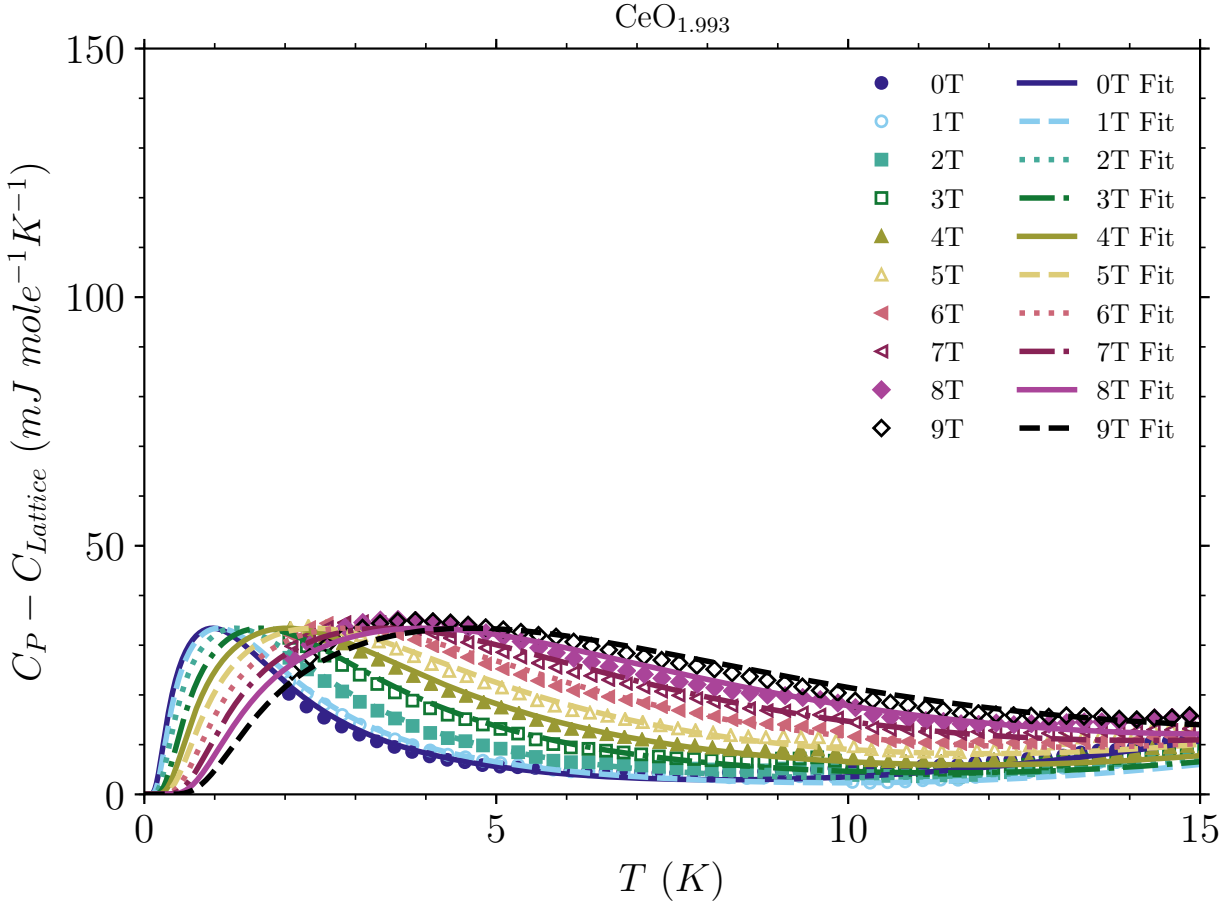

Figure 6.11: Schottky contribution at 0-9 T (symbols) for the $CeO_{1.993}$ sample. The number of plotted points has been reduced for clarity. Also plotted is a multi-level Schottky fitting function that shows excellent agreement with the plotted data.

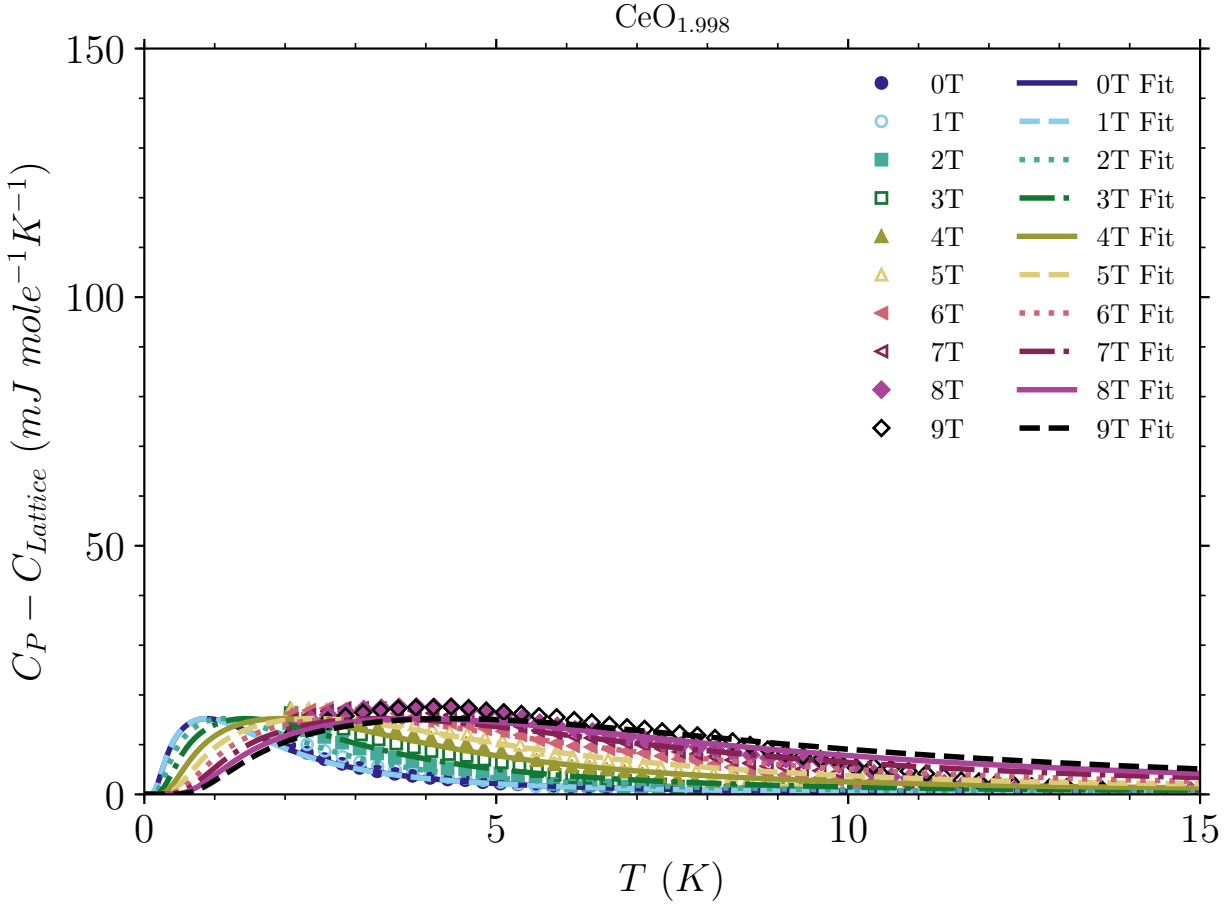

Figure 6.12: Schottky contribution at 0-9 T (symbols) for the $CeO_{1.998}$ sample. The number of plotted points has been reduced for clarity. Also plotted is a multi-level Schottky fitting function that shows excellent agreement with the plotted data.

Thus the Ce^{3+} free electrons must be contributing to the heat capacity in this temperature regime via magnetic interaction. The Schottky upturn is therefore due to magnetic defects in the lattice created when an oxygen vacancy produces two Ce^{3+} free electrons. Each electron has a magnetic dipole moment and the spin quantum number is $s = 1/2$. The Ce^{3+} free electrons do not share an orbit and should therefore exhibit a paramagnetic response to an externally applied field.

For the magnetic moment of a paramagnet, we can use Langevin's theory to describe the states of the system. In this formulation there is no interaction between the magnetic dipoles and are only affected by increases in temperature (thermal agitation) and applied field so we can use a simple term for the energy. Using a Boltzmann distribution to count the probability of being in either the spin up or spin down state, we end up with a magnetization of the form

$$M = N\mu tanh(\mu H/k_B T) \tag{6.2}$$

which when placed in an applied field H, the energy is then MH and the specific heat becomes

$$C_M = (N\mu^2 H^2/k_B T^2) sech^2(\mu H/k_B T). \tag{6.3}$$

This is equivalent to Equation 2.37 but with the energy gap set to $2\mu H$ and $g_0 = g_1$. This is of course just the classic Zeeman effect that splits the ground state in an applied magnetic field. A quick calculation shows that if we set the magnetic dipole moment equal to the Bohr Magneton such that $\mu = \mu_B$ and the applied field to $1 - 10$ T then the energy gap would be $\approx 0.116 - 1.16$ meV, which matches our expected energy gap for a Schottky peak below 5 K as we expected above. Based upon only the relation $2\mu H$ we would expect the energy gap at zero applied field to disappear, but the Schottky anomaly clearly remains even at zero applied field. In 1907 Weiss suggested a mechanism to explain this behavior for ferromagnetic materials.[93] Weiss work showed that due to magnetization of other parts of a solid there is an internal magnetic field acting on the elementary dipoles such that

$$H_{eff} = \sqrt{H_{ext}^2 + H_0^2} \tag{6.4}$$

where H_{ext} is the externally applied field and H_0 is taken as the intrinsic internal field.

For nonstiochiometric $CeO_{2-\delta}$ samples studied here, there aren't enough oxygen vacancies to justify taking an effective internal field across the entire material, yet the magnetic energy gap is still present at zero applied field. The only reasonable explanation is that the magnetic impurities are relatively close to each other forming clusters of magnetic defects that would then act on each other as an internal field. STM measurements [94, 95] of nonstiochiometric $CeO_{2-\delta}$ show that the oxygen vacancies do indeed form clusters, and so the assumption that magnetic impurities in our samples are clustered seems plausible.

6.6 Magnetic Function Fitting

To fit the magnetic contribution with a function, a simple 2-level system could potentially be used, and was attempted. The fit was relatively poor, especially with increasing applied magnetic fields. For independent magnetic clusters Langevin's theory can still be applied, but the total spin for the Ce^{3+} electrons must be taken into account as $J \neq 1/2$ and is instead $J = 5/2$ for the ground state. The corresponding specific heat should be generalized to the multilevel Schottky function[96, 97]:

$$C_m = Nk_B \left[\frac{x^2 e^x}{(e^x - 1)^2} - (2J+1)^2 \frac{x^2 e^{(2J+1)x}}{(e^{(2J+1)x} - 1)^2} \right] \tag{6.5}$$

where $x = g\mu_B H_{eff}/k_B T$, $H_{eff} = \sqrt{H_{ext}^2 + H_0^2}$ as in Equation 6.4, and g is taken as the effective Lande g factor for the cluster.

This multilevel Schottky function shows a peak broadening more consistent with, and fits the data better at temperatures below 10 K, than a simple 2-level Schottky function. In order to simplify the fitting and physical analysis, only N, H_{ext}, and H_0 were varied, while J and g were held constant. For the Ce^{3+} electrons, $J = L - S = 3 - 1/2 = 5/2$ and $g = 6/7$ is calculated by the equation

$$g = 1 + \frac{J(J+1) + S(S+1) - L(L+1)}{2J(J+1)}, \tag{6.6}$$

where J,S,L refer to the total, spin, and orbital angular momentum quantum numbers respectively.

Ideally one could fit all the adjustable parameters, but there is an increased danger of letting one or more parameters become unphysical by over fitting. As the number of parameters increase it is also easy to have an initial fitting guess that won't converge. An example of possible over fitting is given in Figure 6.13. The internal magnetic field H_0 is plotted against the applied field H. Physically the internal magnetic field should only be effective at low applied fields and quickly fall to zero as higher external fields are applied. This is true for the curves of $CeO_{1.998}$, $CeO_{1.984}$, and $CeO_{1.975}$, but breaks down for $CeO_{1.993}$ and $CeO_{1.968}$. There is likely a more complex magnetic interaction happening in all of these samples that cannot be determined by heat capacity measurements alone. It was not possible during the course of this work to complete more magnetic behavior measurements, and leaves opportunity for future work to investigate.

The Schottky term should fall off as T^{-2} as the temperature is increased and eventually trend toward zero. Careful observation of the graphs in Figures 6.8-6.12 show that the multilevel Schottky term is not the only contribution. As the temperature is increased from zero, the Schottky term is prominent below $T < 10$ K, but for $T > 10$ K there is still additional heat capacity above the lattice term that appears to increase as the temperature is increased. This additional heat capacity remains all the way up to the highest temperatures measured. Initially this additional heat capacity was thought to be another Schottky like peak due to an energy gap attributed to spin-orbit coupling or crystal field splitting. Fits using a second Schottky peak in this manner produced poor fitting with high residuals and was abandoned. Further literature review points to an additional contribution by magnon spin waves.[98, 99, 100] Magnons obey Bose-Einstein statistics and have a number of similarities to phonons, including a dispersion relation. The derivation won't be presented here, but follows the same steps covered in Chapter 2. For ferromagnetic materials this results in an addition to the heat capacity of the form $C_m \propto T^{3/2}$ at low temperatures. Interestingly anti-ferromagnetic systems take on a much different form of $C_m \propto T^3$. In general, the

magnetic anisotropy will introduce a finite gap in the magnon dispersion curve, which will scale the above relations as $e^{\frac{-\Delta_{Magnon}}{k_B T}}$. The relation can also be modified by the dimensions involved. We can summarize these results into a simple formula:

$$C_M \propto T^{\frac{d}{m}} e^{\frac{-\Delta_{Magnon}}{k_B T}} \tag{6.7}$$

where d is the dimensionality of magnon excitations and m is defined as the exponent in the dispersion relation $w \propto k^m$. For antiferromagnetic magnons $= 1$ and for ferromagnetic magnons $= 2$. To fit this function both d/m and Δ_{Magnon} were allowed to vary, but d/m was then fixed when an initial best fit obtained.

The Schottky addition to the heat capacity and magnon spin wave addition to the heat capacity were then combined and fitted to the experimental data. The fitting results using this combined function are displayed in Figures 6.8-6.12 along with the experimental data. Agreement with the experimental data is excellent, with only slight variation from the data at the peak and also for high magnetic field curves. Better fits might be obtainable by allowing more parameters to vary, but the analysis becomes much more difficult. For example, the best fits gave a surprising d/m ratio of 0.5, implying that the clusters of magnetic impurities behave as a 1D ferromagnetic spin wave above approximately $10K$. At first glance this appears entirely unphysical, and made analysis extremely difficult. There is some evidence that CeO_2 can exhibit ferromagnetism, even at room temperature.[101] However, without a more thorough study of specifically the magnetism by susceptibility measurements no firm conclusion can be made. This additional heat capacity above 10 K only raises more questions and provides an opportunity for further study. Clearly there is more complex magnetic behavior occurring.

6.7 Spin-Orbit Coupling

As mentioned in the previous section, the choice of fitting using a magnon spin wave appears unphysical due to the localized nature of the Ce^{3+} electrons. The magnon spin wave fitted function showed the best fit to the experimental data, however there is a possible alternate explanation for

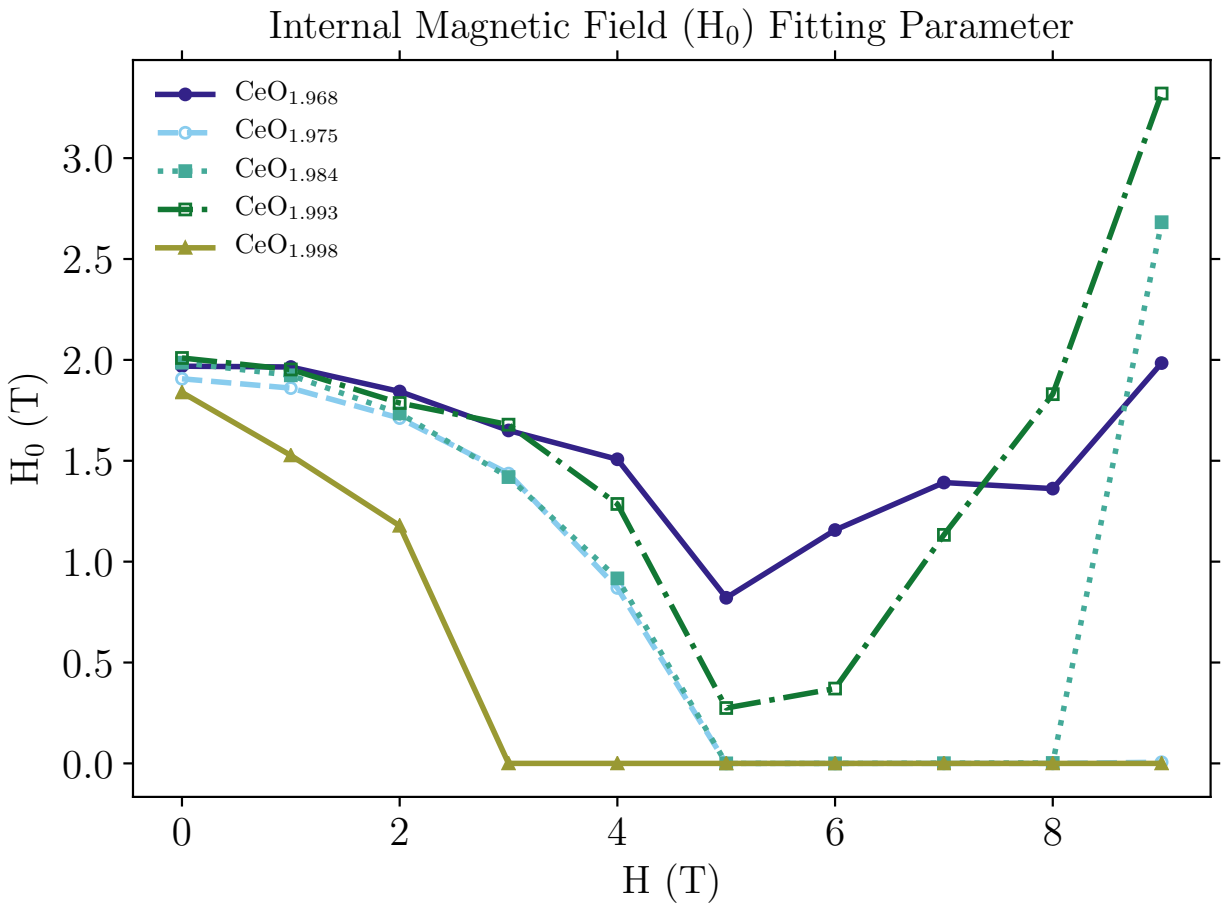

Figure 6.13: Internal magnetic field fitting parameter H_0 vs applied field H.

the additional heat capacity contribution above 10 K. When looking at the T<10 K Schottky peak, the spin-orbit coupling energy gap of the ${}^2F_{5/2}$ ground state of any Ce^{3+} free electron and the next ${}^2F_{7/2}$ excited state was dismissed due to the relatively large energy gap of $\Delta = \approx 300$ meV[92, 102, 103, 104]. While this energy gap is much too large to explain the Schottky peak below 10 K, it is reasonable to assume that it might be producing a broad Schottky peak that extends beyond the measured range and produces a peak at a much higher temperature.

Some of the best evidence that this is the real physical situation are experiments and DFT calculations done for PuO_2. McNeilly's measured band gap of 1.8 eV[105] for the spin-orbit coupling of the J=5/2 ground state and J=7/2 excited state of PuO_2 fits very well with DFT calculations of Nakamura *et al.* [106]. Nakamura *et al.* argue that this is the root cause of the insulating paramagnetic behavior in PuO_2. This result lends strong credence to the idea that a spin-orbit coupling splitting is the root cause of the additional heat capacity above 10 K seen in $CeO_{2-\delta}$. A schematic representation of the energy level splitting for these states due to spin-orbit coupling is given in figure 6.14.

The heat capacity measurements here were only performed up to 40 K with the expectation that the Schottky peak would be completely characterized at this temperature. While this is true for the T<10 K Schottky peak, if we assume that spin-orbit coupling interactions are causing a second Schottky type peak for T>10 K, these measurements are not enough to fully characterize this peak and measurements should be extended to the entire range of 1.8-400 K. A further difficulty with this type of characterization is that at temperatures approaching room temperature and above, the lattice contribution and any anharmonic terms may prove difficult to subtract out without substantial error. Definitive proof of this peak should therefore be left to other measurement methods such as electron paramagnetic resonance (EPR).

6.8 Entropy of $CeO_{2-\delta}$

The heat capacity and the entropy are closely related by the equation:

$$S = \int_0^T \frac{C_p}{T} dT + S_0. \tag{6.8}$$

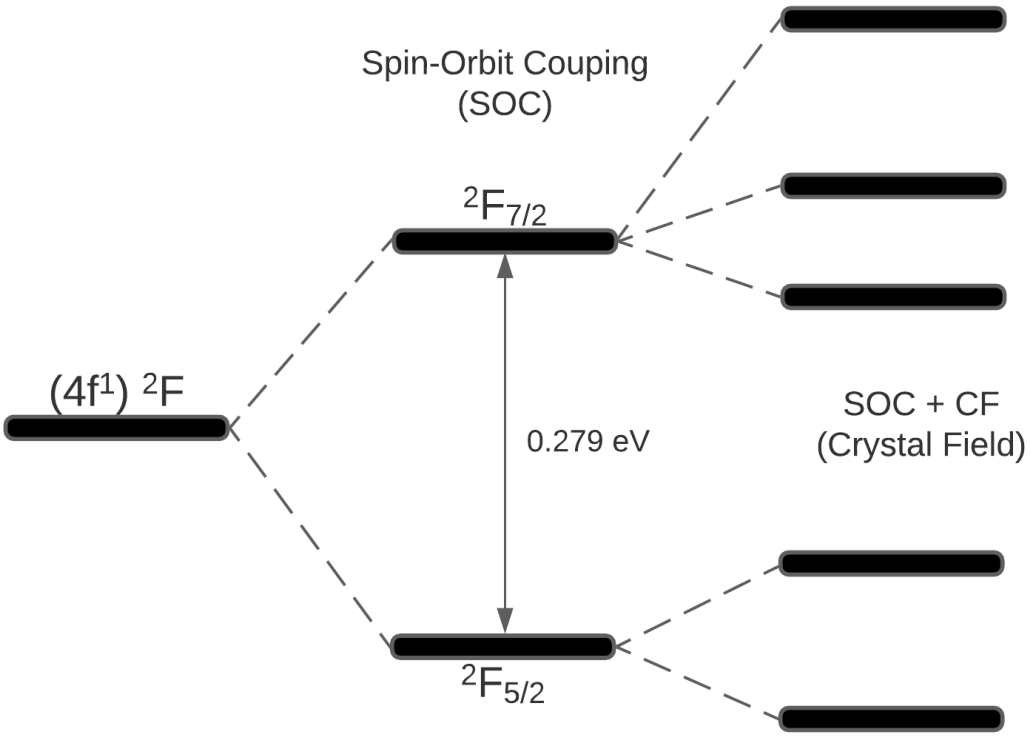

Figure 6.14: Schematic of the 4f electron energy levels, including spin-orbit coupling and crystal field splitting terms. Figure is not to scale.

Since the heat capacity and temperature are both experimentally determined, we can perform a numerical integration to obtain the entropy S. This calculation is more easily performed on the fitted heat capacity function, as it can be calculated for any temperature. It is possible to perform the calculation on the experimental data as well, as was shown in Chapter 5, Figure 5.3 for stoichiometric CeO_2. The entropy calculation for $CeO_{2-\delta}$ is more difficult because the Schottky peak extends below the capability of measurement for our system. Assuming the heat capacity follows the general trend of the Schottky function, it is still possible to perform this calculation, however the true experimental data will deviate from the ideal fitted function.

Calculating the entropy of the magnetic contribution discussed in section 6.5 yields the curves in Figures 6.15-6.19. For clarity, the experimental data has been left off of these plots and only the entropy curves corresponding to the magnetic fitting function are presented. The temperature is also plotted on log scale so that the entire range of $0 - 40$ K can be plotted. It should be noted that the sharp upturn above 10 K is an artifact of the log scale plotting and the actual behavior is a continual slow rise in entropy that corresponds to higher energy states being occupied.

The form of the entropy is that of a classic paramagnetic salt, and therefore it is reasonable to expect a total entropy due to the Schottky portion ($T < 10$ K) to scale as $S = nRln(2)$ where n represents the number of spins either parallel or antiparallel to the field. Since there is also an additional magnetic contribution for temperatures ($T < 10$ K), the entropy continues to rise and does not asymptotically approach $nRln(2)$ as might be expected for only the Schottky portion. Due to the continued rise of the entropy, a suitable choice must be made on where to calculate the maximum entropy due to the Schottky portion. For this work the inflection point where the entropy changes from concave down to concave up was chosen. This value was determined only at an applied field of 0 T for all of the samples and is included in Figures 6.15-6.7. The plateau like behavior in the entropy is a current line of research for frustrated magnetic systems[107], and it appears nonstoichiometric $CeO_{2-\delta}$ may be a candidate for frustrated magnetism. Further study is needed.

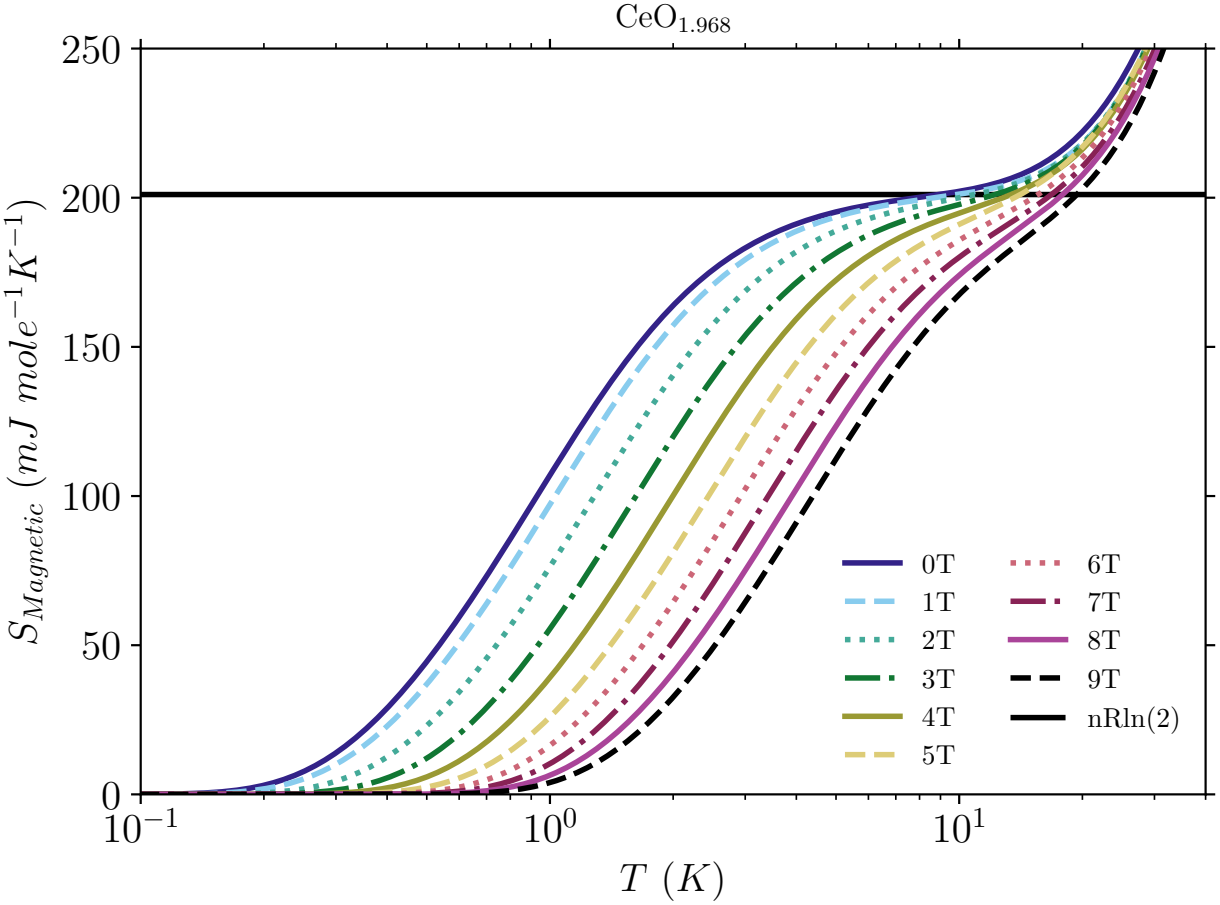

Figure 6.15: Calculated entropy at 0-9 T for the $CeO_{1.968}$ sample. For clarity, experimental data has been left off and the horizontal axis has been plotted on a logarithmic scale. Also plotted is the entropy at the inflection point for the 0T curve.

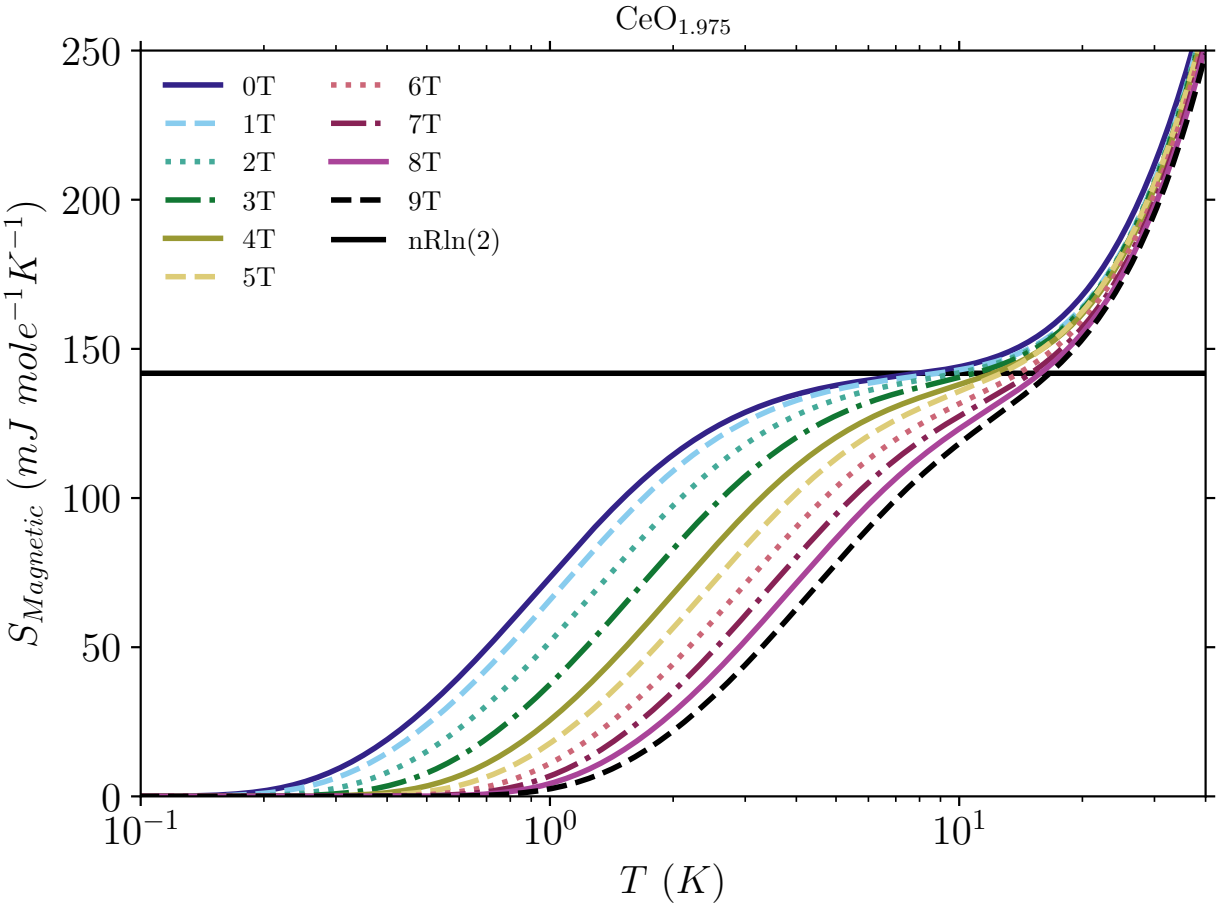

Figure 6.16: Calculated entropy at 0-9 T for the $CeO_{1.975}$ sample. For clarity, experimental data has been left off and the horizontal axis has been plotted on a logarithmic scale. Also plotted is the entropy at the inflection point for the 0T curve.

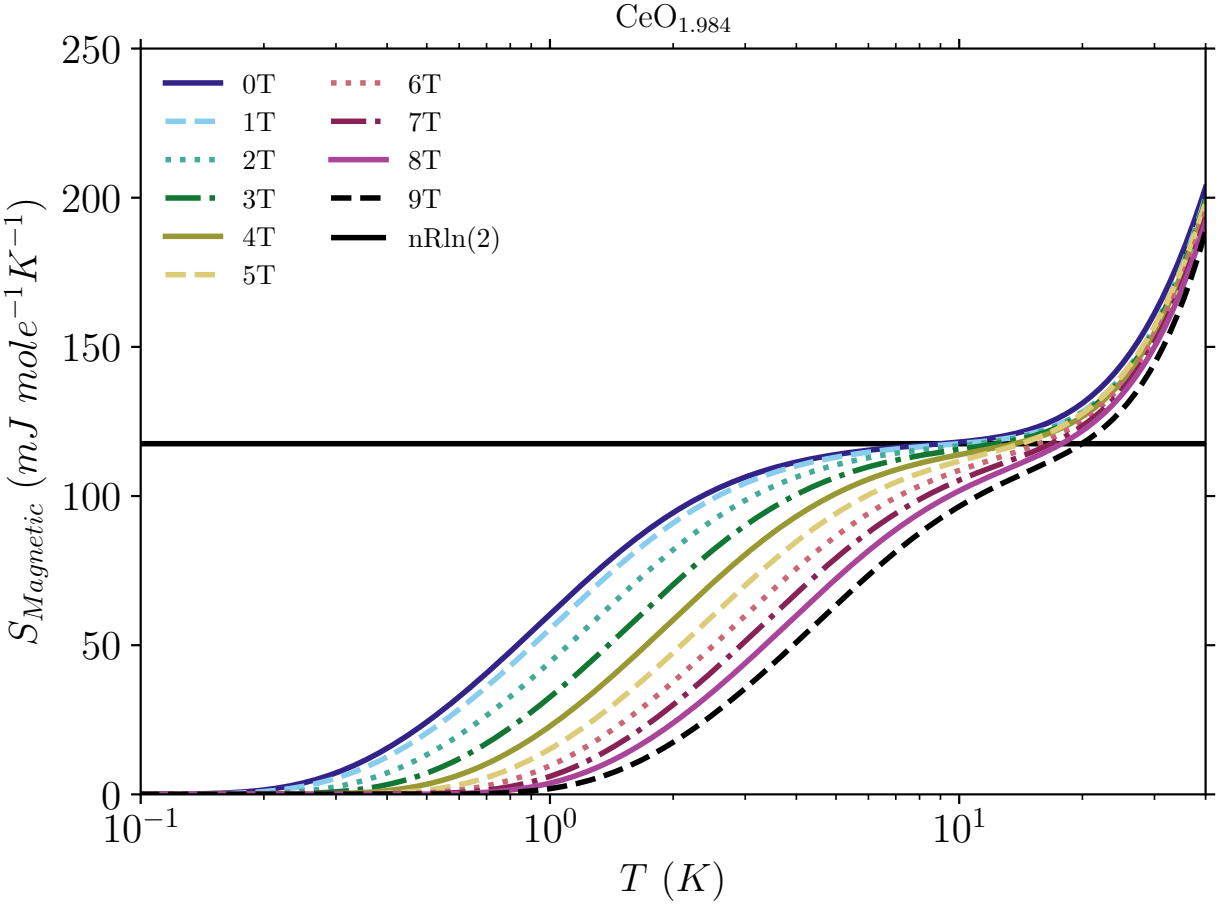

Figure 6.17: Calculated entropy at 0-9 T for the $CeO_{1.984}$ sample. For clarity, experimental data has been left off and the horizontal axis has been plotted on a logarithmic scale. Also plotted is the entropy at the inflection point for the 0T curve.

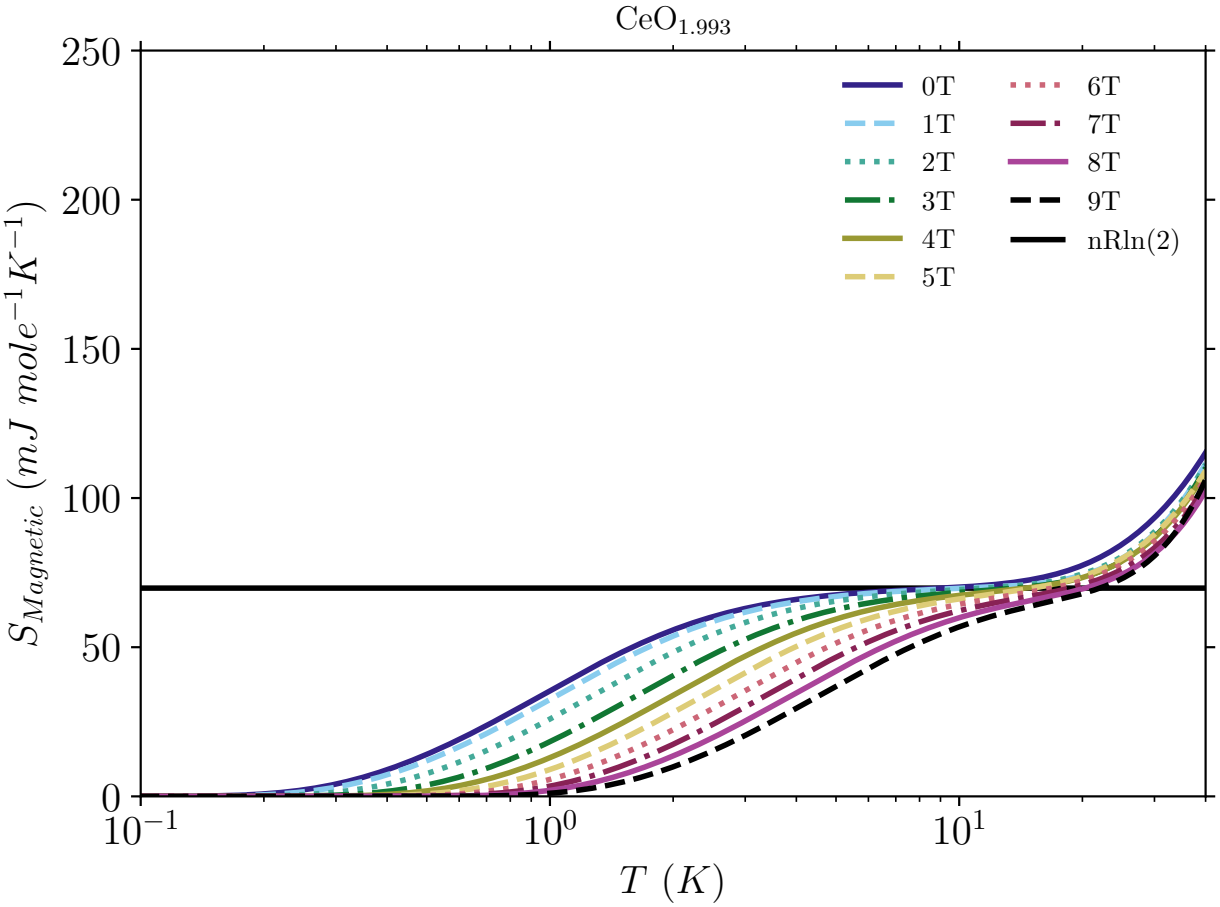

Figure 6.18: Calculated entropy at 0-9 T for the $CeO_{1.993}$ sample. For clarity, experimental data has been left off and the horizontal axis has been plotted on a logarithmic scale. Also plotted is the entropy at the inflection point for the 0T curve.

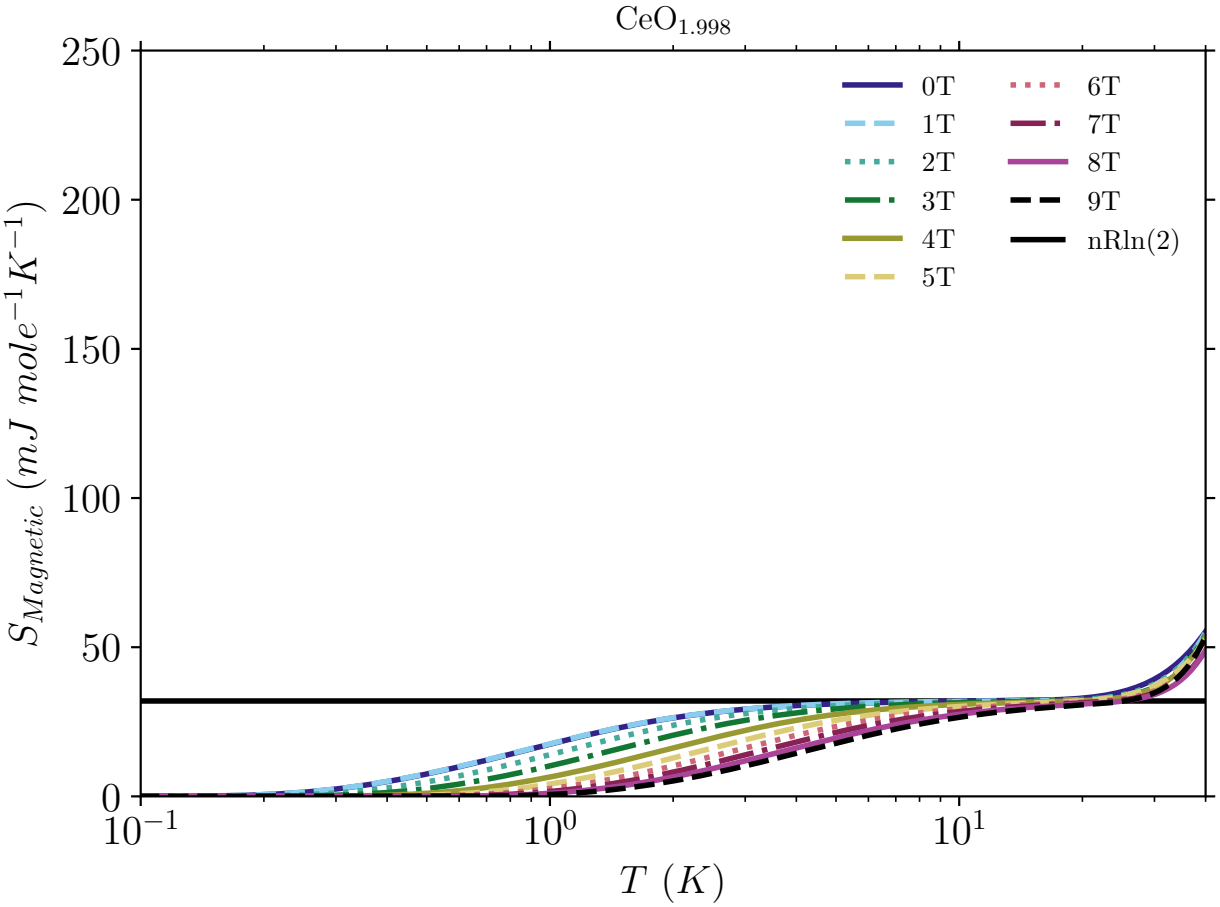

Figure 6.19: Calculated entropy at 0-9 T for the $CeO_{1.998}$ sample. For clarity, experimental data has been left off and the horizontal axis has been plotted on a logarithmic scale. Also plotted is the entropy at the inflection point for the 0T curve.

7. SUMMARY AND CONCLUSIONS

7.1 Conclusions

New experimental measurements of the heat capacity and thermal conductivity below 400 K joined with first principle calculations were performed for stoichiometric CeO_2. Experimentally, raman spectroscopy was performed, the heat capacity was determined by adiabatic calorimetry, while the thermal conductivity was measured with a combination of square wave a.c. drift method (the Maldonado technique), and laser flash analysis. These results were then compared to first principle calculations by density functional perturbation theory. Further thermodynamic properties were calculated and reported using both the experimental data and DFPT results.

Novel heat capacity data was acquired at low-temperature, the new data shows a correction to the existing literature data, and was used to calculate improved thermodynamic functions reported here. The standard values calculated at $T = 298.15$ K for heat capacity and entropy in this study were 63.4 J mol^{-1} K^{-1} and 61.1 J mol^{-1} K^{-1}, respectively. The heat capacity was examined in terms of the simple Debye model, yielding a Debye temperature of 455 K. DFPT results were in good agreement with measured data and previously published literature. The entropy, enthalpy function and Gibbs function were also tabulated from experimental data and theoretical predictions.

The thermal conductivity of stoichiometric CeO_2 was examined using both laser flash analysis and the Maldonado technique. Room temperature values for the thermal conductivity are similar to those of other high quality CeO_2 samples. The thermal conductivity was also analyzed in terms of the Klemens-Callaway model. The mean velocity of sound was determined to be 3610 m/s. At the low temperatures of this study, the thermal conductivity is dominated by 3-phonon Umklaap processes. However, heat conduction of CeO_2 is more complex than simple models can account for and deserves further study in subsequent work.

This study provides a refreshed, accurate, and comprehensive thermodynamic picture of the

bulk properties of CeO_2 in the low-temperature regime. Experimental results show excellent agreement with each other and the DFPT calculations.

The low temperature anomaly of the heat capacity in nonstoichiometric $CeO_{2-\delta}$ samples was investigated in order to examine the deviation of historical CeO_2 data from that presented here. This anomalous heat capacity was shown to have a Schottky term that is attributed to Zeeman splitting of Ce^{3+} cations as well as an additional magnon like term. The low temperature magnetic behavior of $CeO_{2-\delta}$ appears to be a novel measurement and should aid in future studies of rare earth oxide materials.

7.2 Further Study

During the course of this work the thermal conductivity of the $CeO_{2-\delta}$ samples was not able to be completed. A natural extension of this work would be to measure the thermal conductivity of these reduced oxides. The complex magnetic behavior observed in the heat capacity measurements of the $CeO_{2-\delta}$ samples could benefit from a more thorough theoretical analysis as well as additional measurements. The magnetic susceptibility should be measured and if possible electron paramagnetic resonance should also be performed.

REFERENCES

[1] E. F. Westrum and A. F. Beale, "HEAT CAPACITIES AND CHEMICAL THERMODYNAMICS OF CERIUM(III) FLUORIDE AND OF CERIUM(IV) OXIDE FROM 5 TO 300 k," *J. Phys. Chem.*, vol. 65, pp. 353–355, Feb. 1961.

[2] F. A. Kuznetsov, T. N. Rezukhina, and A. N. Golubenko, "Heat capacity of cerium dioxide at high temperature," *Zhur. Fiz. Khim. (Letter)*, vol. 34, p. 2129, 1960.

[3] R. Krishnan and K. Nagarajan, "Heat capacity measurements on uranium-cerium mixed oxides by differential scanning calorimetry," *Thermochimica Acta*, vol. 440, no. 2, pp. 141–145, 2006.

[4] S. Gallagher and W. Dworzak, "Thermodynamic properties of cerium oxalate and cerium oxide," *J. Am. Ceram. Soc.*, vol. 68, no. 8, pp. C206–C207, 1985.

[5] I. Riess, M. Recken, and J. Nolting, "On the specific-heat of nonstoichiometric ceria," *J. Sol. State Chem.*, vol. 57, no. 3, pp. 314–322, 1985.

[6] E. G. King and A. U. Christensen, *High-Temperature Heat Contents and Entropies of Ceriun Dioxide and Columbium Dioxide*. U.S. Department of the Interior, Bureau of Mines, Report 5789, July 1961.

[7] T. S. Yashvili, D. S. Tsagareishvili, and G. G. Gvelesiani, "Enthalpy and heat capacity of the yttrium sesquioxide and cerium dioxide at high temperatures.," *Soobshch. Akad. Nauk Gruz. SSR*, vol. 46, p. 409, 1967.

[8] M. Khafizov, I.-W. Park, A. Chernatynskiy, L. He, J. Lin, J. J. Moore, D. Swank, T. Lillo, S. R. Phillpot, A. El-Azab, D. H. Hurley, and D. Clarke, "Thermal conductivity in nanocrystalline ceria thin films," *J. Am. Ceram. Soc.*, vol. 97, pp. 562–569, dec 2013.

[9] T. D. Morrison, E. S. Wood, P. F. Weck, E. Kim, S. O. Woo, A. T. Nelson, and D. G. Naugle, "A comprehensive assessment of the low-temperature thermal properties and ther-

modynamic functions of CeO2," *The Journal of Chemical Physics*, vol. 151, p. 044202, jul 2019.

[10] C. Walkey, S. Das, S. Seal, J. Erlichman, K. Heckman, L. Ghibelli, E. Traversa, J. F. McGinnis, and W. T. Self, "Catalytic properties and biomedical applications of cerium oxide nanoparticles," *Environ. Sci. Nano*, vol. 2, no. 1, pp. 33–53, 2015.

[11] S. Song, X. Wang, and H. Zhang, "Ceo_2-encapsulated noble metal nanocatalysts: enhanced activity and stability for catalytic application," *NPG Asia Mater.*, vol. 7, pp. e179–e179, May 2015.

[12] S. Logothetidis, P. Patsalas, E. Evangelou, N. Konofaos, I. Tsiaoussis, and N. Frangis, "Dielectric properties and electronic transitions of porous and nanostructured cerium oxide films," *Mater. Sci. Eng. B*, vol. 109, pp. 69–73, June 2004.

[13] J. A. Rodriguez, S. Ma, P. Liu, J. Hrbek, J. Evans, and M. Perez, "Activity of ceox and tiox nanoparticles grown on au(111) in the water-gas shift reaction," *Science*, vol. 318, pp. 1757–1760, Dec. 2007.

[14] Q. Fu, H. Saltsburg, and M. Flytzani-Stephanopoulos, "Active nonmetallic Au and Pt species on ceria-based water-gas shift catalysts," *Science*, vol. 301, pp. 935–938, Aug. 2003.

[15] H.-J. Beie and A. Gnörich, "Oxygen gas sensors based on CeO_2 thick and thin films," *Sens. Actuators B*, vol. 4, pp. 393–399, June 1991.

[16] A. Goyal, M. P. Paranthaman, and U. Schoop, "The rabits approach: Using rolling-assisted biaxially textured substrates for high-performance YBCO superconductors," *MRS Bull.*, vol. 29, pp. 552–561, Aug. 2004.

[17] M. S. Dresselhaus and I. L. Thomas, "Alternative energy technologies," *Nature*, vol. 414, pp. 332–337, Nov. 2001.

[18] G. A. Deluga, "Renewable hydrogen from ethanol by autothermal reforming," *Science*, vol. 303, pp. 993–997, Feb. 2004.

[19] S. Park, J. M. Vohs, and R. J. Gorte, "Direct oxidation of hydrocarbons in a solid-oxide fuel cell," *Nature*, vol. 404, pp. 265–267, Mar. 2000.

[20] S. Mochizuki and F. Fujishiro, "The photoluminescence properties and reversible photoinduced spectral change of CeO_2 bulk, film and nanocrystals," *Phys. Stat. Sol. (B)*, vol. 246, no. 10, pp. 2320–2328, 2009.

[21] A. T. Nelson, D. R. Rittman, J. T. White, J. T. Dunwoody, M. Kato, and K. J. McClellan, "An Evaluation of the Thermophysical Properties of Stoichiometric CeO_2 in Comparison to UO_2 and PuO_2," *Journal of the American Ceramic Society*, vol. 97, pp. 3652–3659, Nov. 2014.

[22] H. S. Kim, C. Y. Joung, B. H. Lee, J. Y. Oh, Y. H. Koo, and P. Heimgartner, "Applicability of CeO_2 as a surrogate for Pu_2 in a MOX fuel development," *J. Nucl. Mater.*, vol. 378, pp. 98–104, Aug. 2008.

[23] R. J. M. Konings, O. Benes, A. Kovacs, D. Manara, D. Sedmidubsky, L. Gorokhov, V. S. Iorish, V. Yungman, E. Shenyavskaya, and E. Osina, "The Thermodynamic Properties of the f- Elements and their Compounds. Part 2. The Lanthanide and Actinide Oxides," *J. Phys. Chem. Ref. Data*, vol. 43, MAR 2014.

[24] C. B. Gopal and A. van de Walle, "Ab initio thermodynamics of intrinsic oxygen vacancies in ceria," *Phys. Rev. B*, vol. 86, p. 134117, Oct 2012.

[25] Z.-W. Niu, Y. Cheng, H.-Y. Zhang, and G.-F. Ji, "First-principles investigations on structural, phonon, and thermodynamic properties of cubic CeO_2," *International Journal of Thermophysics*, vol. 35, pp. 1601–1612, Aug 2014.

[26] Z.-W. Niu, Z.-Y. Zeng, C.-E. Hu, L.-C. Cai, and X.-R. Chen, "Study of the thermodynamic properties of CeO_2 from ab initio calculations: The effect of phonon-phonon interaction," *J. Chem. Phys.*, vol. 142, JAN 7 2015.

[27] J. P. Perdew, K. Burke, and M. Ernzerhof, "Generalized gradient approximation made simple," *Phys. Rev. Lett.*, vol. 77, pp. 3865–3868, 1996.

[28] P. F. Weck and E. Kim, "Assessing hubbard-corrected AM05+U and PBEsol+U density functionals for strongly correlated oxides CeO_2 and Ce_2O_3," *Phys. Chem. Chem. Phys.*, vol. 18, no. 38, pp. 26816–26826, 2016.

[29] J. P. Perdew, A. Ruzsinszky, G. I. Csonka, O. A. Vydrov, G. E. Scuseria, L. A. Constantin, X. Zhou, and K. Burke, "Restoring the density-gradient expansion for exchange in solids and surfaces," *Phys. Rev. Lett.*, vol. 100, p. 136406, Apr. 2008.

[30] H. Preston-Thomas, "The international temperature scale of 1990 (ITS-90)," *Metrologia*, vol. 27, pp. 3–10, Jan. 1990.

[31] R. Clausius, *The Mechanical Theory of Heat: With Its Applications to the Steam-engine and to the Physical Properties of Bodies*. J. Van Voorst, 1867.

[32] P. L. Dulong and A.-T. Petit, "Recherches sur quelques points importans de la theorie de la chaleur," *Annales de Chimie et de Physique*, 1819.

[33] A. Einstein, "Die plancksche theorie der strahlung und die theorie der spezifischen wärme," *Annalen der Physik*, vol. 327, no. 1, pp. 180–190, 1907.

[34] P. Debye, "Zur theorie der spezifischen wärmen," *Annalen der Physik*, vol. 344, no. 14, pp. 789–839, 1912.

[35] M. Born and T. von Kármán, "Über schwingungen in raumgittern," *Physikalishe Zeitschrift*, vol. 13, pp. 297–309, 1912.

[36] M. Blackman, "On the relation of debye theory and the lattice theory of specific heats," *Proceedings of the Royal Society A: Mathematical, Physical and Engineering Sciences*, vol. 181, pp. 58–67, Sept. 1942.

[37] W. Schottky, "Über die drehung der atomachsen in festen körpen," *Physikalsiche Zeitschrift*, vol. 23, pp. 448–455, 1922.

[38] J. Callaway, "Model for lattice thermal conductivity at low temperatures," *Phys. Rev.*, vol. 113, pp. 1046–1051, feb 1959.

[39] J. Lashley, M. Hundley, A. Migliori, J. Sarrao, P. Pagliuso, T. Darling, M. Jaime, J. Cooley, W. Hults, L. Morales, D. Thoma, J. Smith, J. Boerio-Goates, B. Woodfield, G. Stewart, R. Fisher, and N. Phillips, "Critical examination of heat capacity measurements made on a Quantum Design physical property measurement system," *Cryogenics*, vol. 43, pp. 369–378, jun 2003.

[40] P. Robinson, J. Watt, J. Black, and D. McKie, *Partners in Science: Letters of James Watt and Joseph Black*. Harvard University Press, 1969.

[41] A. Lavoisier and P. Laplace, *Memoir on heat. read to the Royal Academy of Sciences, 28 June 1783, by Messrs. Lavoisier and De La Place ; translated with an introduction and notes by Henry Guerlac.* N. Watson Academic Publications, 1982.

[42] A. Eucken, "Über die bestimmung spezifischer wärmen bei tiefen temperaturen," *Physikalische Zeitschrift*, vol. 10, pp. 586–589, 1909.

[43] W. Nernst, "Research on specific heat at low temperatures," *Sitzb. Kgl. Preuss. Akad. Wiss*, vol. 12, p. 261, 1910.

[44] R. Bachmann, F. J. DiSalvo, T. H. Geballe, R. L. Greene, R. E. Howard, C. N. King, H. C. Kirsch, K. N. Lee, R. E. Schwall, H. Thomas, and R. B. Zubeck, "Heat Capacity Measurements on Small Samples at Low Temperatures," *Review of Scientific Instruments*, vol. 43, pp. 205–214, feb 1972.

[45] R. E. Schwall, R. E. Howard, and G. R. Stewart, "Automated small sample calorimeter," *Review of Scientific Instruments*, vol. 46, pp. 1054–1059, aug 1975.

[46] G. R. Stewart, B. Cort, and G. W. Webb, "Specific heat of A15 Nb_3Sn in fields to 18 tesla," *Physical Review B*, vol. 24, pp. 3841–3846, oct 1981.

[47] G. R. Stewart, "Measurement of lowtemperature specific heat," *Review of Scientific Instruments*, vol. 54, pp. 1–11, jan 1983.

[48] S. G. Doettinger-Zech, M. Uhl, D. L. Sisson, and A. Kapitulnik, "Simple microcalorimeter for measuring microgram samples at low temperatures," *Review of Scientific Instruments*, vol. 72, pp. 2398–2406, may 2001.

[49] B. L. Zink, B. Revaz, R. Sappey, and F. Hellman, "Thin film microcalorimeter for heat capacity measurements in high magnetic fields," *Review of Scientific Instruments*, vol. 73, pp. 1841–1844, apr 2002.

[50] J. P. Shepherd, "Analysis of the lumped τ_2 effect in relaxation calorimetry," *Review of Scientific Instruments*, vol. 56, pp. 273–277, feb 1985.

[51] J. S. Hwang, K. J. Lin, and C. Tien, "Measurement of heat capacity by fitting the whole temperature response of a heat-pulse calorimeter," *Review of Scientific Instruments*, vol. 68, pp. 94–101, jan 1997.

[52] S. Riegel and G. Weber, "A dual-slope method for specific heat measurements," *Journal of Physics E: Scientific Instruments*, vol. 19, pp. 790–791, oct 1986.

[53] A. C. Burr, "Notes on the history of the concept of thermal conductivity," *Isis*, vol. 20, no. 1, pp. 246–259, 1933.

[54] T. N. Narasimhan, "Fourier's heat conduction equation: History, influence, and connections," *Reviews of Geophysics*, vol. 37, no. 1, pp. 151–172, 1999.

[55] T. N. Narasimhan, "Thermal conductivity through the 19th century," *Physics Today*, vol. 63, no. 8, pp. 36–41, 2010.

[56] O. Maldonado, "Pulse method for simultaneous measurement of electric thermopower and heat conductivity at low temperatures," *Cryogenics*, vol. 32, no. 10, pp. 908 – 912, 1992.

[57] Q. Design, *Physical Properties Measurement System: AC Transport Option User's Manual*, 2009.

[58] Q. Design, *Physical Properties Measurement System: Hardware Manual*, 2009.

[59] Q. Design, *Physical Properties Measurement System: Thermal Transport Option User's Manual*, 2009.

[60] Q. Design, *Physical Properties Measurement System: Heat Capacity Option User's Manual*, 2009.

[61] W. J. Parker, R. J. Jenkins, C. P. Butler, and G. L. Abbott, "Flash method of determining thermal diffusivity, heat capacity, and thermal conductivity," *Journal of Applied Physics*, vol. 32, no. 9, pp. 1679–1684, 1961.

[62] M. WoŁcyrz and L. Kepinski, "Rietveld refinement of the structure of CeOCI formed in Pd/CeO_2 catalyst: Notes on the existence of a stabilized tetragonal phase of La_2O_3 in LaPdO system," *J. Solid State Chem.*, vol. 99, pp. 409–413, Aug. 1992.

[63] S. S. Courts, "A standardized cernox™ cryogenic temperature sensor for aerospace applications," *Cryogenics*, vol. 64, pp. 248–254, nov 2014.

[64] G. A. Kourouklis, A. Jayaraman, and G. P. Espinosa, "High-pressure Raman study of CeO_2 to 35 GPa and pressure-induced phase transformation from the fluorite structure," *Phys. Rev. B*, vol. 37, pp. 4250–4253, Mar. 1988.

[65] W. H. Weber, K. C. Hass, and J. R. McBride, "Raman study of CeO_2: Second-order scattering, lattice dynamics, and particle-size effects," *Phys. Rev. B*, vol. 48, no. 1, pp. 178–185, 1993.

[66] A. Nakajima, A. Yoshihara, and M. Ishigame, "Defect-induced Raman spectra in doped CeO_2," *Phys. Rev. B*, vol. 50, pp. 13297–13307, Nov. 1994.

[67] A. Filtschew, K. Hofmann, and C. Hess, "Ceria and its defect structure: New insights from a combined spectroscopic approach," *J. Phys. Chem. C*, vol. 120, pp. 6694–6703, mar 2016.

[68] C. Schilling, A. Hofmann, C. Hess, and M. V. Ganduglia-Pirovano, "Raman spectra of polycrystalline ceo2: A density functional theory study," *J. Phys. Chem. C*, vol. 121, pp. 20834–20849, sep 2017.

[69] J. B. Gruber, B. H. Justice, J. Edgar F. Westrum, and B. Zandi, "Revisiting the thermophysical properties of the a-type hexagonal lanthanide sesquioxides between temperatures of 5 k and 1000 k," *J. Chem. Thermodyn.*, vol. 34, pp. 457–473, apr 2002.

[70] T. Hisashige, Y. Yamamura, and T. Tsuji, "Thermal expansion and debye temperature of rare earth-doped ceria," *J. Alloys Compd.*, vol. 408-412, pp. 1153–1156, Feb. 2006.

[71] G. Kresse and J. Hafner, "Ab initio molecular dynamics for liquid metals," *Phys. Rev. B*, vol. 47, pp. 558–561, Jan. 1993.

[72] G. Kresse and J. Furthmüller, "Efficient iterative schemes for ab initio total-energy calculations using a plane-wave basis set," *Phys. Rev. B*, vol. 54, pp. 11169–11186, Oct. 1996.

[73] J. Buckeridge, D. O. Scanlon, A. Walsh, C. R. A. Catlow, and A. A. Sokol, "Dynamical response and instability in ceria under lattice expansion," *Phys. Rev. B*, vol. 87, p. 214304, June 2013.

[74] J. L. Haas and J. R. Fisher, "Simultaneous evaluation and correlation of thermodynamic data," *American Journal of Science*, vol. 276, pp. 525–545, apr 1976.

[75] K. Suzuki, M. Kato, T. Sunaoshi, H. Uno, U. Carvajal-Nunez, A. Nelson, and K. McClellan, "Thermal and mechanical properties of CeO_2," *Journal of the American Ceramic Society.*, vol. 102, pp. 1994–2008, 2018.

[76] T. Barron, W. Berg, and J. Morrison, "The thermal properties of alkali halide crystals ii. analysis of experimental results," *Proceedings of the Royal Society of London, A*, vol. 242, pp. 478–492, 1957.

[77] M. Blackman, "On the relation of debye theory and the lattice theory of specific heats," *Proceedings of the Royal Society of London A*, vol. 181, pp. 58–67, 1941.

[78] H. Casimir, "Note on the conduction of heat in crystals," *Physica*, vol. 5, pp. 495–500, jun 1938.

[79] P. G. Klemens, "The thermal conductivity of dielectric solids at low temperatures (theoretical)," *Proc. R. Soc. Lond. A*, vol. 208, pp. 108–133, aug 1951.

[80] B. Abeles, "Lattice thermal conductivity of disordered semiconductor alloys at high temperatures," *Phys. Rev.*, vol. 131, pp. 1906–1911, sep 1963.

[81] G. S. Nolas, J. L. Cohn, and G. A. Slack, "Effect of partial void filling on the lattice thermal conductivity of skutterudites," *Phys. Rev. B*, vol. 58, pp. 164–170, jul 1998.

[82] K. Gofryk, S. Du, C. R. Stanek, J. C. Lashley, X. Y. Liu, R. K. Schulze, J. L. Smith, D. J. Safarik, D. D. Byler, K. J. McClellan, B. P. Uberuaga, B. L. Scott, and D. A. Andersson, "Anisotropic thermal conductivity in uranium dioxide," *Nat. Commun.*, vol. 5, aug 2014.

[83] M. ZINKEVICH, D. DJUROVIC, and F. ALDINGER, "Thermodynamic modelling of the cerium–oxygen system," *Solid State Ionics*, vol. 177, pp. 989–1001, apr 2006.

[84] T. Montini, M. Melchionna, M. Monai, and P. Fornasiero, "Fundamentals and catalytic applications of CeO_2-based materials," *Chemical Reviews*, vol. 116, pp. 5987–6041, apr 2016.

[85] S. Gangopadhyay, D. D. Frolov, A. E. Masunov, and S. Seal, "Structure and properties of cerium oxides in bulk and nanoparticulate forms," *Journal of Alloys and Compounds*, vol. 584, pp. 199–208, jan 2014.

[86] J. Conesa, "Computer modeling of surfaces and defects on cerium dioxide," *Surface Science*, vol. 339, pp. 337–352, oct 1995.

[87] S. Ackermann, J. R. Scheffe, and A. Steinfeld, "Diffusion of Oxygen in Ceria at Elevated Temperatures and Its Application to H_2O/CO_2 Splitting Thermochemical Redox Cycles," *The Journal of Physical Chemistry C*, vol. 118, pp. 5216–5225, feb 2014.

[88] N. Knoblauch, L. Dörrer, P. Fielitz, M. Schmücker, and G. Borchardt, "Surface controlled reduction kinetics of nominally undoped polycrystalline CeO_2," *Physical Chemistry Chemical Physics*, vol. 17, no. 8, pp. 5849–5860, 2015.

[89] Y. Hao, C.-K. Yang, and S. M. Haile, "Ceria-zirconia solid solutions ($Ce_{1-x}Zr_xO_{2-\delta}$, x $\leq$ 0.2) for solar thermochemical water splitting: A thermodynamic study," *Chemistry of Materials*, vol. 26, pp. 6073–6082, oct 2014.

[90] Z. Popović, Z. Dohčević-Mitrović, M. Šćepanović, M. Grujić-Brojčin, and S. Aškrabić, "Raman scattering on nanomaterials and nanostructures," *Annalen der Physik*, vol. 523, pp. 62–74, oct 2010.

[91] B. H. Justice and E. F. Westrum, "Thermophysical properties of the lanthanide oxides. v. heat capacity, thermodynamic properties, and energy levels of cerium(III) oxide," *The Journal of Physical Chemistry*, vol. 73, pp. 1959–1962, jun 1969.

[92] U. Valiev, *Magnetooptical spectroscopy of the rare-earth compounds : development and application*. Irvine, Calif: Scientific Reserch Publishing, Inc, 2012.

[93] P. Weiss, "L'hypothèse du champ moléculaire et la propriété ferromagnétique," *Journal de Physique Théorique et Appliquée*, vol. 6, no. 1, pp. 661–690, 1907.

[94] H. Nörenberg and G. A. D. Briggs, "Defect structure of Nonstoichiometric-CeO2(111)surfaces studied by scanning tunneling microscopy," *Physical Review Letters*, vol. 79, pp. 4222–4225, nov 1997.

[95] F. Esch, "Electron localization determines defect formation on ceria substrates," *Science*, vol. 309, pp. 752–755, jul 2005.

[96] R. L. Falge and N. M. Wolcott, "Cluster specific heats in copper-rich Cu-Ni alloys: The effect of iron," *Journal of Low Temperature Physics*, vol. 5, pp. 617–650, dec 1971.

[97] C. S. Lue, J. H. Ross, C. F. Chang, and H. D. Yang, "Field-dependent specific heat in Fe_2VAl and the question of possible 3d heavy fermion behavior," *Physical Review B*, vol. 60, pp. R13941–R13945, nov 1999.

[98] K. Charles Kittel, *Quantum Theory of Solids*. John Wiley & Sons, 1987.

[99] L. J. Sundström, "Chapter 5 low temperature heat capacity of the rare earth metals," in *Metals*, pp. 379–410, Elsevier, 1978.

[100] R. D. Batist, R. Gevers, and M. Verschueren, "Magnon Contribution to the Low-Temperature Specific Heat of UO_2," *Physica Status Solidi (b)*, vol. 19, no. 1, pp. 77–88, 1967.

[101] K. Ackland and J. Coey, "Room temperature magnetism in CeO_2—A review," *Physics Reports*, vol. 746, pp. 1–39, jul 2018.

[102] S. S. Naghavi, A. A. Emery, H. A. Hansen, F. Zhou, V. Ozolins, and C. Wolverton, "Giant onsite electronic entropy enhances the performance of ceria for water splitting," *Nature Communications*, vol. 8, aug 2017.

[103] W. M. Yen, "General factors governing the efficiency of luminescent devices," *Physics of the Solid State*, vol. 47, no. 8, p. 1393, 2005.

[104] A. Kramida and Y. Ralchenko, "NIST Atomic Spectra Database, NIST Standard Reference Database 78," 1999.

[105] C. McNeilly, "The electrical properties of plutonium oxides," *Journal of Nuclear Materials*, vol. 11, pp. 53–58, jan 1964.

[106] H. Nakamura, M. Machida, and M. Kato, "Effects of spin-orbit coupling and strong correlation on the paramagnetic insulating state in plutonium dioxides," *Physical Review B*, vol. 82, Oct. 2010.

[107] O. Bradley, C. Feng, R. T. Scalettar, and R. R. P. Singh, "Robustness of entropy plateaus: A case study of triangular ising antiferromagnets," *Physical Review B*, vol. 100, aug 2019.